Dipartimento di Fisica

CORSO DI LAUREA MAGISTRALE
INTERATENEO IN FISICA

Curriculum Fisica Nucleare e Subnucleare

TESI DI LAUREA MAGISTRALE

Study of the reconstruction efficiency of π^0 mesons from decays of the τ lepton at the Belle II experiment

Laureando:
Ermes Aviano

Relatore:
Dott. Diego Tonelli

Correlatori:
Dott. Benigno Gobbo
Dott. Sebastiano Raiz

ANNO ACCADEMICO 2023-2024

Abstract

This experimental particle-physics thesis explores a novel approach to the determination of the π^0 meson reconstruction efficiency, whose uncertainty is a significant limitation in measurements sensitive to beyond Standard Model physics.

I aim to determine the π^0 reconstruction efficiency by comparing the rates of $\tau^- \rightarrow \pi^- \pi^0 \nu_\tau$ with $\tau^- \rightarrow \pi^- \nu_\tau$ decays recorded with the Belle II detector in SuperKEKB electron-positron collisions. Since these decays have large branching fractions known with high precision, have little background, and cover a wide range in π^0 momentum, this approach would enable a reduction of the uncertainty on the π^0 efficiency by up to a factor of three over current determinations.

I develop the method starting from a simplified simulated sample comprising τ-pairs only and validate it against samples of known efficiency. Next, I extend the study to a fully realistic simulated sample, demonstrating the feasibility and performance of the method in realistic conditions. Finally, I briefly discuss various aspects of the applicability of the method to data. The results demonstrate that the π^0 efficiency approach conceptually works and yields performances superior to existing Belle II methods.

Sunto

Questa tesi sperimentale di fisica delle particelle esplora un nuovo approccio alla determinazione dell'efficienza di ricostruzione del mesone π^0, la cui incertezza è un limite significativo nella misura di processi sensibili alla fisica oltre il Modello Standard.

L'obiettivo è determinare l'efficienza di ricostruzione del π^0 confrontando i rate di decadimento di $\tau^- \to \pi^- \pi^0 \nu_\tau$ con quelli di $\tau^- \to \pi^- \nu_\tau$ rivelati con il detector Belle II in collisioni elettrone-positrone a SuperKEKB. Dato che questi decadimenti hanno branching fraction grandi e note con alta precisione, sono contaminati da fondi limitati e coprono un ampio spettro d'impulso del π^0, questo approccio permetterebbe di ridurre l'incertezza sull'efficienza del π^0 fino a un fattore tre rispetto alle determinazioni attuali.

Ho sviluppato il metodo partendo da un campione simulato semplificato comprendente solo coppie di leptoni τ e l'ho validato usando campioni di efficienza nota. In seguito, ho esteso lo studio ad un campione simulato completo e con proporzioni realistiche dimostrando la fattibilità e le performance del metodo in queste condizioni. Infine ho discusso brevemente diversi aspetti dell'applicabilità del metodo ai dati. I risultati dimostrano che l'approccio di stima dell'efficienza del π^0 funziona concettualmente e fornisce performance superiori rispetto ai metodi esistenti utilizzati a Belle II.

Contents

Introduction

The Standard Model of elementary particles and their interactions (SM) is the currently accepted theory of particle physics. It is widely recognized as the ultimate success of the reductionist paradigm for describing microphysics at its most fundamental level. By means of about twenty parameters, the Standard Model describes accurately thousands of measurements involving processes mediated by the electromagnetic, weak, and strong interactions that span more than ten orders of magnitude in energy.

However, theoretical considerations and, possibly, experimental inconsistencies support the general belief that the Standard Model might still be an *effective theory* — a theory valid at the energies probed so far, that is incorporated in a yet-unknown and more general theory reaching higher energies. Completing the Standard Model is the principal goal of today's particle physics.

Direct approaches, which broadly consist in searching for decay products of non-SM particles produced on mass-shell in high-energy collisions, have been traditionally fruitful. However, their current reach is limited by the collision energy of today's accelerators and by the large investments needed to further it in future. Complementary approaches consist in comparing with predictions precise measurements in lower-energy processes where virtual non-SM particles could contribute. The reach of such *indirect* approaches is not constrained by collision energy, but rather by the precision attainable, both in measurements and predictions.

The Belle II experiment is an international collaboration of about 700 physicists that *indirectly* tests the Standard Model by studying billions of decays of mesons containing the quarks b and c (heavier and longer-lived partners of the fundamental constituents of ordinary matter) and τ leptons (heaviest partners of the electron). These particles are pair-produced in electron-positron collisions at $10.58\,\mathrm{GeV}$, which is the threshold energy for the production of the $\Upsilon(4S)$ particle (a bound states of a $b\bar{b}$ pair). Since the start of physics data taking in 2019, Belle II collected samples corresponding to $531\,\mathrm{fb}^{-1}$ of integrated luminosity.

Knowledge of the π^0 meson reconstruction efficiency is critical for accurately measuring processes sensitive to physics beyond the Standard Model, as these processes often involve decays into π^0 mesons. The precision on efficiency often represents a significant limitation in the precise determination of the rates of such processes, frequently being the primary source of systematic uncertainty. Improving the knowledge of the π^0 reconstruction efficiency could significantly enhance the precision of various important Belle II analyses.

Several methods have been implemented so far to estimate the π^0 reconstruction efficiency at Belle II using experimental data to correct the determinations based on simulation. However, these approaches are limited by uncertainties in the branching fractions of the channels used, by significant background from other processes, or by the restricted π^0 momentum ranges probed.

This work studies the feasibility of determining such efficiency in data relative to

simulation using a novel approach in Belle II that uses the ratio between the yields of $\tau^- \to \pi^- \pi^0 \nu_\tau$ and $\tau^- \to \pi^- \nu_\tau$ decays reconstructed with the Belle II detector in electron-positron collisions at SuperKEKB.

The π^0 reconstruction efficiency is typically obtained from the ratio of decay rates between channels that differ only by the presence of a π^0 at the numerator, normalized by the branching fractions of the relevant processes. If the initial state is the same for denominator and numerator processes, and all final state particles at the denominator are also final states of the numerator, the ratio of event rates after accounting for the respective branching fractions, isolates the π^0 reconstruction efficiency as the only remaining factor.

The processes considered in my approach are abundant, have well-known branching fractions, have modest background, and span a wide π^0 momentum range. This method, therefore, has the potential to reduce the current uncertainty on the efficiency by significant factor.

The main challenge is to obtain two mutually disjoint samples, as enriched as possible in $\tau^- \to \pi^- \pi^0 \nu_\tau$ and $\tau^- \to \pi^- \nu_\tau$ decays to determine reliably the signal yields needed for the π^0 efficiency. Particular focus is dedicated to suppress background from concurring τ decays and dominant low-multiplicity processes such as Bhabha events. I develop the basic methodology starting from a simplified simulated sample containing only τ pair production events. Subsequently, I apply this method to a fully simulated sample, demonstrating its validity in a realistic conditions.

Comparing the resulting efficiency with the values expected from independent studies allows for a robust validation of the reliability of the method.

This thesis is structured as follows. Chapter 1 introduces the flavor sector of the Standard Model and its potential in indirectly searching for non-SM physics; Chapter 2 describes the Belle II experiment; Chapter 3 outlines the novel approach used for the determination of the π^0 reconstruction efficiency; Chapter 4 reports the τ-analysis generalities, the samples, and the tools used in this work; Chapter 5 describes the efficiency determination in a simulated $\tau^+\tau^-$ sample; Chapter 6 outlines the efficiency estimate in a realistic simulated sample. Finally, Chapter 7 presents an initial comparison between simulated and experimental data and discusses systematic uncertainties. The final chapter, Chapter 8, presents the conclusions.

Charge- and flavor-conjugate processes are implied throughout the document unless specified otherwise.

Chapter 1

Flavor physics to overcome the Standard Model

This is a concise introduction to the weak interactions of quarks and how they are incorporated in the Standard Model of particle physics. Emphasis is on their role in searches for as-yet unknown particles that may complete the Standard Model at high energies. Some focus is devoted to processes where a π^0 meson is present in the final state as these are the processess that would benefit from this work.

1.1 The Standard Model of particle physics

The Standard Model (SM) is an effective quantum field theory that describes all fundamental interactions in nature without gravity [1–6].

The quantum-field-theory framework results from the unification of quantum mechanics with special relativity and offers the most fundamental description of nature known to date.

A field is a set of values, associated to certain physical properties, assigned to every point in space and time. Quantum fields are fields that pervade the whole spacetime and obey the rules of quantum mechanics. If a quantum field is modified by an appropriate perturbation, the resulting oscillatory states, called field excitations, carry more energy than the resting state and are called 'particles'. For instance, the electron is the massive excitation of the electron field. The quantized nature of the description implies that only certain perturbations that satisfy precise energetic conditions are capable of generating field excitations. It is not possible, for example, to generate a wave in the electron field that corresponds to half an electron.

Quantum fields interact with each other. The Standard Model is the theory that describes their dynamics at energy scales relevant for the subnuclear world. Particles and their interactions are described in a Lagrangian formalism, in which every combination of fields and interaction operators that is not forbidden by the symmetries of the dynamics is, in principle, included. Local gauge symmetry, i.e., the invariance of the Lagrangian under space-time-dependent transformations applied to the phases of fields, is the key overarching concept. Interaction terms appear in the free-field Lagrangian after requiring it to be invariant under local gauge symmetries. The Standard Model is based on the symmetry group

$$SU(3)_C \otimes SU(2)_L \otimes U(1)_Y,$$

where $SU(3)_C$ is the standard unitary group that describes the strong interactions (quantum chromodynamics, QCD), and C stands for the color charge; $SU(2)_L \otimes U(1)_Y$ is the

product of groups that describe the combination of the weak and electromagnetic interactions, where $SU(2)_L$ is the standard unitary group of weak isospin doublets (L standing for $left^1$) and $U(1)_Y$ stands for the unitary group of *hypercharge* Y.

Spin-1 particles called *gauge bosons* mediate the interactions. Strong interactions are mediated by eight massless particles corresponding to the $SU(3)_C$ generators, called *gluons*: they carry a charge that can be of three kinds, called *color*. Weak interactions are mediated by two charged massive bosons, $W^{\pm}$, and a neutral massive boson, Z^0. Electromagnetic interactions occur between particles carrying electric charge and are mediated by a neutral massless boson, the photon γ. The physical electroweak bosons ($W^{\pm}$, Z^0, γ) arise from the following linear combinations of $SU(2)_L \otimes U(1)_Y$ generators:

$$W^{\pm} = \frac{1}{\sqrt{2}}(W_1 \mp iW_2) \ \ \text{and} \ \ \begin{pmatrix} \gamma \\ Z^0 \end{pmatrix} = \begin{pmatrix} \cos\theta_W & \sin\theta_W \\ -\sin\theta_W & \cos\theta_W \end{pmatrix} \begin{pmatrix} B \\ W_3 \end{pmatrix},$$

where θ_W is a free parameter, called *Weinberg angle*. The $W^{\pm}$ mass depends on the Z mass via θ_W. Particles acquire mass via the interaction with the Higgs field, which is mediated by a spin-0 particle, the Higgs boson.

Matter particles correspond to excitations of spin-$\frac{1}{2}$ fields and are called *fermions*. Their masses are free parameters of the theory. Each fermion is also associated with an antiparticle that has the same mass and opposite internal quantum numbers. Fermions are further classified into two classes, quarks, which are the fundamental constituents of nuclear matter, and leptons, each organized in three weak-isospin doublets.

- Quark doublets are each composed of an up-type quark, with charge $\frac{2}{3}e$, and a down-type quark, with charge $-\frac{1}{3}e$,

$$\begin{pmatrix} u \\ d \end{pmatrix} \begin{pmatrix} c \\ s \end{pmatrix} \begin{pmatrix} t \\ b \end{pmatrix}.$$

  They couple with both the strong and electroweak interactions. Each quark has color and a 'flavor' quantum number, which comes in six varieties and is conserved in the electromagnetic and strong interactions, but not in the weak interactions. Due to color confinement free quarks are not observable [7]. They are only observed in their colorless bound states, which include mesons, typically composed of a quark and an anti-quark, and baryons, composed of three quarks. Baryons are assigned a quantum number, called baryon number, found to be conserved even if no symmetry of the Lagrangian implies that.

- Lepton doublets are each composed by an almost massless neutral neutrino and a massive particle with electric charge $-e$;

$$\begin{pmatrix} \nu_e \\ e \end{pmatrix} \begin{pmatrix} \nu_\mu \\ \mu \end{pmatrix} \begin{pmatrix} \nu_\tau \\ \tau \end{pmatrix}.$$

  They couple only with the electroweak interaction. Each lepton has a lepton-family quantum number; their sum in a process, called global lepton number, is found to be conserved in all interactions, although no symmetry of the dynamics prescribes that; individual lepton numbers are not conserved in neutrino oscillations.

Figure 1.1 shows a scheme of the Standard Model particles and their interactions.

---

[1]Only particles with *left* chirality are influenced by the weak interaction.
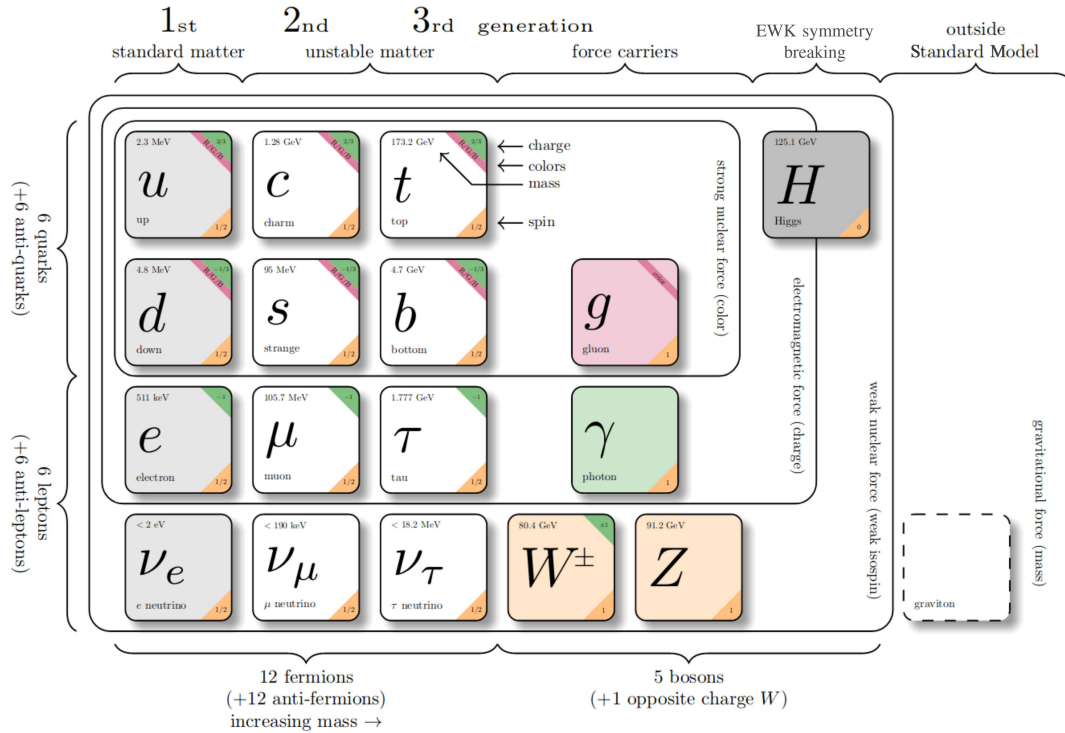
Figure 1.1: Scheme of particles and interactions in the Standard Model [8].

In addition to gauge symmetry, discrete symmetries are important in constraining the dynamics. Parity (P) is a transformation that inverts all spatial coordinates; charge conjugation (C) is the exchange of every particle with its own antiparticle; and time reversal (T) inverts the time axis. The product of these three discrete symmetry transformations is found to be conserved in all interactions, as prescribed by foundational axioms of field theory [9,10], but the symmetries are not conserved individually. Parity symmetry is maximally violated in the weak interactions, while the combined CP symmetry is violated in the weak interactions at the 0.1% level. In principle, the strong interaction too could violate CP symmetry, but no experimental evidence of that has ever been observed. The existence of as-yet unobserved particles, called axions, has been postulated to account for that [11].

1.2 Where do we stand?

The Standard Model was completed in the 1970's and has been successfully tested since, in thousands of measurements whose fractional precisions reach one part per trillion [12]. However, observations and theoretical considerations suggest that the Standard Model is likely to be an effective theory, valid at the eV–TeV energies probed so far, that should be completed by a more general full theory valid over a broader range of high energies. Open questions that support this interpretation include the lack of an explanation for a dynamical origin for the observed asymmetry between matter and antimatter in the universe, the strikingly large differences observed between fermion masses, the possible

instability of the Higgs vacuum, the conceptual and technical difficulties in achieving a description of gravity consistent with quantum mechanics, or the postulated large amounts of non-interacting matter (dark matter), introduced to justify cosmological observations.

Extending the Standard Model to higher energy-scales is the main goal of today's particle physics, in an attempt at addressing these and other open issues. Current strategies to extend the Standard Model can broadly be classified into two synergic approaches.

The energy-frontier, *direct* approach aims at using high-energy collisions to produce on-shell particles (that is, particles satisfying the energy-momentum conservation at production) not included in the Standard Model, and detect directly their decay products, thus gaining direct evidence of their existence.[2] Historically this offered striking experimental evidence of new phenomena, when energetically accessible, but its reach is limited by the maximum energy available at colliders.

The intensity-frontier, *indirect* approach broadly consists in searching for significant differences between precise measurements and equally precise SM predictions in lower-energy processes sensitive to non-SM contributions. A semi-intuitive, although simplified conceptual representation of the subtending idea is that exchanges of virtual (off-mass-shell) particles of arbitrary high mass, including those not described in the Standard Model, occur in the transition, thus altering the amplitudes in an observable manner. The presence of virtual particles, which may imply a temporary non-conservation of energy if interpreted classically, is allowed by Heisenberg's uncertainty principle $\Delta E \Delta t > \hbar/2$. Experimental evidence is typically harder to establish, but the reach is not bounded by the maximum collision energy reachable by experiments. A large portion of the effort in this approach is centered on the weak-interactions of quarks (so called 'flavor physics').

1.3   Flavor physics in the Standard Model

Although technically flavor physics includes also lepton interactions, I restrict the scope by referring solely to the quark interactions here.

The role of flavor in shaping the Standard Model has been central since the early days of particle physics. However, its prominence in determining the theory can perhaps be tracked down to the early 1960's with the apparent inconsistency between weak coupling constants measured in muon decay, neutron decay, and strange-particle decays. Such inconsistency was first addressed by Gell-Mann and Levy [13] and then Cabibbo [14], who postulated differing mass (d) and weak (d') eigenstates for down-type quarks. This was achieved by introducing a mixing angle (θ_C) between the s quark and d quark, the only two down-type quarks known at the time. While Cabibbo's theory addressed efficiently the difference of weak coupling constants, it also predicted a rate for the $K_L^0 \to \mu^+\mu^-$ and other kaon decays inconsistent with the experimental exclusion limits at the time. Glashow, Iliopoulos, and Maiani addressed the conundrum by postulating the existence of a fourth quark (c) of $2\,\text{GeV}/c^2$ mass, whose contribution in the $K_L^0 \to \mu^+\mu^-$ decay amplitude would cancel the u quark contribution, suppressing the branching fraction down to values consistent with experimental limits [15]. The charm quark was then discovered four years after the prediction, showing the compelling power of the indirect approach. In addition, in 1973, when only three quarks were known, Kobayashi and Maskawa generalized Cabibbo's theory from a four-quark model to a six-quark model to accommodate the phenomenon of *CP* violation observed in 1964 [16]. They introduced a complex unitary matrix to describe the

---

[2]*Mass shell* is jargon for mass hyperboloid, which identifies the hyperboloid in energy–momentum space describing the solutions to the mass-energy equivalence equation $E^2 = (pc)^2 + m^2c^4$. A particle *on-mass-shell* satisfies this relation.

relations between mass (unprimed) and weak (primed) interaction eigenstates of quarks as seen by $W^{\pm}$ bosons. This is known as the Cabibbo-Kobayashi-Maskawa (CKM) quark-mixing matrix or V_{CKM},

$$
\begin{pmatrix} d' \\ s' \\ b' \end{pmatrix} = \begin{pmatrix} V_{ud} & V_{us} & V_{ub} \\ V_{cd} & V_{cs} & V_{cb} \\ V_{td} & V_{ts} & V_{tb} \end{pmatrix} \begin{pmatrix} d \\ s \\ b \end{pmatrix} .
$$

Each V_{ij} matrix element encapsulates the weak-interaction coupling between an up-type i and down-type j quarks. It is a $N \times N$ CKM matrix with $(N-1)^2$ free parameters, where N is the number of quarks families [17]. If $N = 2$, the only free parameter is the Cabibbo angle $\theta_C \approx 13°$, whereas if $N = 3$, the free parameters are three Euler angles (θ_{12}, θ_{13}, and θ_{23}) and a complex phase (δ), which allows for CP-violating couplings [12]. The matrix is most conveniently written in the so-called *Wolfenstein parametrization*, an expansion in the small parameter $\lambda = \sin \theta_C \approx 0.23$ that makes explicit the observed hierarchy between its elements [18],

$$
V_{\mathrm{CKM}} = \begin{pmatrix} 1 - \lambda^2/2 & \lambda & A\lambda^3(\rho - i\eta) \\ -\lambda & 1 - \lambda^2/2 & A\lambda^2 \\ A\lambda^3(1 - \rho - i\eta) & -A\lambda^2 & 1 \end{pmatrix} + \mathcal{O}(\lambda^4) \,,
$$

where

$$
\lambda = \frac{V_{us}}{\sqrt{V_{ud}^2 + V_{us}^2}}, \quad A\lambda^2 = \lambda \frac{V_{cb}}{V_{us}}, \quad \text{and} \quad A\lambda^3(\rho + i\eta) = V_{ub}^* \,.
$$

The parameter λ expresses the mixing between the first and second quark generations, A and ρ are real parameters, and η is a complex phase that introduces CP violation. The unitarity condition $V_{\mathrm{CKM}} V_{\mathrm{CKM}}^{\dagger} = \mathbb{1}$ yields nine relations,

$$
\begin{array}{lll}
|V_{ud}|^2 + |V_{cd}|^2 + |V_{td}|^2 = 1 & V_{us}^* V_{ud} + V_{cs}^* V_{cd} + V_{ts}^* V_{td} = 0 & V_{ud} V_{cd}^* + V_{us} V_{cs}^* + V_{ub} V_{cb}^* = 0 \,, \\
|V_{us}|^2 + |V_{cs}|^2 + |V_{ts}|^2 = 1 & V_{ub}^* V_{ud} + V_{cb}^* V_{cd} + V_{tb}^* V_{td} = 0 & V_{ud} V_{td}^* + V_{us} V_{ts}^* + V_{ub} V_{tb}^* = 0 \,, \\
|V_{ub}|^2 + |V_{cb}|^2 + |V_{tb}|^2 = 1 & V_{ub}^* V_{us} + V_{cb}^* V_{cs} + V_{tb}^* V_{ts} = 0 & V_{cd} V_{td}^* + V_{cs} V_{ts}^* + V_{cb} V_{tb}^* = 0 \,,
\end{array}
$$

which are sums of three complex numbers each. The six equations summing to zero prompt a convenient geometric representation in the complex plane in terms of so-called *unitarity triangles*. A CP conserving theory would yield null-area triangles or, equivalently, a vanishing Jarlskog invariant $J = \Im(V_{us} V_{cb} V_{ub}^* V_{cs}^*)$ [19–21]. All elements of the second equation in the second row have similar magnitudes, yielding a notable triangle referred to as 'the Unitarity Triangle', shown in figure 1.2. Conventionally, side sizes are normalized to the length of the base, and the three angles are labelled α or ϕ_2, β or ϕ_1, and γ or ϕ_3.

The flavor-mixing phenomenon, which involves flavored neutral mesons $|M\rangle$, enriches significantly the CP violation phenomenology. Flavor quantum numbers are conserved in strong interactions and thus flavor eigenstates are eigenstates of strong interactions. Weak interactions do not conserve flavor, allowing $|M\rangle$ to undergo a transition into $|\overline{M}\rangle$ (or vice versa), which changes flavor by two units. Because the full Hamiltonian contains strong and weak interactions, its eigenstates (which are the particles we observe, with definite masses and lifetimes) are linear superpositions of flavor eigenstates $|M\rangle$ and $|\overline{M}\rangle$.
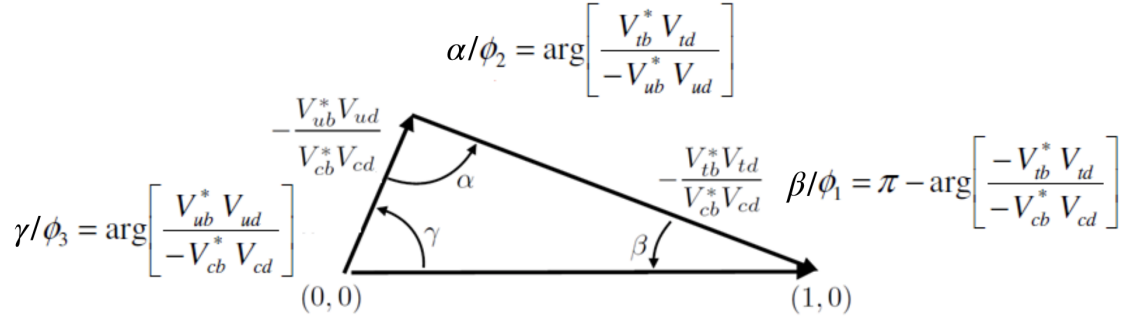
Figure 1.2: Graphical representation of the Unitarity Triangle [8].

1.4 Time evolution of neutral flavored mesons

The time evolution of neutral flavored mesons is approximated by the Schrödinger equation (in Weisskopf-Wigner approximation)

$$i\hbar \frac{\mathrm{d}}{\mathrm{dt}}|\psi\rangle = \mathcal{H}_{\text{eff}}|\psi\rangle,$$

where the effective Hamiltonian $\mathcal{H}_{\text{eff}}$ is a 2×2 complex matrix that can be decomposed into a mass and a decay matrix

$$\mathcal{H}_{\text{eff}} = \boldsymbol{M} - \frac{i}{2}\boldsymbol{\Gamma},$$

and $\boldsymbol{M}$ and $\boldsymbol{\Gamma}$ are hermitian matrices. The effective Hamiltonian $\mathcal{H}_{\text{eff}}$ is not hermitian and thus probability is not conserved. This corresponds to the decrease in the total number of mesons due to decay. The diagonal elements of $\boldsymbol{M}$ and $\boldsymbol{\Gamma}$ are related respectively to the mass and the lifetime of the pure flavor eigenstates. Conservation of CPT symmetry requires that the M and the $\bar{M}$ mesons have the same mass and the same lifetime implying that $M_{11} = M_{22} = M$ and $\Gamma_{11} = \Gamma_{22} = \Gamma$. These diagonal elements are determined by the quark masses and by strong and electromagnetic interactions. Thus, the diagonal elements of $\mathcal{H}_{\text{eff}}$ can be identified as the strong and electromagnetic Hamiltonian $\mathcal{H}_0$. On the other hand, the off-diagonal elements have to fulfill $M_{12} = M_{21}^*$ and $\Gamma_{12} = \Gamma_{21}^*$ due to hermiticity of $\boldsymbol{M}$ and $\boldsymbol{\Gamma}$. These elements involve weak interactions and can be considered as a weak perturbation Hamiltonian $\mathcal{H}_{\text{w}}$. One obtains

$$\mathcal{H}_{\text{eff}} = \begin{pmatrix} H_0 & 0 \\ 0 & H_0 \end{pmatrix} + \mathcal{H}_{\text{w}} = \begin{pmatrix} M - \frac{i}{2}\Gamma & M_{12} - \frac{i}{2}\Gamma_{12} \\ M_{12}^* - \frac{i}{2}\Gamma_{12}^* & M - \frac{i}{2}\Gamma \end{pmatrix}. \tag{1.1}$$

Since the phase factors of $|M\rangle$ and $|\bar{M}\rangle$ can be arbitrarily adjusted without changing the physics, only the difference between them, ϕ_{12}, is relevant. Flavor mixing is parametrized by five real parameters [22]

$$M_{11}, \quad \Gamma_{11}, \quad |M_{12}|, \quad |\Gamma_{12}| \quad \text{and} \quad \phi_{12} = \arg\left(-\frac{M_{12}}{\Gamma_{12}}\right).$$

By diagonalizing the Hamilton operator in Eq.(1.1), the time evolution of the meson-antimeson system gets described in terms of its eigenvalues

$$\omega_{\pm} = M - \frac{i}{2}\Gamma \pm \sqrt{(M_{12} - \frac{i}{2}\Gamma_{12})(M_{12}^* - \frac{i}{2}\Gamma_{12}^*)} = M - \frac{i}{2}\Gamma \pm pq \tag{1.2}$$

and the associated eigenstates $v_{\pm} = (1, \pm\frac{q}{p})^{\mathrm{T}}$, which represent the physical eigenstates

$$|M_+(t)\rangle \equiv p|M(t)\rangle + q|\bar{M}(t)\rangle,$$
$$|M_-(t)\rangle \equiv p|M(t)\rangle - q|\bar{M}(t)\rangle. \tag{1.3}$$

As an example, figure 1.3 shows the leading-order Feynman diagrams contributing to $B^0 - \overline{B}^0$ mixing. Flavor mixing induces flavor oscillations in the time evolution of neutral flavored mesons. Flavor oscillations generate additional time-evolution paths to the simple decay, which interfere with the decay thus enriching the dynamics and our opportunities to study it.
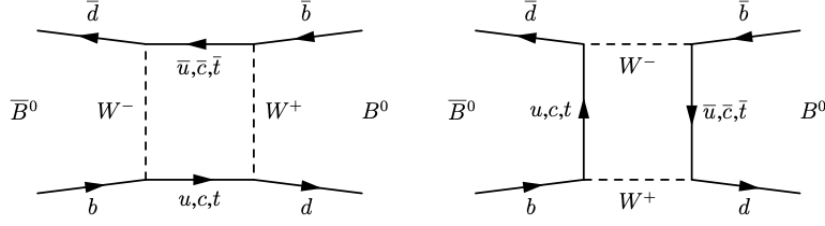
Figure 1.3: Feynman diagrams for leading-order amplitudes contributing to $B^0 - \overline{B}^0$ mixing [8].

The complex numbers p and q satisfy

$$\frac{q}{p} = \sqrt{\frac{M_{12}^* - \frac{i}{2}\Gamma_{12}^*}{M_{12} - \frac{i}{2}\Gamma_{12}}} = e^{-i\phi_M}\sqrt{\frac{|M_{12}| + \frac{i}{2}|\Gamma_{12}|e^{i\phi_{12}}}{|M_{12}| + \frac{i}{2}|\Gamma_{12}|e^{-i\phi_{12}}}} \quad \text{with } |p|^2 + |q|^2 = 1, \tag{1.4}$$

where the absolute mixing weak phase $\phi_M \equiv \arg(M_{12})$ is introduced. The mass eigenstates $|M_\pm(t)\rangle$ are pure CP eigenstates if they are orthogonal to each other (even and odd states). This is the case when the phase ϕ_{12} is zero or an odd multiple of π, i.e., if the absolute value of $|q/p|$ is equal to 1. The masses $m_\pm$ and the lifetimes $\Gamma_\pm$ for the mass eigenstates states are derived from the eigenvalues in Eq. (1.2),

$$m_+ = \mathrm{Re}(\omega_+), \qquad\qquad \Gamma_+ = -2\mathrm{Im}(\omega_+),$$
$$m_- = \mathrm{Re}(\omega_-), \qquad\qquad \Gamma_- = -2\mathrm{Im}(\omega_-),$$

which can be recast in terms of the following observables:

$$m \equiv \frac{1}{2}(m_+ + m_-) = M, \qquad \Gamma \equiv \frac{1}{2}(\Gamma_+ + \Gamma_-) = \Gamma = \frac{1}{\tau},$$
$$\Delta m \equiv m_- - m_+ = -2\mathrm{Re}\,(pq), \qquad \Delta\Gamma \equiv \Gamma_- - \Gamma_+ = 4\mathrm{Im}\,(pq).$$

The time evolution of $|M_\pm\rangle$ is given by

$$|M_+(t)\rangle = e^{-i\omega_+ t}\left(p|M\rangle + q|\bar{M}\rangle\right),$$
$$|M_-(t)\rangle = e^{-i\omega_- t}\left(p|M\rangle - q|\bar{M}\rangle\right), \tag{1.5}$$

where both mass eigenstates decay as $e^{-\Gamma_\pm t}$ with a modulation generated by the complex phase $e^{im_\pm}$. Considering now Eq.(1.3), the time evolution of the pure flavor states reads

$$|M(t)\rangle \equiv \frac{1}{2p}\left(|M_+(t)\rangle + |M_-(t)\rangle\right),$$
$$|\bar{M}(t)\rangle \equiv \frac{1}{2q}\left(|M_+(t)\rangle - |M_-(t)\rangle\right).$$

Insertion of the time evolution in Eq.(1.4) yields

$$
\begin{aligned}
|M(t)\rangle &= \frac{1}{2}\left(\left(e^{-i\omega_+ t} + e^{-i\omega_- t}\right)|M\rangle + \frac{q}{p}\left(e^{-i\omega_+ t} - e^{-i\omega_- t}\right)|\bar{M}\rangle\right) \\
&= \frac{1}{2}e^{-i\omega_+ t}\left(\left(1 + e^{-i(\Delta m - \frac{i}{2}\Delta\Gamma)t}\right)|M\rangle + \frac{q}{p}\left(1 - e^{-i(\Delta m - \frac{i}{2}\Delta\Gamma)t}\right)|\bar{M}\rangle\right), \quad (1.6)
\end{aligned}
$$

$$
\begin{aligned}
|\bar{M}(t)\rangle &= \frac{1}{2}\left(\frac{p}{q}\left(e^{-i\omega_+ t} - e^{-i\omega_- t}\right)|M\rangle + \left(e^{-i\omega_+ t} + e^{-i\omega_- t}\right)|\bar{M}\rangle\right) \\
&= \frac{1}{2}e^{-i\omega_+ t}\left(\frac{p}{q}\left(1 - e^{-i(\Delta m - \frac{i}{2}\Delta\Gamma)t}\right)|M\rangle + \left(1 + e^{-i(\Delta m - \frac{i}{2}\Delta\Gamma)t}\right)|\bar{M}\rangle\right). \quad (1.7)
\end{aligned}
$$

With non vanishing Δm and $\Delta\Gamma$, which are related to the weak off-diagonal components of the Hamiltonian M_{12} and Γ_{12}, an initial pure flavor state will mix with its opposite flavor state before it decays. Thus, decay rates can be only properly defined if the initial state is specified either as $|M\rangle$ or as $|\bar{M}\rangle$ [23]. Starting with a specific flavor eigenstate $|M\rangle$ at $t = 0$, and taking into account the orthogonality between flavor eigenstates, the probability to observe the state $|\bar{M}\rangle$ at time t is

$$
|\langle\bar{M}|M(t)\rangle|^2 = \frac{1}{2}\left|\frac{q}{p}\right|^2 e^{-\Gamma t}\left(\cosh\left(\frac{\Delta\Gamma t}{2}\right) - \cos(\Delta m t)\right), \quad (1.8)
$$

and to observe $|M\rangle$ is

$$
|\langle M|M(t)\rangle|^2 = \frac{1}{2}e^{-\Gamma t}\left(\cosh\left(\frac{\Delta\Gamma t}{2}\right) + \cos(\Delta m t)\right). \quad (1.9)
$$

The time evolutions of the transition amplitudes are

$$
A_f(t) = \langle f|\mathcal{H}|M(t)\rangle = A e^{-\frac{\Gamma t}{2}}\left(\cos\frac{\Delta m t}{2} + i\lambda\sin\frac{\Delta m t}{2}\right)
$$

$$
\overline{A}(t) = \langle f|\mathcal{H}|\overline{M}(t)\rangle = \overline{A} e^{-\frac{\Gamma t}{2}}\left(\cos\frac{\Delta m t}{2} + \frac{i}{\lambda}\sin\frac{\Delta m t}{2}\right),
$$

and the time-dependent asymmetries are

$$
\begin{aligned}
a_f &= \frac{\Gamma(M \to f) - \Gamma(\overline{M} \to f)}{\Gamma(M \to f) + \Gamma(\overline{M} \to f)} \\
&= \frac{|\lambda|^2 - 1}{1 + |\lambda|^2}\cos(\Delta m t) + \frac{2\,\mathrm{Im}(\lambda)}{1 + |\lambda|^2}\sin(\Delta m t) \\
&= \mathcal{A}_{CP}\cos(\Delta m t) + \mathcal{S}_{CP}\sin(\Delta m t),
\end{aligned}
$$

where $\mathcal{A}_{\mathrm{CP}}$ is the direct CP-violation parameter, and $\mathcal{S}_{\mathrm{CP}}$ is the mixing-induced CP-violation parameter. These are two of the three manifestations of nonconservation of charge-parity symmetry. Indeed, depending on how the CP-violating complex phase enters the amplitude of the dynamical evolution of a system, CP violation can be classified into three distinct phenomenologies. In the most general case, one considers the amplitudes of transitions governed by the effective Hamiltonian $\mathcal{H}_{\mathrm{eff}}$, of a flavored meson $|M\rangle$ and of its antiparticle $|\overline{M}\rangle$, into a final state $|f\rangle$ and into the CP conjugate $|\overline{f}\rangle$, respectively,

$$
\begin{aligned}
A_f &= \langle f|\mathcal{H}_{\mathrm{eff}}|M\rangle = A\left(|M\rangle \to |f\rangle\right), & \overline{A}_f &= \langle f|\mathcal{H}_{\mathrm{eff}}|\overline{M}\rangle = A\left(|\overline{M}\rangle \to |f\rangle\right), \\
A_{\overline{f}} &= \langle\overline{f}|\mathcal{H}_{\mathrm{eff}}|M\rangle = A\left(|M\rangle \to |\overline{f}\rangle\right), & \overline{A}_{\overline{f}} &= \langle\overline{f}|\mathcal{H}_{\mathrm{eff}}|\overline{M}\rangle = A\left(|\overline{M}\rangle \to |\overline{f}\rangle\right).
\end{aligned}
$$

Violation of CP symmetry *in decay* occurs if

$$\left|\frac{A_f}{\overline{A}_{\overline{f}}}\right| \neq 1 \;\text{ or }\; \left|\frac{\overline{A}_f}{A_{\overline{f}}}\right| \neq 1, \tag{1.10}$$

and appears experimentally as a difference between the $|\overline{M}\rangle \to |\overline{f}\rangle$ and $|M\rangle \to |f\rangle$ decay rates. This is the only CP-violation phenomenology possible for both neutral and charged mesons, and for baryons. Since, in general, various amplitudes contribute to a single decay, the total decay amplitudes A_f and $\overline{A}_{\overline{f}}$ are written as sums of the individual contributions

$$A_f = \sum_i |A_i| e^{i(\delta_i + \phi_i)}, \qquad \overline{A}_{\overline{f}} = \sum_i |A_i| e^{i(\delta_i - \phi_i)},$$

where symbols δ_i indicate CP-conserving phases, and ϕ_i are CP-violating phases associated with the elements of the CKM matrix that appear in each amplitude. As CP-conserving couplings are real, the corresponding phases are invariant under CP transformation. Since a CP transformation turns CKM coefficients into their complex conjugate, the CP-violating phases flip their sign. The condition of CP violation in decay in Eq. (1.10) is satisfied if

$$|A_f|^2 - |\overline{A}_{\overline{f}}|^2 = -2 \sum_{i,j} |A_i||A_j| \sin(\delta_i - \delta_j) \sin(\phi_i - \phi_j) \neq 0.$$

Thus, CP violation in decay can occur only if at least two amplitudes with different CP-conserving and CP-violating phases contribute to the relevant decay process. The squared magnitudes of the total decay amplitudes $|A_f|^2$ and $|\overline{A}_{\overline{f}}|^2$ are the quantities typically accessible experimentally since they are proportional to the total decay rates. The individual amplitudes A_i are often difficult to compute theoretically as they typically involve contributions from strong-interaction amplitudes at low energy. These are non-perturbative and therefore hard to calculate, leading to large uncertainties. Thus, observables that depend only on the weak phases, such as the CKM angles, allow for sensitive and reliable SM test.

Violation of CP symmetry *in mixing* implies

$$\left|\frac{q}{p}\right| = \left|\frac{1-\varepsilon}{1+\varepsilon}\right| \neq 1 \;\Rightarrow\; |\varepsilon| \neq 0, \tag{1.11}$$

where q and p are introduced in Eq. (1.2). In this case, CP violation generates a difference between the flavor-oscillation rates $|M\rangle \to |\overline{M}\rangle$ and $|\overline{M}\rangle \to |M\rangle$, which can be observed as a charge-dependent asymmetry in the yields of charged leptons from semileptonic decays of oscillating B^0 mesons.

Violation of CP symmetry *in the interference* of mixing and decay is observed when the neutral mesons $|M\rangle$ and $|\overline{M}\rangle$ can decay into a common final state $|f\rangle$, preferentially a pure CP eigenstate f_{CP},

$$CP|f_{CP}\rangle = \pm|f_{CP}\rangle.$$

Even if CP is conserved in mixing and in decay separately, i.e., if $|\overline{A}_{f_{CP}}/A_{f_{CP}}| = |q/p| = 1$, the combination of the decay and mixing phases can generate a total phase difference and thus an interference between these two processes, generating a violation of CP symmetry. Introducing the complex quantity λ_{CP}, the condition for CP violation is

$$\text{Im}(\lambda_{CP}) \neq 0, \quad \text{where} \quad \lambda_{CP} \equiv \frac{q}{p} \cdot \frac{\overline{A}_{f_{CP}}}{A_{f_{CP}}} = \left|\frac{q}{p}\right| \cdot \left|\frac{\overline{A}_{f_{CP}}}{A_{f_{CP}}}\right| e^{-i(\phi_M + \phi_D)}.$$

1.5 Flavor physics to overcome the Standard Model

Many physicists find the current understanding of flavor dynamics unsatisfactory. The observed hierarchies between quark masses and couplings seem too regular to be accidental and the abundance of free parameters (six quark masses and four couplings) suggests the possibility of a deeper, more fundamental theory possibly based on a reduced set of parameters. In addition, while the CKM mechanism offers a framework to include CP violation in the Standard Model, it does not really enlighten the origin for such a singular phenomenon.

But even in the absence of a deeper understanding of the origin of CP violation, naturalness arguments indicate that most generic extensions of the Standard Model would involve additional sources of CP violation. These and other considerations support the notion that a more detailed and complete study of the phenomenology of quarks dynamics may reveal useful information to guide searches for SM extensions.

The abundance and diversity of experimentally accessible processes to measure redundantly a reduced set of parameters makes indirect searches in the flavor sector a powerful option for exploring non-SM dynamics. In fact, even if no deviations from the Standard Model will be found, the resulting stringent constraints on SM extensions are expected to remain useful in informing future searches.

The two classes of flavor-physics processes most promising for probing contributions of non-SM particles are *flavor-changing-neutral-currents* and *CP-violating* processes.

Flavor-changing neutral currents (FCNC) are processes in which quark flavor changes in the transition, but quark electric charge does not. The processes are suppressed in the Standard Model, because they occur only through higher-order amplitudes involving the internal exchange of $W^\pm$ bosons ('loop amplitudes'), as shown in figure 1.4. Such amplitudes are naturally sensitive to non-SM contributions, since any particle with proper quantum numbers and nearly arbitrary mass can replace the SM-quark closed-line in these diagrams thus altering the rate. Hence, FCNC are powerful in signaling contributions from non-SM particles if rate enhancements, or suppressions, with respect to Standard Model expectations are observed.

In addition to rate alterations, the phenomenon of CP violation offer additional avenues to uncover or characterize possible non-SM contributions. Alterations of the CP-violating phases with respect to those predicted by the SM are generically expected in a broad class of SM-extensions. Observing experimental evidence of those phases offers further opportunities to explore the dynamics, even if total rates are unaffected.

1.6 Current flavor status

Measurements of parameters associated with quark-flavor physics have been performed in many dedicated, or general-purpose, experiments in the last three decades, including CLEO, CPLEAR, NA32, NA48, NA62, KTeV, SLD, OPAL, L3, ALEPH, DELPHI, BaBar, Belle, CDF, CDFII, LHCb, BESIII, ATLAS, CMS and Belle II [24].

The current status of constraints on sides and angles of the Unitarity Triangle is shown in figure 1.5 [25]. Measurements of $\sin 2\beta$ reached a precision of 1%, mainly due to the availability of large samples of $B^0 \to J/\psi K^0$ decays in e^+e^- and pp collisions, while the angle α is known down to a 4% precision from $B \to hh$ decays, and h represents a charged or neutral π or ρ) in e^+e^- collisions. The angle γ is measured with 4% precision using combinations of several measurements involving $B \to DK$ decays reconstructed in e^+e^- and pp collisions. Discrepancies in the determinations of $|V_{cb}|$ and $|V_{ub}|$ are found between
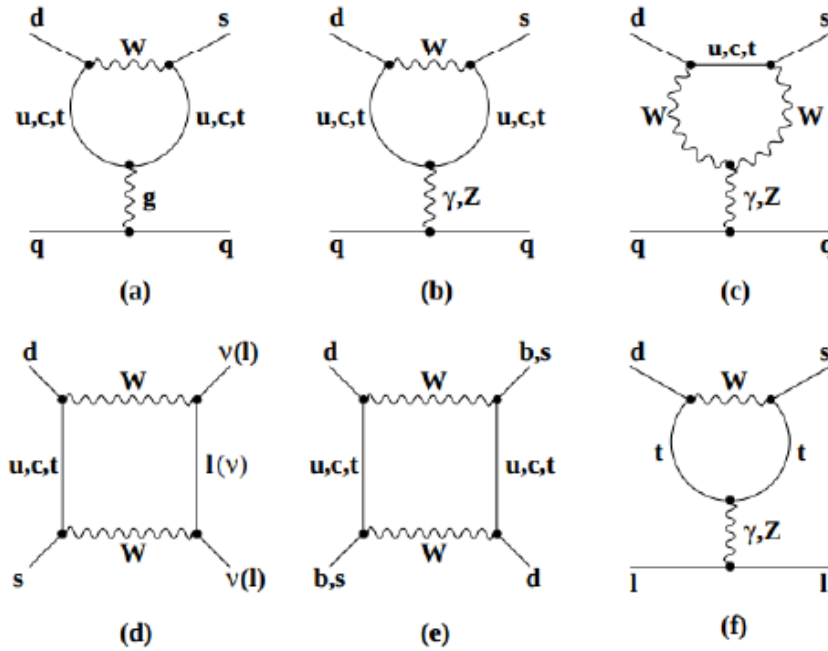
Figure 1.4: Examples of leading FCNC diagrams [8].

values measured using different analyses of semileptonic decays, mainly performed in e^+e^- collisions.

The decay-width difference of the $B_s^0 - \overline{B}_s^0$ system is determined with 5% precision in pp collisions, while measurements are not yet precise enough to discern the expected non-zero value for the $B^0 - \overline{B}^0$ system. Mass differences in both systems are known with better than 1% precision from pp and $p\bar{p}$ collisions. In addition, many other measurements in charm and kaon physics contribute that are not straightforwardly represented in the Unitarity Triangle.

The resulting global picture is that the CKM interpretation of quark-flavor phenomenology is the dominant mechanism at play in the dynamics. Despite the first-order consistency of the experimental flavor picture with the CKM theory, possible deviations of up to 10%–15% are still unconstrained, especially those associated with loop-mediated processes, leaving sufficient room for non-SM physics. It is especially promising that most of the relevant measurements are currently dominated by statistical uncertainties, offering therefore fruitful opportunities for the two experiments that will contribute the most in the next decade, LHCb and Belle II.

This is all the more attractive because recent direct searches for non-SM physics, mainly in pp collisions at the Large Hadron Collider (LHC) at CERN, excluded large portions of the parameter space for several proposed SM extensions, but showed no conclusive evidence of non-SM physics to date. Since plans for a higher-energy collider in the near future are still fluid, the systematic study of flavor physics emerges as a promising program to search for non-SM in the next decade.

1.7 Channels with π^0 in the final states

This thesis proposes a novel method in Belle II for the determination of the π^0 meson reconstruction efficiency using one-prong decays of the τ lepton. The π^0 efficiency represents
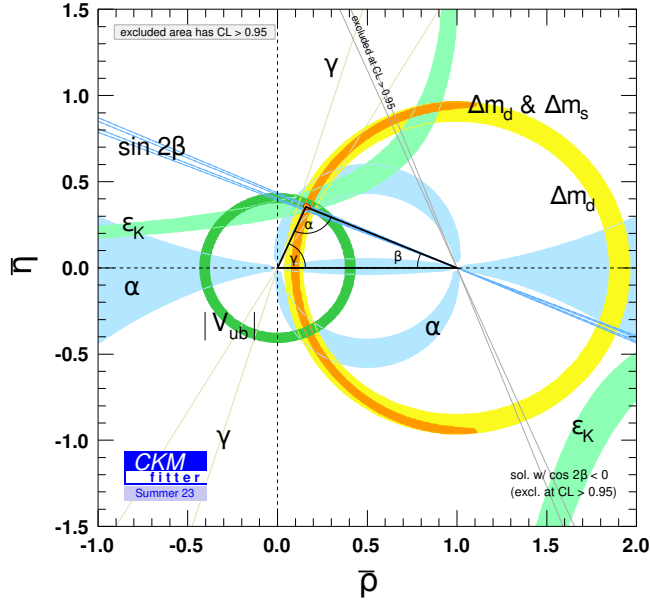
Figure 1.5: Current constrains on sides and angles of the Unitarity Triangle. Reproduced from Ref. [25]

the main contribution to systematic uncertainties in many processes sensitive to physics beyond the Standard Model, and is therefore a fundamental ingredient to make the most out of Belle II measurements. A few examples of such processes are discussed below.

1.7.1 $B^0 \to J/\psi\,\pi^0$

Precise measurements of the CKM angle $\beta = \phi_1 = arg\,(-V_{cd}V_{cb}^*/V_{td}V_{tb}^*)$, where V_{ij} are CKM matrix elements, have been performed in decays to CP eigenstates mediated by $b \to c\bar{c}s$ transitions. In the SM, the direct and mixing-induced CP asymmetries are predicted to be $C_{b\to c\bar{c}s} = 0$ and $-\eta S_{b\to c\bar{c}s} = \sin 2\phi_1$ with very high accurancy, where η is the CP eigenvalue of the decay final state. Current world-average values, $C_{b\to c\bar{c}s} = -0.005 \pm 0.015$ and $-\eta S_{b\to c\bar{c}s} = 0.699 \pm 0.017$ [12], agree with independent constraints on the CKM matrix. However, higher-order amplitudes (also called "penguin") can induce a shift in measurements of ϕ_1, thereby limiting the sensitivity of CKM fits. The decay $B^0 \to J/\psi\,\pi^0$, which proceeds via suppressed tree-level $b \to c\bar{c}s$ transitions, is used to constrain the contributions from penguin topologies in the extraction of ϕ_1.

In particular, the branching fraction is used to probe the size of non-factorizable $SU(3)$-breaking effects, which are the main contribution to the theoretical uncertainties in the extraction of the penguin parameters. The current world-average of the branching fraction, which does not include yet a recent measurement from LHCb, is $\mathcal{B}(B^0 \to J/\psi\,\pi^0) = (1.66 \pm 0.10) \times 10^{-5}$ [12]. This is dominated, in precision, by a Belle measurement $\mathcal{B}(B^0 \to J/\psi\,\pi^0) = (1.62 \pm 0.11\,(\text{stat}) \pm 0.06\,(\text{syst})) \times 10^{-5}$ [26]. The systematic uncertainty is 3.7%. A significant (16%) contribution to this uncertainty is due to the uncertainty in the π^0 reconstruction efficiency. This is just one example that highlights the importance of this efficiency.

1.7.2 $B^0 \to \pi^0 \pi^0$

The decay of the neutral bottom-meson into a pair of neutral pions, $B^0 \to \pi^0 \pi^0$, is important in the study of the weak interactions of quarks. The properties of this decay can be used to constrain parameters of potential processes not described by the Standard Model; allow to test phenomenological models of hadronic bottom-meson amplitudes and refine their parameters; and provide important inputs for the determination of $\alpha = \phi_2$, a fundamental parameter in flavor-changing weak interactions of quarks.

Theoretical predictions for the branching fraction $\mathcal{B}(B^0 \to \pi^0 \pi^0)$ are challenging because the calculation of hadronic amplitudes involves low-energy, nonperturbative gluon exchanges. Current approximate methods that reduce the associated hadronic unknowns often fail to reproduce data. Predictions based on QCD factorization and perturbative QCD are approximately five times smaller than the experimental results. In addition, the ratio of color-suppressed to color-allowed tree amplitudes, as inferred from other charmless two-body decay modes, does not agree with expectations, possibly indicating anomalously large electroweak-penguin contributions. An improved understanding of the $B^0 \to \pi^0 \pi^0$ branching fraction could be relevant to the so-called $B \to K \pi$ puzzle [27].

The branching fraction plays also a role in the determination of ϕ_2. Given the contributions from both $b \to u$ (W emission, or tree) and $b \to d$ (W exchange, or penguin) transitions in the decay amplitude, the determination of ϕ_2 requires measurements of the branching fractions and CP asymmetries of the full set of isospin-related $B \to \pi \pi$ decay modes, i.e., $B^0 \to \pi^+ \pi^-$, $B^0 \to \pi^0 \pi^0$, and $B^+ \to \pi^+ \pi^0$. Isospin relations then allow the penguin and tree contributions to be separated. Currently, the uncertainty in the $B^0 \to \pi^0 \pi^0$ branching fraction is an important limiting factor in the determination of ϕ_2. The world-average value $\mathcal{B}(B^0 \to \pi^0 \pi^0) = (1.59 \pm 0.26) \times 10^{-6}$ [12] combines measurements reported by the BaBar and Belle collaborations, but suffer from large uncertainties, partly due to the uncertainty in π^0 reconstruction efficiency. For example, the most recent result reported by the Belle II collaboration, reads $\mathcal{B}(B^0 \to \pi^0 \pi^0) = (1.38 \pm 0.27 \,(\text{stat}) \pm 0.22 \,(\text{syst})) \times 10^{-6}$ [28]. The systematic uncertainty is 16%. The dominant (50%) contribution to this uncertainty is due to the π^0 reconstruction efficiency, which shows the importance of this factor in accurately determining the branching ratio. These are just two examples, out of many, that demonstrate the importance of understanding and controlling the precision of our knowledge of the π^0 reconstruction efficiency, and the potential impact of improving it.

1.8 Generalities on τ decays

Since this work is based on samples of τ decays, we briefly outline a few relevant generalities.

The τ is the only known lepton massive enough to decay into hadrons. It therefore offers access to a large breadth of useful dynamical information regarding the strong and weak interactions. However, in this work we only use them as a convenient probe for the π^0 efficiency so we do not include here any discussion on τ lepton physics.

In this work, we use the three-body decay $\tau^- \to \pi^- \pi^0 \nu_\tau$ and the two-body decay $\tau^- \to \pi^- \nu_\tau$. Figure 1.6 illustrates the tree level Feynman diagrams for the two channels considered. The decay $\tau^- \to \pi^- \pi^0 \nu_\tau$ occurs via an intermediate state dominated by the $\rho(770)$ meson resonance, while the decay $\tau^- \to \pi^- \nu_\tau$ is mediated by a virtual charged vector boson W. The branching fractions are known with high accuracy namely 0.35% for $\mathcal{B}\left(\tau^- \to \pi^- \pi^0 \nu_\tau\right) = (25.49 \pm 0.09)\%$ and 0.46% for $\mathcal{B}\left(\tau^- \to \pi^- \nu_\tau\right) = (10.82 \pm 0.05)\%$. Such accuracy enables our approach to target hypothetical precision on the order

of subpercent.
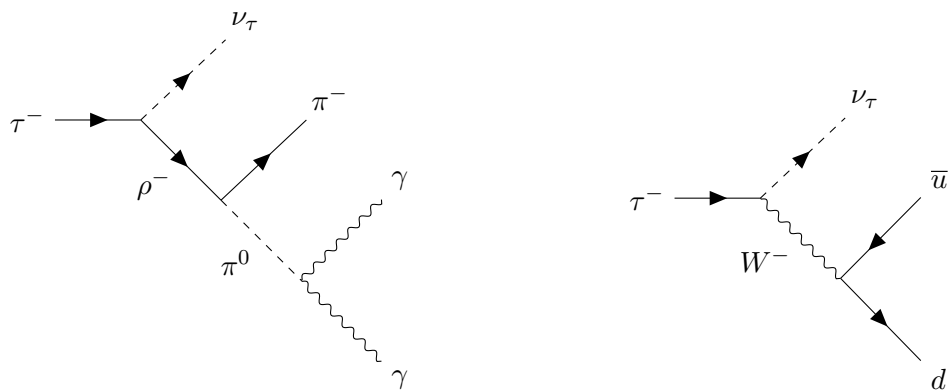
Figure 1.6: Dominant Feynman diagrams for $\tau^- \to \pi^0 \pi^- \nu_\tau$ (left) and $\tau^- \to \pi^- \nu_\tau$ (right).

Chapter 2

The Belle II experiment at the SuperKEKB collider

The data used in this work are collected by the Belle II experiment. This chapter outlines the Belle II detector at the SuperKEKB accelerator, with emphasis on the subdetectors more relevant for the reconstruction of $\tau^- \to \pi^- \left(\pi^0\right) \nu_\tau$ decays.

2.1 The SuperKEKB collider

SuperKEKB is an electron-positron (e^+e^-) energy-asymmetric collider, designed to produce more than 600 $B\overline{B}$ pairs per second ($B^0\overline{B}^0$ and B^+B^- in approximately equal proportions) via decays of $\Upsilon(4S)$ mesons produced at threshold [29]. Such colliders are called 'B-factories', and were proposed in the 1990's for the dedicated exploration of CP violation in B mesons. The main goal of B-factories is to produce low-background quantum-correlated $B\overline{B}$ pairs at high rates and with sufficient boost to study their time evolution.

Intense beams of electrons and positrons are brought to collision at the energy corresponding to the $\Upsilon(4S)$ meson mass, $10.58\,\text{GeV}$, which is just above the $B\overline{B}$ production kinematic threshold. The great majority of collisions yield electromagnetic processes as $e^+e^- \to e^+e^-$, $e^+e^- \to \mu^+\mu^-$, $e^+e^- \to \tau^+\tau^-$, $e^+e^- \to \gamma\gamma$ etc., see figure 2.1; the rest are collisions that produce hadrons (henceforth called hadronic events). Figure 2.2 shows the hadron-production cross-section in e^+e^- collisions as a function of the final-state mass. The various peaks are radial excitations of the Υ meson. They overlap the nearly uniform background at about 4 nb from so-called continuum of lighter-quark pair-production from the process $e^+e^- \to q\overline{q}$, where q identifies a u, d, c, or s quark. These are useful for charm physics, some selected topics in hadron physics, and as control channels. The rest are $\Upsilon(4S)$ events, which decay to $B\overline{B}$ pairs more than 96% of the time. At-threshold production implies little available energy to produce additional particles in the $B\overline{B}$ events, resulting in low-background conditions. In addition, colliding beams of point-like particles imply precisely known collision energy, which sets stringent constraints on the collision's kinematic properties, thus offering means of further background suppression. Since bottom mesons are produced in a strong-interaction decay, flavor is conserved, and the null net bottom content of the initial state implies production of a flavorless $B\overline{B}$ pair. Even though B^0 and $\overline{B}^0$ undergo flavor oscillations before decaying, their time-evolution is quantum-correlated in such a way that no B^0B^0 or $\overline{B}^0\overline{B}^0$ pairs are present at any time. Angular-momentum conservation implies that the decay of the spin-1 $\Upsilon(4S)$ in the two spin-0 bottom mesons yields total angular momentum $J = 1$. Because the simultaneous presence of two identical

particles in an antisymmetric state would violate Bose statistics, the system evolves coherently as an oscillating $B^0\overline{B}^0$ particle-antiparticle pair until either one decays. This allows efficient identification of the bottom (or antibottom) content of one meson at the time of decay of the other, if the latter decays in a final state accessible only by either bottom or antibottom states. This important capability is called 'flavor tagging' and allows measurements of flavor-dependent decay rates, as needed in many determinations of CP-violating quantities.
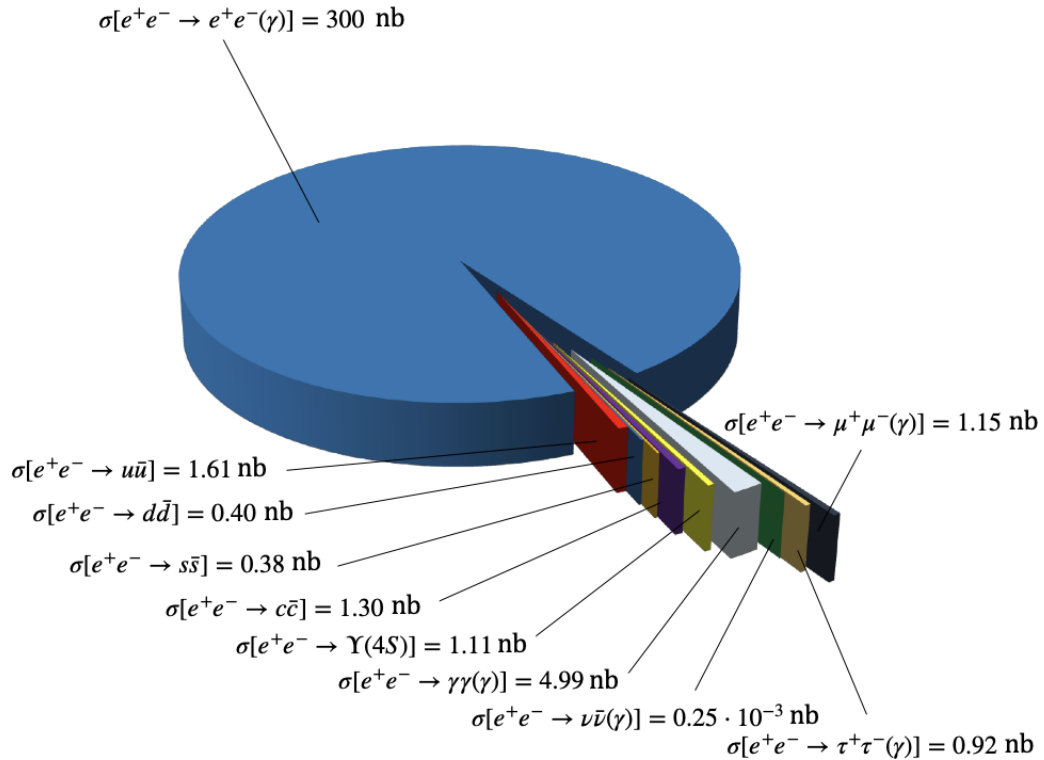
Figure 2.1: Pie chart of the cross sections for the main processes produced in e^+e^- collision at the $\Upsilon(4S)$ center-of-mass energy [8].

Because the $\Upsilon(4S)$ mesons are produced at threshold, they would be nearly at rest in the laboratory in an energy-symmetric collider. The resulting B mesons too would be produced with low momentum (about $10\,\mathrm{MeV}/c$) in the laboratory, because of the $21\,\mathrm{MeV}/c^2$ difference between the $\Upsilon(4S)$ mass and the $B\overline{B}$ pair mass. With such low momenta they would only travel approximately $1\,\mu$m before decaying, rendering the $10\,\mu$m typical spatial resolution of vertex detectors insufficient to separate B-decay vertices and study the decay-time evolution. Asymmetric beam energies are used to circumvent this limitation. By boosting the collision center-of-mass along the beam in the laboratory frame, B-decay vertex separations are achieved that are resolvable with current vertex detectors [31]. SuperKEKB (figure 2.3) implements a 7–on–4 GeV energy-asymmetric double-ring design, which achieves a vertex displacement of about $130\,\mu$m.

Electrons are produced in a thermionic gun with a barium-impregnated tungsten cathode, then accelerated to 7 GeV with a linear accelerator (linac) and injected in the high-energy ring (HER). Positrons are produced by colliding electrons on a tungsten target, then isolated by a magnetic field, accelerated to 4 GeV with the linac and injected in the low-energy ring (LER).
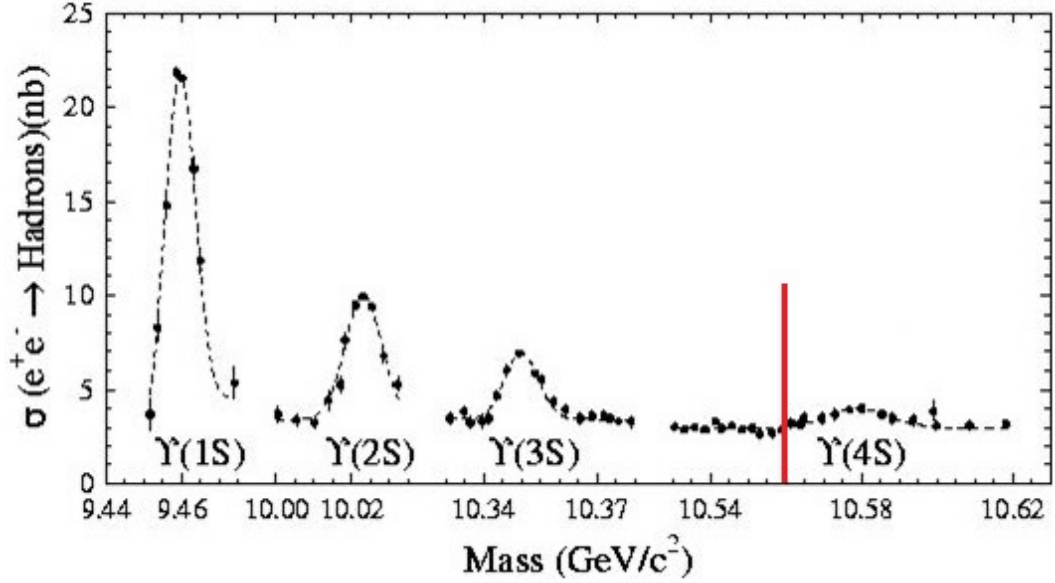
Figure 2.2: Hadron production cross section from e^+e^- collisions as a function of the final-state mass. The vertical red line indicates the $B\overline{B}$ production threshold [30].

The electrons and positrons continuously collide at a single interaction point, surrounded by the Belle II detector. To achieve high luminosities, a nano-beam, large crossing-angle collision scheme is implemented [33]. This is an innovative configuration based on keeping small horizontal and vertical emittance, which is a measure of the spread and size of the particle beam in the phase space of position and momentum, and large crossing angle, as shown in figure 2.4. Such configuration is obtained with the production of low emittance beams, in addition to a sophisticated final-focus superconducting-quadrupole-magnet system, made of magnets, corrector coils, and compensation solenoids installed at each longitudinal end of the interaction region. Conceptually the nano-beam scheme mimics a collision with many short micro-bunches, allowing significant advantages in luminosity with respect to previous conventional schemes. The reduction of the luminous volume size to about 5% with respect to the predecessor KEKB, combined with doubled beam currents, is expected to yield a factor 40 gain in intensity. The penalty for such high intensities are significant challenges in achieving the design performance and operating steadily, and higher beam-induced backgrounds.

The performance of the SuperKEKB collider is mainly characterized in terms of the instantaneous luminosity $\mathcal{L}$, which is a measure of collision intensity,

$$\mathcal{L} = \frac{\gamma_\pm}{2er_e}\left(1 + \frac{\sigma_y^*}{\sigma_x^*}\right)\frac{I_\pm \xi_{y\pm}}{\beta_{y\pm}^*} \cdot \frac{R_\mathcal{L}}{R_{\xi_y}},$$

where γ is the relativistic Lorentz factor, e is the absolute value of the electron charge, r_e is the classical radius of the electron, σ_x^* and σ_y^* are the bunch widths at the interaction point (IP) in the plane orthogonal to the beam direction (transverse plane), I is the current of the beam, β_y^* is the vertical betatron function at the IP [35], ξ_y is the vertical beam-beam parameter, $R_\mathcal{L}$ and R_{ξ_y} are the luminosity reduction factors and the vertical beam-beam parameter, respectively, due to non-vanishing crossing angle [36]. The ratio of these reduction factors is close to unity, while the design values for the other parameters are reported in table 2.1.

The rate of any given process
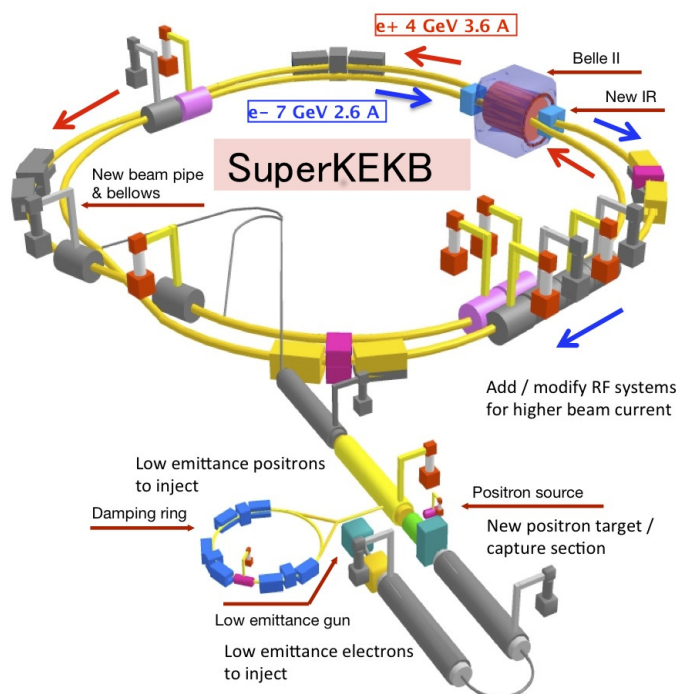
Figure 2.3: Illustration of the SuperKEKB collider [32].

$$\text{rate [events s}^{-1}] = \mathcal{L} \text{ [cm}^{-2} \text{ s}^{-1}] \times \sigma \text{ [cm}^2],$$

is the product of its cross-section and $\mathcal{L}$.

	Design	Achieved (as of late 2024)
Energy [GeV]	4.0/7.0	4.0/7.0
ξ_y	0.090/0.088	0.0407/0.0279
β_y^* [mm]	0.27/0.41	1.0/1.0
I [A]	3.6/2.62	1.321/1.099

Table 2.1: Design and achieved values for SuperKEKB fundamental parameters (LER/HER).

The integral of instantaneous luminosity over time T, called integrated luminosity,

$$\mathcal{L}_{\text{int}} = \int_0^T \mathcal{L}(t')dt'$$

is a measure of the number of produced events of interest $N = \mathcal{L}_{\text{int}}\sigma$.

Physics data-taking started in March 2019, and Belle II has integrated $531\,\text{fb}^{-1}$ of luminosity at the time of this writing. In 2022, SuperKEKB achieved the instantaneous-luminosity world record, 4.7×10^{34} cm^{-2}s^{-1}. In spite of these achievements, a number of technological and scientific challenges have significantly reduced SuperKEKB performance compared to design. A number of issues associated with beam injection, collimation, and short beams lifetime due to the reduction of their dynamic aperture, which also causes high uncontrollable beam backgrounds, limited the capability to deliver the expected samples of data in its first five years. Consolidation, improvement and development work is ongoing to overcome these difficulties.
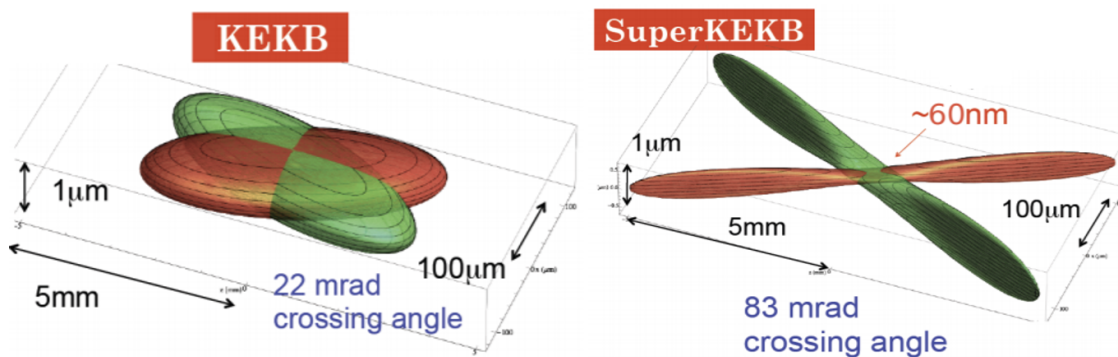
Figure 2.4: Two-dimensional sketch of the nano-beam mechanism implemented in SuperKEKB (right) compared with the previous KEKB collision scheme (left) [34].

2.2 The Belle II detector

Belle II (figure 2.5) is a large-solid-angle, multipurpose magnetic spectrometer surrounded by a calorimeter and particle-identification systems, installed around the SuperKEKB interaction point. It is designed to determine energy, momentum, and identity of a broad range of particles produced in 10.58 GeV e^+e^- collisions. Belle II is approximately a cylinder of about 7 m in length and 7 m in diameter. It employs a right-handed Cartesian coordinate system with origin in the interaction point. The z axis corresponds to the principal axis of the solenoid, which is approximately parallel to the electron beam direction at the interaction point; the y axis points vertically upward, and the x axis is horizontal and pointing outward of the accelerator tunnel. The polar angle, θ, is referred to the positive z axis. The azimuthal angle, ϕ, is referred to the positive x axis in the xy plane. The radius, $r = \sqrt{x^2 + y^2}$, is defined in cylindrical coordinates and measured from the origin in the xy plane. Throughout this thesis, *longitudinal* means parallel to the electron beam direction (to the z axis), and *transverse* means perpendicular to the electron beam direction, i.e., in the xy plane.

Belle II comprises several subsystems, each dedicated to one or few specific aspects of event reconstruction. From the interaction point outward, a particle would traverse the beam pipe, a two-layer silicon-pixel vertex-detector (PXD), a four-layer silicon-strip vertex-detector (SVD), a central wire drift-chamber (CDC), a time-of-propagation central Cherenkov counter (TOP) or an aerogel threshold forward Cherenkov counter (ARICH), an array of CsI(Tl) crystals (ECL), a superconducting solenoidal magnet, and multiple layers of resistive plate counters (KLM).

The principal experimental strengths are hermetic coverage, which allows for reconstruction of final states involving neutrinos; efficient and precise reconstruction of charged-particle trajectories (tracks), which provide accurately reconstructed decay-vertices and good momentum resolution; high-purity charged-particle identification and neutral-particle reconstruction. A summary of the technological specifications of the Belle II subsystems is in table 2.2. A detailed description of Belle II and its performance is in Ref. [37]. In the following, I focus on the electromagnetic calorimeter, which is the subdetector more relevant for the analysis reported in this thesis.

Figure 2.5: Top view of Belle II, the beam pipe at IP and final-focus magnets [38].

Purpose	Acronym	Technology	Configuration	Channels	Polar coverage (θ)
Beam pipe		Beryllium	Cylindrical, inner radius 10 mm, 10 μm Au, 0.6 mm Be, 1 mm paraffin, 0.4 mm Be		
Tracking	PXD	Silicon pixel	Sensor size: 15×(L1 136, L2 170) mm², Pixel size: 50×(L1a 50, L1b 60, L2a 75, L2b 85) μm²; two layers at radii: 14, 22 mm	10^6	[17°;150°]
	SVD	Silicon strip	Rectangular and trapezoidal, strip pitch: 50(p)/160(n) - 75(p)/240(n) μm, with one floating intermediate strip; four layers at radii: 38, 80, 115, 140 mm	2.45×10^5	[17°;150°]
	CDC	Drift chamber with He-C_2H_6 gas	14336 wires in 56 layers, inner radius of 160mm outer radius of 1130 mm	1.4×10^5	[17°;150°]
	Solenoid	Solenoid coil	Length: 4.41 m. Radius: 1.80 m		
Particle ID	TOP	RICH with quartz radiator	16 segments in ϕ at $r \approx 120$ cm, 275 cm long, 2cm thick quartz bars with 4×4 channel MCP PMTs	8×10^3	[31°;128°]
	ARICH	RICH with aerogel radiator	2×2 cm thick focusing radiators with different n, HAPD photodetectors	7.8×10^4	[14°;30°]
Calorimetry	ECL	CsI(Tl) crystals	Barrel: $r = 125-162$cm, end-cap: $z = -102 - +196$cm	6624 (Barrel), 1152 (FWD), 960 (BWD)	[12.4°;31.4°], [32.2°;128.7°], [130.7°;155.1°]
Muon ID	KLM	Barrel: RPCs and scintillator strips	2 layers with scintillator strips and 12 layers with 2 RPCs	θ 1.6×10^4, ϕ 1.6×10^4	[40°;129°]
	KLM	End-cap: scintillator strips	12 layers of (7-10)×40 mm² strips	1.7×10^4	[25°;40°], [129°;155°]

Table 2.2: Summary of the Belle II subdetectors and their specifications.

The beam pipe is a 3 km-long vacuum enclosure to allow beams circulating inside the detector. In the following, I refer only to the straight section of the beam pipe surrounding the interaction point. Multiple Coulomb scattering in the beam-pipe wall of the final-state charged particles would spoil the vertex-position resolution; this dictates a thin beam-pipe wall made of a low-Z material. Moreover, since the vertex resolution is inversely proportional to the distance between the interaction point and the track sampling, the beam pipe has to be narrow. The possibility for beam-halo to interact with the beam pipe, thus inducing beam backgrounds, and heating of the pipe wall due to charge induction complicates the design. Hence, the beam pipe is constantly cooled and shielded from the vertex detector. The Belle II beam pipe is made of two beryllium cylinders, 0.6 mm-thick at radius of 10 mm, and 0.4 mm-thick at radius of 12 mm, respectively. A 1.0 mm gap between the inner and outer walls of the pipe is filled with paraffin for cooling. The beam pipe is coated with a 10 μm gold sheet that absorbs low-energy photons, which could damage the silicon detector.

2.2.1 Tracking system

At Belle II, reconstruction of charged particles and ensuing measurement of their momenta and charges is achieved through an integrated system consisting of six layers of silicon and a drift chamber, surrounding the beam pipe and immersed in a 1.5 T axial magnetic field maintained in a cylindrical volume 3.4 m in diameter and 4.4 m in length. The field is oriented along the z direction and provided by an aluminum-stabilized superconducting solenoid made of NbTi/Cu alloy. The solenoid surrounds all the subdetectors up to the KLM. The iron yoke of the detector serves as the return path of the magnetic flux.

2.2.1.1 Silicon-pixel vertexing detector

The innermost detector is a pixel vertex detector [39]. Its goal is to sample the trajectories of final-state charged particles in the vicinity of the decay position (vertex) of their long lived ancestors, so that the decay point can be inferred by extrapolation inward.

PXD sensors are based on the technology of depleted field-effect transistors [39]. They are made of p-channel MOSFET integrated on a silicon substrate, which is fully depleted by applying an appropriate voltage. Incident particles generate electron-hole pairs in the depleted region. The charge carriers drift towards the minimum of potential placed under the transistor channel, and thus modulate a current passing through the MOSFET. Sensors are 75 μm thick.

The PXD has two layers at 14 mm and 22 mm radii, respectively, and a full length of 174 mm at the radius of the outer layer. It comprises around 8 million pixels, $50 \times (50 - 55)\mu$m^2 (inner layer) and $50 \times (70 - 85)\mu$m^2 (outer layer) each. The polar acceptance ranges from 17° to 150°. The design impact-parameter resolution is 12 μm, achieved by weighting the charge deposited in neighboring pixels.

2.2.1.2 Silicon-strip vertexing detector

Around the PXD is SVD, a silicon detector aimed at reconstructing decay vertices and low-momentum charged-particles at high resolution [40].

It uses double-sided silicon strip sensors. Each sensor is made of a silicon n-doped bulk on one side, and a perpendicular highly p-doped implant on the other side. This means that, for each sensor, one side has strips parallel to the beams direction, and the other perpendicular. A voltage is applied to enhance the depletion region at the p-n junction,

and removes intrinsic charge-carriers from the region. Traversing charged particles ionize the silicon, freeing electron-hole pairs that drift due to the electric field thus inducing a signal in highly granular strip electrodes implanted at both ends of the depletion region. The fine segmentation and fast charge collection of SVD sensors make possible to deal with high track-density environments.

The SVD structure consists of four concentric layers at radii of 39, 80, 104 and 135 mm, composed by, respectively, 7, 10, 12, and 16 independently-readout longitudinal modules arranged in a cylindrical geometry. As shown in figure 2.6, SVD has a polar-asymmetric geometry that mirrors the asymmetry in particle density resulting from the center-of-mass boost. The polar acceptance ranges from 17° to 150°.

Sensors are 300 μm thick, and the separation between adjacent strips (d_{pitch}) ranges from 50 μm to 240 μm. Hence, the nominal spatial resolution $d_{pitch}/\sqrt{12}$ varies with the polar angle. Since the charge associated with an incident particle is usually distributed among several strips, position resolution is improved by interpolation.
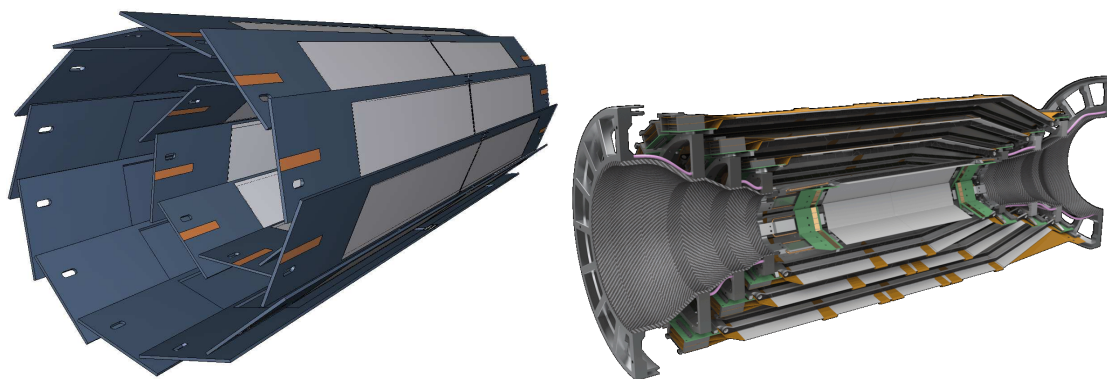
Figure 2.6: (Left) sketch of the PXD detector [41] and (right) exploded view of a SVD detector half [42].

2.2.1.3 Central drift chamber

The CDC is a drift chamber [43]. It samples charged-particle trajectories at radii between 16 cm and 113 cm, thus providing accurate measurements of momentum and electric charge, trigger information for events containing charged particles, and information on identification of charged-particle species by measuring their specific-ionization energy-loss (dE/dx). Between SVD and CDC, a small section with 2.5 cm radius is present.

When a charged particle traverses the CDC volume, it ionizes the gas, freeing electrons and positive ions from gas atoms. A stationary electric field then accelerates these charges until they approach the sense wires. In their vicinity high field gradients cause an abrupt acceleration that causes secondary ionizations, which induce an electric signal whose time is digitized. The particle trajectory is inferred from the time between the collision and the signal.

The chamber volume contains 14336 30-μm-diameter sense wires, divided in 56 layers, immersed in a gaseous mixture of 50% He and 50% C_2H_6, while 42240 126-μm-diameter aluminum wires shape the electric field. Layers of wires are installed with either "axial" orientation, i.e., aligned with the solenoidal magnetic field, or skewed with respect to the axial wires with a "stereo" orientation. The azimuthal acceptance ranges from 17° to 150°.

The spatial resolution is about 100 μm and the dE/dx resolution is 11.9% for an incident angle of 90°. Figure 2.7 shows a sliced schematic representation of the CDC and the wire

configurations.
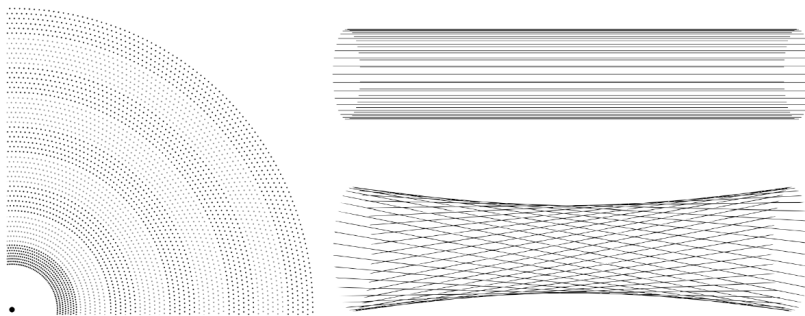
Figure 2.7: A transverse quadrant of the drift chamber, organized in layers, called *super-layers* (left); wire orientation for axial (top right) and stereo (bottom right) layers. Skew is exaggerated for visualization purposes [44].

2.2.2 Electromagnetic calorimeter

The ECL measures the energy of photons and electrons [45]. High energy photons and electrons entering the calorimeter initiate an electromagnetic shower through bremsstrahlung and electron-positron pair production. The energy is mostly converted to photons, which are collected by the photodiodes. In contrast to hadrons, which pass through the calorimeter with minimal energy loss, most photons and electrons dissipate their entire energy.

The configuration, mechanical structure, and crystals of Belle II ECL are those of the calorimeter of the predecessor experiment, Belle. The readout electronic boards have been upgraded to cope with SuperKEKB's higher luminosity. The layout is shown in figure 2.8. The ECL consists of three polar compartments: the barrel, the forward endcap, and the backward endcap section. The barrel section is 3.0 m long with 1.25 m of inner radius; the endcaps are located at $z = +2.0$ m (forward) and -1.0 m (backward) from the interaction point. Table 2.3 summarizes the geometrical parameters of each section.

Item	θ coverage	θ segmentation	ϕ segmentation	Number of crystals
Forward endcap	12.4°–31.4°	13	48–144	1152
Barrel	32.2°–128.7°	46	144	6624
Backward endcap	130.7°–155.1°	10	64–144	960

Table 2.3: Summary of ECL parameters.

Efficient π^0 detection is essential in this work and requires good separation of two nearby photons and a precise determination of the opening angle. This requires a segmented calorimeter. The ECL is a highly segmented array of 8736 cesium iodide crystals doped with thallium (CsI(Tl)). Thallium shifts the energy of the excitation light into the visible spectrum. The light is detected by a independent pair of silicon PIN photodiodes [45] and charge-sensitive preamplifiers installed at the outer end of each crystal.

A typical crystal in the barrel section has a 55×55 mm^2 active surface on the front face and 65×65 mm^2 on the rear face; the dimensions of the crystals in the endcap sections vary from 44.5 to 70.8 mm and from 54 to 82 mm for front and rear faces, respectively. A
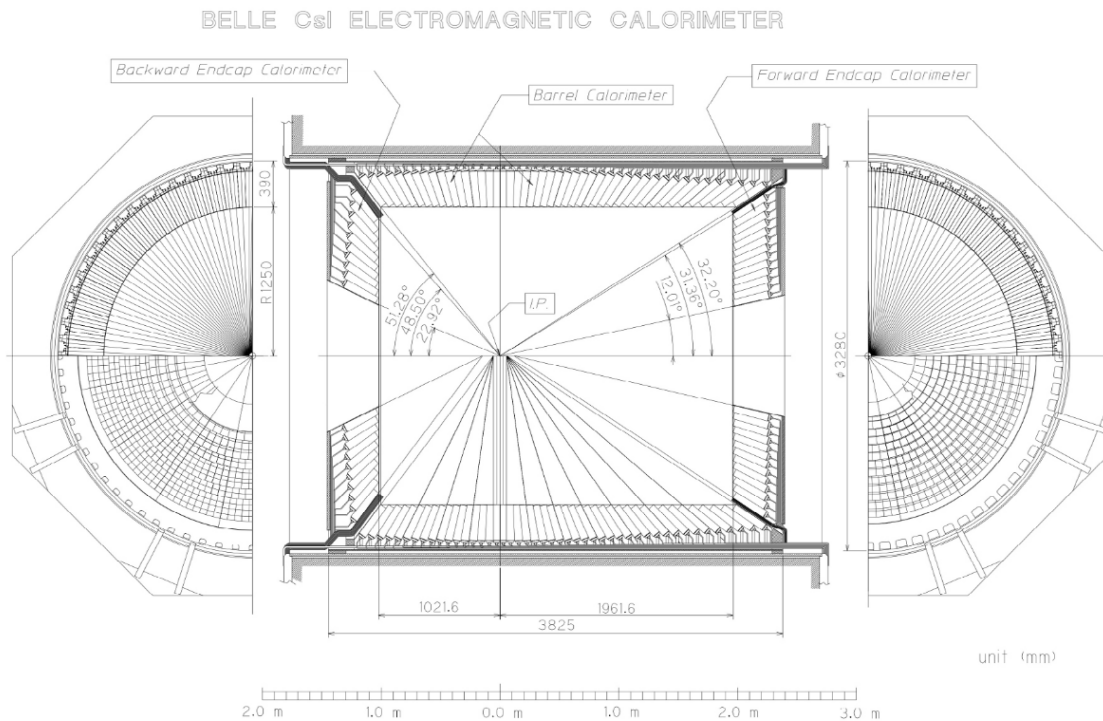
Figure 2.8: ECL layout [38].

diagram of an ECL crystal is shown in figure 2.9. The 30-cm crystal length, corresponding to $16.1X_0$, reduces the fluctuations of shower leakages out of the outermost end of the crystals, which spoils energy resolution. The crystals are designed in such a way that a photon injected at the center of the crystal would deposit 80% of its energy in the crystal on average. The principal axes of the crystals do not point exactly to the nominal interaction point, but they are inclined to prevent photons from escaping through gaps by about 1.3° in the θ and ϕ directions in the barrel section, and by about 1.5° and about 4° in the θ direction in the forward and backward sections.

Considering the ECL structure – gaps, crystal wrapping, mechanical structure – the fraction of photons that do not leave a detectable signal in the calorimeter is only 0.2%.
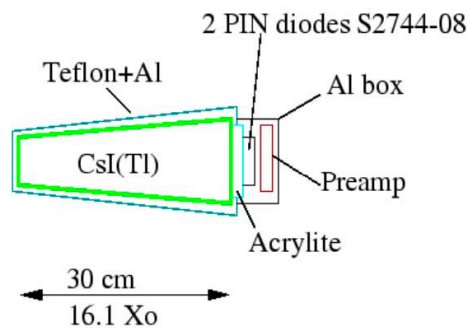
Figure 2.9: Schematic design of a CsI(Tl) crystal with attached readout electronic circuits [46].

Signals from the photodiodes are sent to two preamplifiers mounted on the rear of the crystal for charge integration. The two resulting signals are sent to a readout board [45] located outside the Belle II detector and containing 16 analog shaper circuits. These channels receive signals from up to 16 CsI(Tl) crystals. A total of 576 shaper modules are needed to process signals from all 8736 crystals. Shaper circuits amplify and shape the analog signal to provide a well-defined pulse while removing noise, pile-up due to overlapping pulses from neighboring events, and other unwanted features from the signal. The signal is sampled by a digitizer at 1.76 MHz, which corresponds to an interval between measurements of 567 ns. After collecting 31 samples, the signal waveform is processed using a photon template fit to compute the signal amplitude of the signal, the time relative to the trigger signal, and the χ^2 fit quality. The first 16 samples (pedestal) contain information about the baseline value, while the remaining 15 samples, from the 16th to the 31st sample, contain the signal waveform. In data, the pedestal is not uniform, but shows fluctuations due to electronic noise and backgrounds not coming from collisions. An example of a fit is shown in figure 2.10.
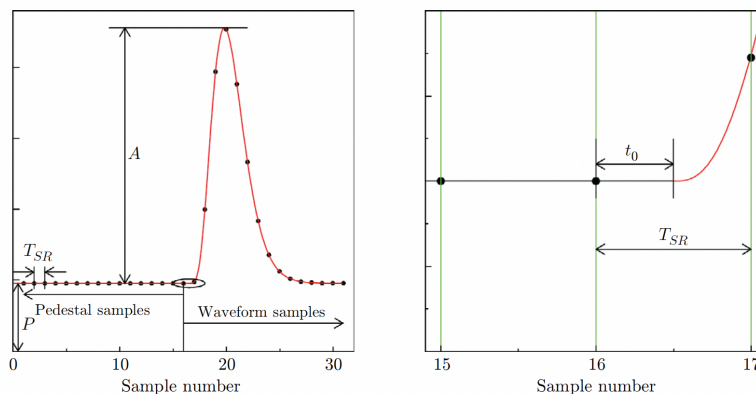
Figure 2.10: Fit to the 31 samples containing the pedestal and the signal waveform (left), and focus on the 16th sample, where the signal starts (right) in simulation [47].

The signal waveforms are analyzed using pulse-shape discrimination to improve particle identification, since the signal decay time in CsI(Tl) includes a fast component of around 0.6 μs and a slow component of around 3.5 μs. The fast component is associated with the scintillation response to electromagnetic interactions, while the slow component is associated with the scintillation response to hadronic (e.g., proton or neutron) interactions. This occurs because scintillation in CsI(Tl) for electromagnetic interactions involves the excitation and deexcitation of Tl atoms, while scintillation for hadronic interactions involves the excitation and deexcitation of both Tl and Cs atoms, leading to a longer decay time. The ratio between the intensity of these two decay components varies as a function of the ionizing power of the absorbed particle. When analyzing the shape of the scintillation pulse, the shape discrimination can help to distinguish between these different types of particles. The photon emission spectrum peaks at around 550 nm, which is convenient for photodiode readout. However, the time for the light in the crystals to decay is relatively long, increasing considerably the overlap of pulses from neighboring (background) events.

This means that scintillation light may be present when a particle from a later event arrives, generating pile-up background.

The ECL also uses Bhabha scattering to measure luminosity. Because the Bhabha cross section is predicted with high accuracy in QED, a precise inference of luminosity is achieved from the measured rate of Bhabha events in an instrumented volume of known acceptance.

2.2.3 Particle identification

Belle II combines measurements of time-of-propagation, Cherenkov radiation, and ionization energy loss in the tracker and drift chamber to identify charged particles.

2.2.3.1 Time-of-propagation detector

The TOP detector measures the time of propagation of the Cherenkov photons emitted from charged particles passing through its quartz bars and internally reflected within a radiator [48]. It is made of 16 quartz bars mounted at 1.2 m from the IP. Each bar has three main components (figure 2.11): a long bar acts as Cherenkov radiator, where photons are generated and propagated; a focusing mirror is mounted at the forward end; and a prism mounted at the backward end collects photons and guides them to a photomultiplier. The polar coverage ranges from 31° to 128°. On average, photons originated from slower particles take more time to reach the photomultipliers, because of the inverse proportionality between β and $\cos\theta_C$.
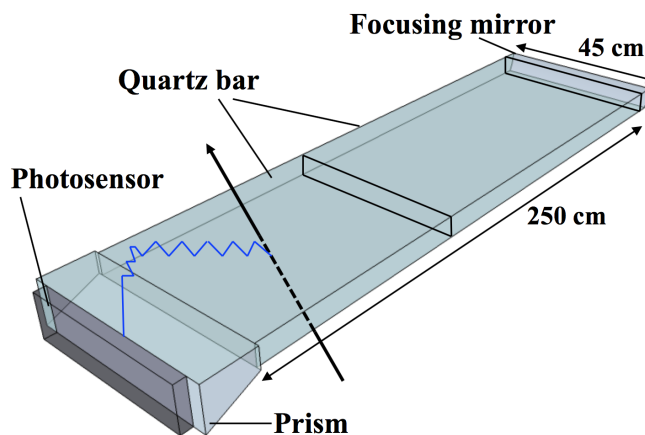
Figure 2.11: Scheme of a TOP bar. A charged particle crossing the radiator and emitting Cherenkov photons, which are collected at the photomultipliers, is also represented [49].

2.2.3.2 Aerogel ring-imaging Cherenkov counter

The ARICH detector identifies charged particles by measuring the Cherenkov ring produced when passing through a radiator [50]. It consists of 420 modules for photon detection in seven layers extending from 0.56 to 1.14 m radius, and 248 aerogel tiles installed on the detector endcaps. The aerogel radiator produces Cherenkov photons when traversed by charged particles of a certain momentum range. Next to the radiator is an expansion volume where photons are propagated, to form rings on position-sensitive photodiodes. Photocathodes then convert photons into photoelectrons and generate electric signals. Two

adjacent radiators with different refraction indexes generate enough photons for achieving sufficient resolution, as shown in figure 2.12.
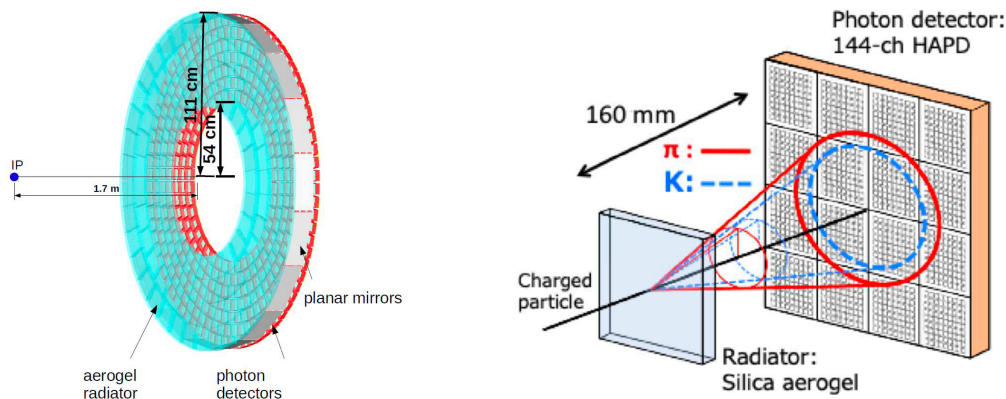
Figure 2.12: Sketch of (left) the ARICH with its main components [51] and (right) diagram of the difference in the photon path for Cherenkov photons from kaons and pions [50].

2.2.3.3 K_L^0 and muon detection system

The KLM detects muons and neutral particles that do not get absorbed in the inner detectors, such as K_L^0 mesons [52]. It is made of alternating 4.7-cm-thick iron plates and active detector elements. Iron elements act also as magnetic flux returns for the tracking solenoid. In the inner layers, the active material is scintillator, in the outer layers are glass-electrode resistive-plates chambers, with a gas mixture filling the space between electrodes. When particles traverse the KLM, they produce charges that are collected by applying an appropriate voltage. The barrel section of the detector covers $45°$ to $125°$ in polar angle. The endcaps cover $20°$ to $45°$ and $125°$ to $155°$.

2.2.4 Trigger and data acquisition system

The e^+e^- collisions at the $\Upsilon(4S)$ resonance produce a variety of processes. As the events of interest are only a fraction of the total cross section and it would be impossible to record all collisions on permanent memory, an online event-selection system (trigger) is used to distinguish them from background in real time, and to feed only the interesting events to the data acquisition system (DAQ), compatibly with data processing resources. The physics processes of interest include hadronic, μ/τ-pair, Bhabha, and two photon events. Accept rates of Bhabha and $\gamma\gamma$ events, which have high cross section and can be identified by their distinct signature, are artificially reduced by a factor of 100 to comply with the data acquisition limitations. Preferably discarded events include beam-related background resulting from synchrotron radiation, scattering of the beams on the residual gas, interactions in the beam pipe, and cosmic-ray events.

The Belle II trigger is organized according to a two-level logic, with a level 1 (L1) hardware trigger followed by a software-based, high-level trigger (HLT).

The L1 trigger, designed for a maximum rate of 30 kHz, uses input from four sub-detectors: (i) the CDC, which provides three-dimensional track information to suppress tracks not originating from the interaction point; (ii) the ECL, which gives information on total energy deposit and cluster multiplicity; (iii) the TOP, which provides timing and hit topology information; and (iv) the KLM, which gives high-efficiency trigger for muons.

These are used to achieve a low-level reconstruction that is fed to the global decision logic, which sends the proper trigger signal if the event passes the selection requirements. The L1 logic is implemented using field-programmable gate arrays that have a fixed latency of $5\,\mu s$, with an uncertainty on the trigger timing (jitter) of approximately 10 ns.

Expected cross sections and trigger accept rates for physics processes of interest at the design instantaneous luminosity of $8\times10^{35}\mathrm{cm}^{-2}\mathrm{s}^{-1}$ are given in table 2.4.

Process	σ [nb]	Rate [Hz]
$e^+e^- \to \Upsilon(4S)$	1.2	960
$e^+e^- \to q\bar{q}$ $(q=u,d,s,c)$	2.8	2200
$e^+e^- \to \mu^+\mu^-$	0.8	640
$e^+e^- \to \tau^+\tau^-$	0.8	640
$e^+e^- \to e^+e^-$ (Bhabha scattering) $\theta_{lab} > 17°$	44	350*
$e^+e^- \to \gamma\gamma$ $\theta_{lab} > 17°$	2.4	19*
Two photon events ($\theta_{lab} > 17°$ and $p_T \geq 0.1$ GeV/c)	≈ 80	≈ 1500

Table 2.4: Expected cross sections and trigger rates of various physics processes at $8\times10^{35}\mathrm{cm}^{-2}\mathrm{s}^{-1}$ luminosity [37]. Bhabha and $\gamma\gamma$ accept rates (*) are artificially reduced by a factor of 100 to comply with the data acquisition limitations.

Events selected by the L1 trigger are input to the HLT, that makes a decision using information from all the subdetectors except for PXD. The online software reconstruction is similar to that used offline. A first selection, performed after the first step of the reconstruction and aimed at discarding about half of the events, is based on requirements on track multiplicity, vertex position, and total ECL energy deposit. After the remaining steps of the standard reconstruction are completed, further physics-level selection are performed. After this stage, the number of events is reduced to about 1/5 of those passing the L1 trigger. The efficiency of the HLT for $\Upsilon(4S) \to B\bar{B}$ events is higher than 99%.

Data from the PXD for events that pass the L1 selection are stored in a dedicated online data reduction system. Once an event passes the selection, HLT extrapolates the tracks found by CDC and SVD to the PXD layers, defining regions of interest (ROIs). These are passed to the data reduction system, and only hits matching with a ROI are transmitted to the DAQ system. This keeps the PXD data size to about 100 kB/event.

Fully reconstructed events are stored in DST files. The size of a DST of a typical hadronic event is 100 kB. The large amount of information stored in DST files is reduced into mini-DST to isolate subsets of events of physics processes of interest like hadronic or τ pairs events. The size of a mini-DST of an hadronic event is around 40 kB.

2.3   Reconstruction of stable particles

Reconstruction is the process through which raw data collected by the detectors are transformed into manageable physics information, in terms of quantity, quality, and proximity to data-analysis-ready quantities. Several algorithms use low-level objects (detector signals, alignment, and calibration information) combined with our knowledge of relativistic kinematics to produce higher-level objects (tracks, energy deposits, etc). In the work described in this thesis I use information associated to two types of stable particles, i.e. particles that do not usually decay in the detector and are detected: charged particles and photons,

that both contribute to form also the final state of my signal channel in $\tau^- \to \pi^- \left(\pi^0\right) \nu_\tau$ decay. An outline of the essential aspects of the reconstruction of these, along with the associated performance quantities follows.

2.3.1 Charged-particle reconstruction

The ideal trajectories of charged particles in a solenoidal magnetic field are helical, with radius proportional to their transverse momentum. This ideal configuration is altered by effects such as Coulomb scattering. When reconstructing a track, that is, measuring its momentum and position of closest approach to the interaction point, we need to take into account for these possible effects.

Track reconstruction, or "tracking", in Belle II [44] consists in the combination of sequences of hits (measurement space-points) into tracks (full trajectories) after a charged particle crosses multiple active layers. The first step is called track finding; the second, track fitting. Tracking relies on PXD, SVD, and CDC information. Due to the different properties of these detectors, specific algorithms are used for each.

As a first step of track finding, hits in the outer tracking volume (CDC), where lower occupancy aids track finding, are filtered and reconstructed by two independent algorithms. One is a global track finding based on the Legendre algorithm [53], which transforms the position of each hit into a (θ, ρ) pair that represents all the circles traversing both the IP and the considered hit. Another is a local algorithm that takes into account possible non-circular trajectories. The global track finding searches for patterns of hits consistent with helical trajectories, accounting for layer inefficiencies, while local track finding detects extended patterns of nearby hits, to complement the global search and detect short tracks and tracks displaced from the IP. The results of both algorithms are merged and the resulting CDC-only tracks are fitted by an iterative fitter based on a Kalman filter, which accounts also for possible random perturbations on the trajectory due for example to multiple scattering or energy losses [54].

Then, tracks are extrapolated inward making sure to avoid duplications, and SVD information is added. They are fitted again, before being extrapolated further inward to the PXD to define regions of interest around their expected intersection points. If an excited pixel is found inside this region, it is included in the pattern recognition algorithm, otherwise it is discarded.

Finally, the parameters of the track are determined in a fitting algorithm and by assuming a mass hypothesis (figure 2.13) and formated into:

- d_0, the distance of the point of the closest approach to the z axis;

- ϕ_0, the angle between the transverse momentum and the x axis at the point of the closest approach;

- ω, the track curvature signed according to the particle charge;

- z_0, the z coordinate at d_0;

- $\tan \lambda$, the tangent of the angle between track momentum and transverse momentum.

Track reconstruction is subjected to uncertainties and errors. A track might sometimes be a false track, if it includes hits from beam-induced background or combines hits from two different particles, or a clone track, if other tracks are reconstructed from the same particle.
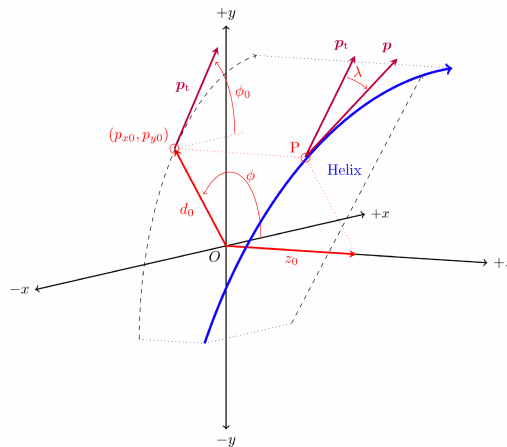
Figure 2.13: Three-dimensional representation of the helical trajectory of an ideal track at the point of closest approach (P) to the IP (the origin O). Symbol p is the momentum of the charged particle at the point P, p_t its transverse component and λ is the angle between the two vectors [55].

Tracking efficiency, that is the efficiency in reconstructing the track of a particle produced after a collision in the detector acceptance, varies from 75% at low transverse momenta ($\mathcal{O}(10)$ MeV/c) to 95% around 4 GeV/c. It degrades the closer the track is to the beam axis (small or large polar angles), while it is mostly constant around 90% regardless of the azimuthal angle.

The observed transverse momentum resolution is $\sigma(p_T)/p_T = 0.0011 p_T [\text{GeV}/c] \oplus 0.0025/\beta$ as shown in figure 2.14. The momentum- and angle-dependent impact parameter resolutions are $\sigma_{xy} = 10 \oplus 25/(p\beta\sin^{3/2}\theta)\mu$m and $\sigma_z = 15 \oplus 27/(p\beta\sin^{5/2}\theta)\mu$m for the transverse and longitudinal projections, respectively.
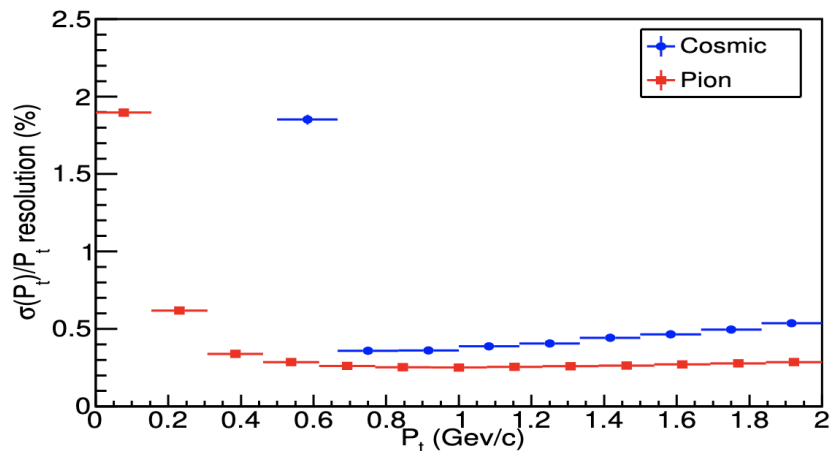
Figure 2.14: Transverse momentum resolution for collision and cosmic ray Belle II data [8].

2.3.2   Charged-particle identification

Particle identification is essential in flavor physics as most of the interesting channels are suppressed and therefore affected by signal-like backgrounds that only differ by the

identity of some final-state hadrons. Particle identification (PID) at Belle II is achieved by combining information from several subdetectors. The trajectories of charged particles reconstructed by the tracking detectors, PXD, SVD, and CDC, are extrapolated outward to the TOP, ARICH, ECL and KLM detectors, where geometric matching between the tracks and observed signals is attempted. Offline reconstruction associates PID-detector information sensitive to its identity to each matching track. For example, the drift chamber output encodes information on the specific ionization energy loss associated with each track. The raw information is further processed to provide higher-level quantities that are more convenient for usage in analysis. These are typically 'likelihood' values associated to the track. For each of six possible mass hypotheses, kaon, pion, electron, muon, proton and deuteron, the likelihood expresses the probability to observe the reconstructed PID information if the mass hypothesis was true.

For each detector and particle-hypothesis, the likelihood is usually obtained by comparing the expected and the observed value of the raw information, taking into account the uncertainties. For instance, in the CDC such information is $dE/dx_{\text{obs}}(h)$, the specific-ionization energy-loss observed for a charged particle h, averaged across the CDC wires. The resulting (natural logarithm of) the likelihood is

$$\ln \mathcal{L}_{\text{hyp}}^{\text{CDC}}(h) = -\frac{1}{2} \left[\frac{\frac{dE}{dx}_{\text{obs}}(h) - \frac{dE}{dx}_{\text{exp-hyp}}(h)}{\sigma_{\text{obs}}(h)} \right]^2 , \qquad (2.1)$$

where 'hyp' represents the particle hypothesis and $\sigma_{\text{obs}}(h)$ is the observed uncertainty on $dE/dx_{\text{obs}}(h)$, which mainly depends on the number of CDC hits associated to h. The expected value $dE/dx_{\text{exp-hyp}}(h)$ is the average ionization-energy loss from a charged particle h that has the observed momentum, assuming the hypothesis 'hyp', calculated using the Bethe-Bloch equation [56,57] modified according to minor empirical adjustments to adapt to the details of the CDC response. Figure 2.15 shows the $dE/dx_{\text{obs}}(h)$ distribution for various particle species in Belle II data and the expected energy loss for each of the six mass hypotheses considered.

In the TOP, the likelihood is calculated by comparing the observed number of detected photons associated to the charged particle with the photon yield expected from simulation [58,59],

$$\ln \mathcal{L}_{\text{hyp}}^{\text{TOP}}(h) = \Sigma_{i=1}^{N} \ln \left[\frac{S_{\text{hyp}}(x_i, t_i, h) + B(x_i, t_i)}{N_e(h)} \right] + \ln P_N(N_e(h)), \qquad (2.2)$$

where x_i and t_i are, respectively, the positions and times of arrival of the N Cherenkov photons excited by the charged hadron h. The term $S_{\text{hyp}}(x, t, h)$ is the signal distribution for the hypothesis 'hyp'; $B(x, t)$ is the distribution of background; and $N_e(h) = N_{\text{hyp}}(h) + N_B$ is the expected number of detected photons, which is the sum of the expected number of signal photons $N_{\text{hyp}}(h)$ for hypothesis 'hyp' and background photons N_B. The second term in Eq. (2.2) is a probability for a Poisson with mean N_e to generate N photons [58]. Figure 2.16 shows an example of the identification of a kaon in the TOP detector: the positions and arrival times of Cherenkov photons are compared with the values expected for a pion or a kaon.

Using the likelihoods for the various mass hypotheses, Belle II algorithms construct a particle identification variable $\text{PID}_{\text{hyp}}^{\text{det}}$ for every detector, which is directly used in physics analyses. As an example,

$$\text{PID}_{\pi}^{\text{det}}(h) = \frac{\mathcal{L}_{\pi}^{\text{det}}(h)}{\mathcal{L}_{\pi}^{\text{det}}(h) + \mathcal{L}_{K}^{\text{det}}(h) + \mathcal{L}_{e}^{\text{det}}(h) + \mathcal{L}_{\mu}(h) + \mathcal{L}_{p}^{\text{det}}(h) + \mathcal{L}_{d}^{\text{det}}(h)}, \qquad (2.3)$$
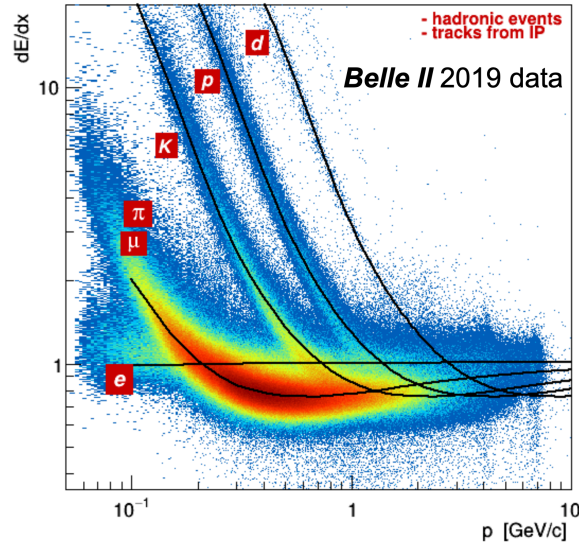
Figure 2.15: Distribution of (points) observed ionization-energy loss as a function of momentum for charged particles from hadronic events reconstructed in Belle II data, along with average expected values (solid lines). Reproduced from Ref. [46].
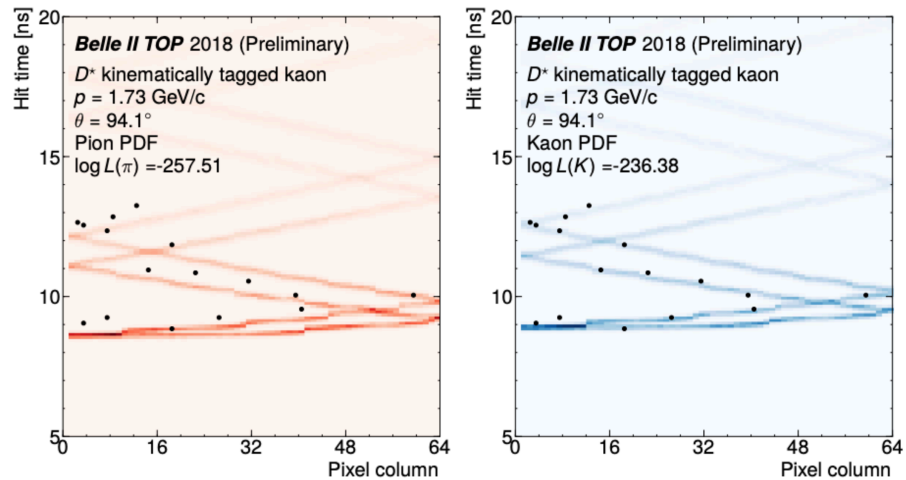
Figure 2.16: Example of kaon identification in the TOP detector. Arrival time of the Cherenkov photons as a function of position is compared with the expectations for (left) a pion and (right) a kaon passing in the TOP [46].

is the $\mathrm{PID}_{\mathrm{hyp}}^{\mathrm{det}}$ expression associated with the pion mass hypothesis[1] , but the $\mathrm{PID}_{\mathrm{hyp}}^{\mathrm{det}}$ values for other mass hypotheses are obtained by replacing the likelihood at the numerator $\mathcal{L}_\pi^{\mathrm{det}}(h)$ with the corresponding hypothesis-specific value $\mathcal{L}_{\mathrm{hyp}}^{\mathrm{det}}(h)$. The quantity $\mathrm{PID}_{\mathrm{hyp}}^{\mathrm{det}}(h)$ is defined similarly to a likelihood ratio $\mathcal{L}_0/\mathcal{L}_1$, which is the best-performing quantity to test two alternative simple statistical hypotheses [60]. The $\mathrm{PID}_{\mathrm{hyp}}^{\mathrm{det}}$ variable assumes values from 0.0 to 1.0. The larger the $\mathrm{PID}_{\mathrm{hyp}}^{\mathrm{det}}$, the higher the probability of observing the reconstructed particle-identification signatures assuming true the chosen mass hypothesis.

Information from individual detectors is combined to improve the identification performance. The detector-specific likelihoods are combined together as a product,

$$\mathcal{L}_{\mathrm{hyp}}(h) = \mathcal{L}_{\mathrm{hyp}}^{\mathrm{TOP}}(h)\mathcal{L}_{\mathrm{hyp}}^{\mathrm{CDC}}(h)\mathcal{L}_{\mathrm{hyp}}^{\mathrm{SVD}}(h)\mathcal{L}_{\mathrm{hyp}}^{\mathrm{ARICH}}(h)\mathcal{L}_{\mathrm{hyp}}^{\mathrm{ECL}}(h)\mathcal{L}_{\mathrm{hyp}}^{\mathrm{KLM}}(h), \tag{2.5}$$

and the result is used in Eq.(2.6) to obtain the detector-combined PID. If a particle does not get reconstructed in a detector because, for instance, it escapes its acceptance, no PID information from that detector is available and the corresponding individual likelihood is set to unity.

Of the two main PID detectors, TOP allows separating pions from kaons at $0.4 - 4\,\mathrm{GeV}/c$ momenta with kaon identification efficiency of 85% and pion misidentification rate of about 10%, while ARICH separates pions from kaons across all their momentum and discriminates also pions, electrons, and muons below 1 GeV/c with 4σ separation or more.

Combining information from all detectors, the electron and muon identification efficiencies are respectively 86% and 88.5% after requiring the binary PID to be larger than 0.9, with pion misidentification rates of 0.4% and 7.3%, respectively. Binary PID is an additional PID variable that compares only two mass hypotheses, for example

$$\mathrm{PID}_{\mu,\pi}^{\mathrm{det}}(h) = \frac{\mathcal{L}_\mu^{\mathrm{det}}(h)}{\mathcal{L}_\mu^{\mathrm{det}}(h) + \mathcal{L}_\pi^{\mathrm{det}}(h)}. \tag{2.6}$$

Data and simulation agree, except at low momenta where discrepancies within 20% are observed. Performance of kaon identification for a threshold of 0.8 on the kaon-pion binary PID is summarized in figure 2.17. Efficiency varies from 95% to around 60%, depending on kaon momentum and polar angle. The pion misidentification varies from about 20% to less than 5%.

---

[1]In practice, the Belle II software expresses $\mathrm{PID}_{\mathrm{hyp}}$ using only the natural logarithm of the likelihood values,

$$\mathrm{PID}_{\mathrm{hyp}} = \frac{e^{\ln\mathcal{L}_{\mathrm{hyp}} - \ln\mathcal{L}_{\mathrm{MAX}}}}{\Sigma_i\left(e^{\ln\mathcal{L}_i - \ln\mathcal{L}_{\mathrm{MAX}}}\right)} = \frac{e^{\Delta\ln\mathcal{L}_{\mathrm{hyp}}}}{\Sigma_i\left(e^{\Delta\ln\mathcal{L}_i}\right)} \tag{2.4}$$

where $\mathcal{L}_{\mathrm{MAX}}$ is the largest of the likelihood values over the six hypotheses.
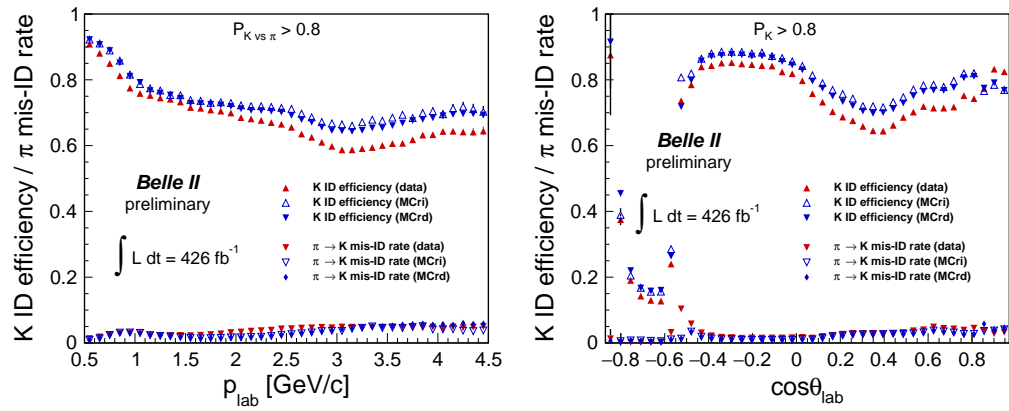
Figure 2.17: Kaon identification efficiencies and pion misidentification rates for events having a binary PID larger than 0.8, in data and simulation as functions of (left) kaon momentum, and (right) cosine of the polar angle in the laboratory frame [47].

2.3.3   Photon reconstruction

Given the relevance photon reconstruction has in this thesis, we outline its main aspects in more detail here.

Photons are reconstructed from energy deposits in the ECL not associated with any outward CDC track extrapolation. When photons impinge on the ECL, they undergo electromagnetic interactions with the crystals thus depositing energy, which is commonly spread across multiple crystals and might overlap with energy deposits from other nearby photons. In each collision that passes the trigger, the information of all 8736 crystals in the calorimeter is recorded for offline analysis. Raw crystal-level information is translated into photon candidates used in Belle II analyses through the photon reconstruction algorithms.

Sets of calorimeter crystals showing energy deposits are called clusters, and the process by which the energies and times observed in each of the crystals are converted into a set of clusters is called cluster reconstruction. The cluster reconstruction algorithm, illustrated in figure 2.18, starts by dividing the calorimeter active surface into connected regions, which are contiguous sets of crystals containing significant energy, isolated from all other connected regions. A connected region is assembled starting from a seed crystal, whose energy must exceed $10\,\mathrm{MeV}$. The eight immediate neighbors to the seed crystal are examined and included in the connected region if their energy exceeds $0.5\,\mathrm{MeV}$. If any of these have energy greater than $10\,\mathrm{MeV}$, their neighbors are also examined, and the process repeats. To form an idea of the chosen thresholds, the electronic noise is of order $0.35\,\mathrm{MeV}$, while energy deposits from beam background typically range from $0.5\,\mathrm{MeV}$ to $1\,\mathrm{MeV}$ in the barrel and forward endcap, and up to $2\,\mathrm{MeV}$ in the backward endcap.

Each connected region is then divided into clusters, one per local maximum. A local maximum is a crystal whose energy is greater than the seed energy and is greater than its eight immediate neighbours. If more than one local maximum is detected, the energy in each crystal is shared among the resulting clusters. For each local maximum i, each crystal j in the connected region is assigned an energy weight

$$w_j^i = E_{\mathrm{sum}}^i e^{-R_j^i/R_w} / \Sigma_k E_{\mathrm{sum}}^k e^{-R_j^k/R_w},$$

where R_j^i is the distance from the crystal j to the location of the centroid of the cluster associated with the local maximum i, R_w is $1.43\,\mathrm{cm}$ (40% of the Molière radius), and $E_{\mathrm{sum}}^i = \Sigma_j w_j^i E_j$ is the total energy of cluster i deposited in the crystals, where E_j is the total energy in crystal j. The weight w_j^i is the fraction of the energy in crystal j assigned to each cluster, and does not depend on the energy in the crystal, but rather on the energy of the clusters and the distance between the crystals and cluster centroid.

The properties of the cluster, including the centroid position, are derived from the corresponding set of associated crystals. The centroid is the weighted sum of the positions of the crystals, where the weight $w_j'^i$ for cluster i from crystal j is

$$w_j'^i = 4 + \log(w_j^i E_j / E_{\mathrm{sum}}^i).$$

Only crystals with positive weights (corresponding to crystals containing at least 1.8% of E_{sum}^i) are included in the sum. This is an iterative procedure. The centroid position is initially taken to be the center of the crystal exhibiting a local maximum, and cluster energy to be 50% more than the energy in the crystal showing the local maximum. The position and energy are updated after each iteration, and the process repeats until the centroid positions are stable. The process is similar for connected regions with only one local maximum, but in this case, the energy weights are all unity.
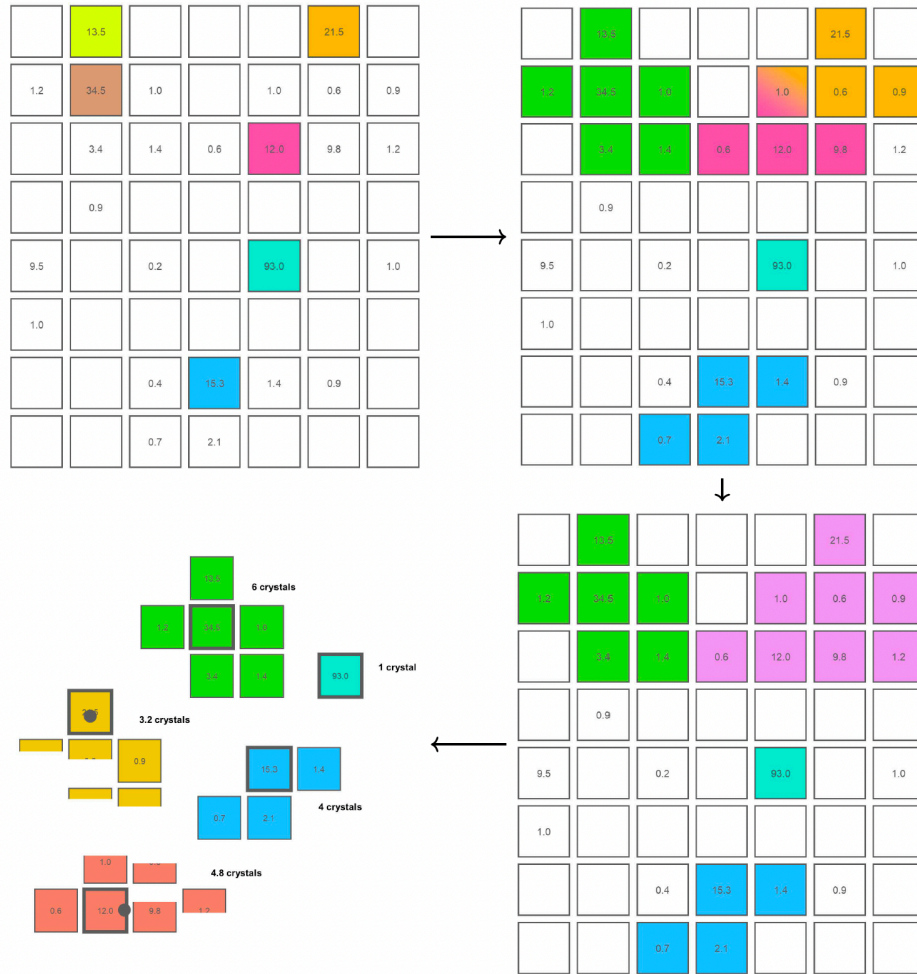
Figure 2.18: Scheme of the steps of cluster reconstruction. Seed crystals are identified (top left), neighbouring crystals are attached if they have a large enough energy (top right), connected regions are created (bottom right), and finally if a connected region has more than one local maxima, it is split in more clusters (bottom left) [47].

Cluster shape quantities are calculated using all crystals in the cluster. The energy is the sum of energies in the N most energetic crystals, where N depends on the location in the detector, the photon energy, and the level of beam-induced backgrounds in the event, estimated using out-of-time events, that are events with times far from the trigger time.

Finally, clusters associated with a CDC track, or with energy less than 50 MeV, or having times further away from the trigger time than (nominally) 99% of real photons of that energy, are discarded.

The energy of the surviving clusters is calibrated using simulated single photon events due to various effects that can modify their true energy: energy leakage out of the back of the calorimeter, energy deposited in inactive material between crystals or in front of the calorimeter, or energy deposited in crystals not included in the cluster energy calculation.

Finally, we associate to the cluster a reconstructed photon (or neutral hadron) candidate.

2.3.3.1 Photon matching

A particle reconstructed in simulation is considered "correctly reconstructed" if it is "matched" with the underlying generator-level particle. In the case of a photon, a cluster is correctly matched if a certain fraction of its reconstructed energy is attributable to the generated particle.

Each cluster can have weighted relations with up to 21 crystals. Each excited crystal, in turn, can have a weighted relation with none, one, or multiple generated particles. The weight between a cluster and a generated particle is given by the product of the weight between the corresponding cluster and crystal and the weight between the crystal and the generated particle. The weight between the cluster and the crystal, as described above, is just the fraction of energy the crystal contributes to the cluster. The weight between the crystal and the generated particle is calculated using the total energy deposited by the generated particle in each crystal. If multiple relations exist between a given cluster and generated particle, only the relation with the largest weight is used for photon matching. Truth matching is set between the reconstructed cluster and the generated particle if the following conditions are met:

- the generated particle is actually a photon,

- weight$/E_{\text{rec}} > 0.2\,\text{GeV}$, and

- weight$/E_{\text{true}} > 0.3\,\text{GeV}$,

where E_{rec} is the reconstructed energy and E_{true} is the true energy in simulation. If the generated particle is not a photon no match occurs. This applies even if one of the other lower-weighted relations for the particle is correct.

2.3.3.2 Shower topologies

Once clusters are reconstructed, the distribution of the detected energy within the crystals in each provides information about the spatial distribution of the released energy, so-called "shower-shape". This in turn offers information useful to statistically identify the various phenomena that generated the interaction.

The simplest shower shape originates from a single photon where the maximal energy is deposited in the center crystal of a shower symmetric around the crystal main axis. The whole shower is typically contained in an array of about 5×5 crystals, even for high photon energies. Example shower shapes are shown in figure 2.19 for simulated events.

While electron–induced clusters are intrinsically similar to photon clusters, their shower shape is often different due to additional bremsstrahlung photons emitted in the interaction with material surrounded by the ECL. These photons lead to less well-defined cluster shapes for electrons when compared to photons. In addition, electrons are bent in the magnetic field, which may result in a different entry angle into the ECL and a deviation of the shower from the radially symmetric shape even in the absence of additional radiation. Final state radiation photons collinear with the electron resulting from the collision can overlap or merge with the electron shower. Example shower shapes with and without radiated photons are shown in figure 2.20 for simulated events.

Highly–energetic π^0 mesons yield two photon showers that may overlap or merge. To recover these single showers as π^0 mesons requires a dedicated reconstruction. Example shower shapes with overlapping and merged photons are shown in figure 2.21 for simulated events. Overlapping photon showers share crystals but have separate seeds, whereas merged
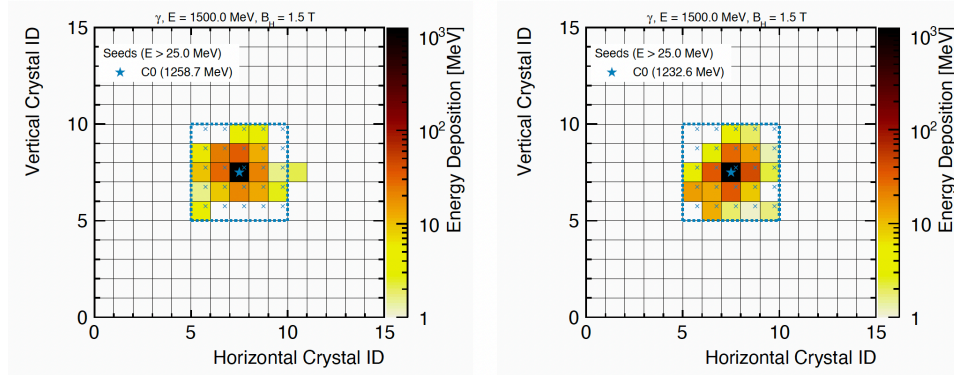
Figure 2.19: Simplified event displays of the energy deposition of two simulated photons with $E = 1.5\,\text{GeV}$. In addition to the seed crystal, a 5×5 area around the seed is marked [47].
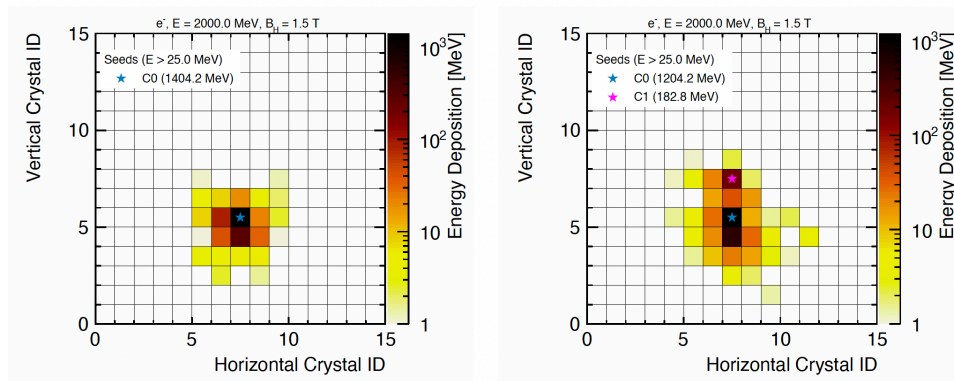
Figure 2.20: Simplified event displays of the energy deposition of (left) one simulated electron with $E = 2.0\,\text{GeV}$ and (right) one simulated electron with $E = 2.0\,\text{GeV}$ and an additional radiated photon [47].

showers have only one seed. In this analysis, I did not include the fraction of overlapping and merged photons in the reconstruction.
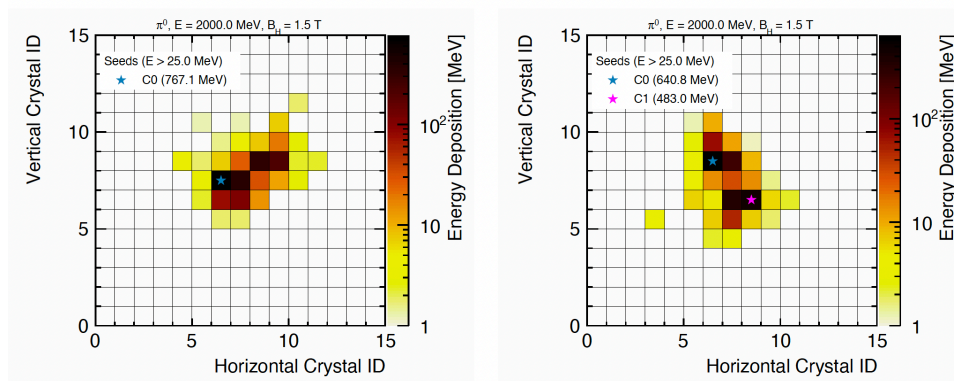
Figure 2.21: Simplified event displays of the energy deposition of (left) one simulated merged π^0 with $E = 2.0\,\text{GeV}$ and (right) one simulated π^0 with $E = 2.0\,\text{GeV}$ with overlapping photon showers [47].

A fraction of neutral hadrons, such as neutrons and K_L^0, undergo strong interactions in the ECL: the resulting shower shape is irregular and radial asymmetric. Example shower shapes are shown in figure 2.22 for simulated events. If charged hadrons interact strongly
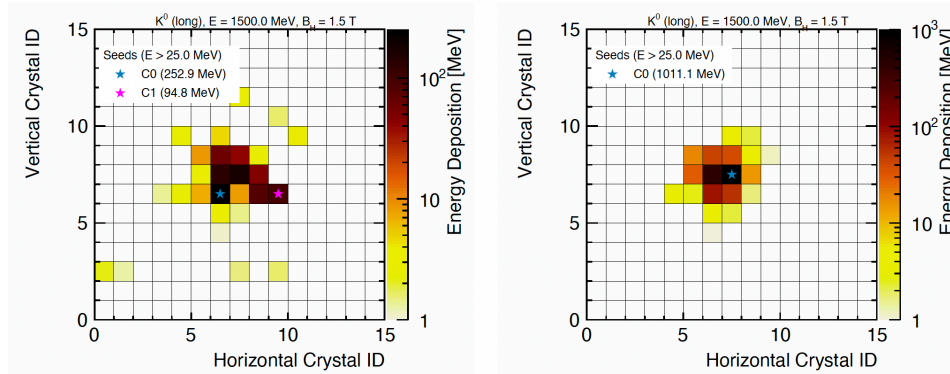
Figure 2.22: Simplified event displays of the energy deposition of (left) one simulated K_L^0 with $E = 1.5\,\mathrm{GeV}$ with two seeds and (right) one simulated K_L^0 with $E = 1.5\,\mathrm{GeV}$ [47].

within the ECL, they produce irregularly shaped showers in addition to a tilted entry angle due to the magnetic field. If they do not interact strongly, they still leave a small, mimimum-ionizing-like signal similar to that of as muons. An example of shower shape is shown in figure 2.23 (left) for a simulated event. Additional radiated photons may lead to rather complicated topologies of overlapping hadron and electromagnetic showers.
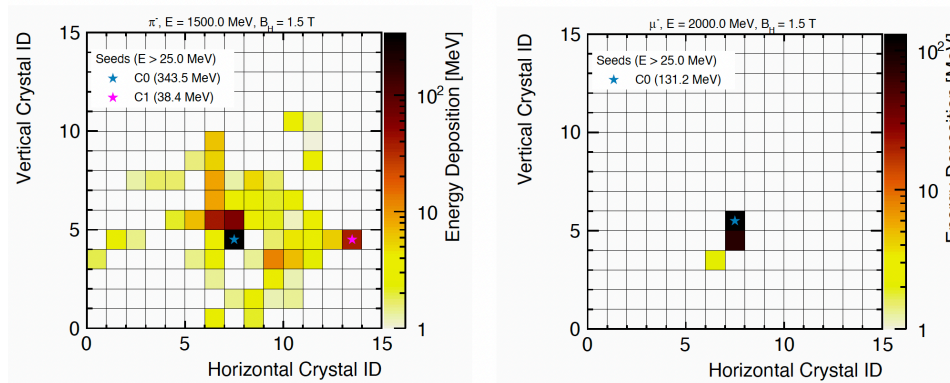
Figure 2.23: Simplified event displays of the energy deposition of (left) a simulated charged pion with $E = 1.5\,\mathrm{GeV}$ and (right) a simulated muon with $E = 2.0\,\mathrm{GeV}$ [47].

Particles like muons and hadrons that do not interact strongly within the crystal are minimum-ionizing, depositing around $200\,\mathrm{MeV}$ almost solely in the crystals directly transversed by the particle. An example shower shape is shown in figure 2.23 (right) for a simulated event. Additional radiated photons may lead to an overlapping minimal ionizing signal with electromagnetic showers.

2.3.3.3 Neutral particle reconstruction performance

The energy resolution for photons ranges from $\sigma_E/E = 7.7\%$ at 100 MeV to 2.2% at 1 GeV. The resolution on the reconstructed π^0 mass is $5.4\,\mathrm{MeV}/c^2$.

Chapter 3

A novel approach for the determination of the π^0 reconstruction efficiency

This chapter states the motivations for an accurate π^0 reconstruction efficiency, outlines the methods used so far at Belle II, and introduces my proposal for a novel approach.

3.1 Motivation

Inspection of the systematic uncertainties in absolute rates measurements involving final-state π^0 mesons at Belle II shows that the π^0 reconstruction efficiency is among the dominant contributions (see table 3.1). The table lists the systematic uncertainties considered in the measurement of the branching fraction and CP asymmetry of $B^0 \rightarrow \pi^0 \pi^0$ decays from an analysis of 198×10^6 $B\bar{B}$ mesons pairs collected by the Belle II experiment. The total systematic uncertainty is 16% and about 12% is due to the uncertainty on the π^0 reconstruction efficiency. An additional relevant case is the $B^0 \rightarrow J/\psi \, \pi^0$ decay, in which the overall systematic uncertainty is 3.7%, 16% of which is represented by the uncertainty on the π^0 reconstruction efficiency [26]. These are just two examples, out of several, that show how a better understanding of the π^0 reconstruction efficiency is important to enable more precise constraints on important physics parameters.

3.2 Challenges

The efficiency of reconstructing a particle, such as the neutral pion in this case, is tipically defined as the probability for detecting, reconstructing, and correctly identifying such a particle when produced in a collision. The efficiency accounts for the geometrical acceptance of the detector, the probability for the particle to reach the active region of the detector without interacting earlier, the probability for that particle to interact in the active region, the probability that the interaction generates a signal above electronic noise, et cetera, and the efficiency of the selection requirements used to discriminate background processes. To measure the efficiency, an unbiased sample of neutral pions is typically used. One option is to use a full, realistic simulation: knowing the number of generated particles, one can count the number of surviving particles after simulating the full chain of detection, reconstruction, and selection. However, simulation would likely fail in reproducing the true value of the reconstruction efficiency accurately due to approximations and simplifications

Source	$\mathcal{B}(\%)$	$\mathcal{A}_{CP}$
π^0 reconstruction efficiency	11.6	n/a
Continuum parametrization	7.4	0.02
Continuum classifier efficiency	6.5	n/a
$1 + f^{+-}/f^{00}$	2.5	n/a
Fixed $B\bar{B}$ background yield	2.3	0.01
Fixed signal r bin fractions	2.2	0.01
Knowledge of the photon-energy scale	2.0	n/a
Assumption of independence of ΔE from r	1.8	< 0.01
Number of $B\bar{B}$ meson pairs	1.5	< 0.01
Choice of $(M_{\mathrm{bc}}, \Delta E)$ signal model	1.3	0.02
Fixed continuum r bin fraction	1.1	< 0.01
Branching fraction fit bias	1.0	n/a
Best candidate selection	0.2	< 0.01
Mistagging parameters	n/a	0.05
Potential non-zero $B\bar{B}$ background $\mathcal{A}_{CP}$	n/a	0.03
$\mathcal{A}_{CP}$ fit bias	n/a	0.02
Continuum $q \cdot r$ asymmetry	n/a	0.01
Total	16.2	0.07

Table 3.1: Summary of systematic uncertainties for the measurement of the branching fraction and CP asymmetry of $B^0 \to \pi^0 \pi^0$ decay using 198×10^6 $B\bar{B}$ pairs reconstructed in Belle II data. The total uncertainty is calculated by adding all systematic uncertainties in quadrature. Reproduced from ref. [28].

used to model the detection processes involved. In the case of $\pi^0 \to \gamma\gamma$ reconstruction, we might have differences between data and simulation especially due to multiple different factors:

- **Imperfect modeling of the material distribution in the detector**. A photon can undergo pair production in the material of the detector before reaching the calorimeter. If the resulting electron and positron are reconstructed in the tracking detectors, the corresponding clusters in the calorimeter, if any, are identified as being produced by a charged particle and the photon candidate is not reconstructed as such. Even if the reconstruction algorithms still finds a photon candidate, the energy resolution might be degraded, leading to a π^0 candidate with an incorrectly reconstructed mass, which gets discarded. Because the description of the material within the detector, or the description of the interactions of the materials and photons may not be completely accurate, discrepancies between the data and the simulation could occur, affecting the efficiency;

- **Imperfect modeling of photon-shower shape**. In order to discriminate electromagnetic from hadronic showers, shower shape variables, such as the number of crystals associated with a shower are used. Showers shapes are difficult to simulate as they require a detailed description of the particle interactions in the crystals. Approximations used in modeling often generate efficiency differences between data and simulation;

- **Split-offs**. The particle showers created by hadrons interacting with the material in

the calorimeter contain a fraction of neutral hadrons. Such secondary hadrons can travel a sizable distance in the calorimeter before interacting with the material and depositing (a part of) their energy. These so-called split-offs leave the signature of a calorimeter cluster without an associated track pointing to it, which resemble closely a genuine photon. As for the photon-shower shape, a detailed modeling of hadronic showers is difficult: split-offs present a further potential source of difference between data and simulation;

- **Unmodeled backgrounds**. Real data events typically contain more (low-momentum) photon candidates than simulation, most of which originate from beam-related background. This background consists primarily of electrons and positrons from radiative Bhabha scattering that hit elements of the detector or the beam pipe, producing neutrons with energies in the MeV range, which then can produce low energy showers in the calorimeter. These additional photon candidates increase the number of photon combinations in data, giving rise to more π^0 candidates, especially at low momentum. Differencies in photon multiplicity between data and simulation are likely to introduce discrepancies in the efficiencies.

The above effects, and possibly others, imply that determining the efficiency using only simulation is likely to be unreliable and would require relying on unsupported assumptions. A more robust approach is to use control data to correct the findings of simulation.

3.3 Current Belle II approaches

In Belle II, the π^0 reconstruction efficiency is typically obtained from the ratio of decay rates between channels that differ only by the presence of a π^0 at the numerator, normalized by the branching fractions of the relevant processes. If the initial state is the same for denominator and numerator processes, and all final state particles at the denominator are also final states of the numerator, the ratio of event rates after accounting for the respective branching fractions, isolates the π^0 reconstruction efficiency as the only remaining factor.

Figure 3.2 offers an overview of the methods currently used in Belle II. The main limitations of many of these approaches are the irreducible systematic uncertainties due to limited knowledge of the branching fractions of the decays used, and the restrictions in π^0 momentum that limit the applicability of the resulting efficiency.

An example is the ratio of $D^0 \to K^- \pi^+ \pi^0$ over $D^0 \to K^- \pi^+$. The equation defining the π^0 reconstruction efficiency is

$$\varepsilon_{\pi^0} = \frac{N(D^0 \to K^- \pi^+ \pi^0)}{N(D^0 \to K^- \pi^+)} \frac{\mathcal{B}(D^0 \to K^- \pi^+)}{\mathcal{B}(D^0 \to K^- \pi^+ \pi^0)\mathcal{B}(\pi^0 \to \gamma\gamma)},$$

where $N(D^0 \to K^- \pi^+ \pi^0)$ and $N(D^0 \to K^- \pi^+)$ are the observed signal yields of $D^0 \to K^- \pi^+ \pi^0$ and $D^0 \to K^- \pi^+$ decays, respectively.

Hence,

$$\frac{\varepsilon_{\pi^0}}{\varepsilon_{\pi^0}^{\mathrm{MC}}} = \frac{N(D^0 \to K^- \pi^+ \pi^0)/N^{\mathrm{MC}}(D^0 \to K^- \pi^+ \pi^0)}{N(D^0 \to K^- \pi^+)/N^{\mathrm{MC}}(D^0 \to K \pi)}.$$

Large samples of pure D mesons decays are available, so the statistical uncertainty on this measurement is small. Nevertheless, the method is limited by the 2.6% uncertainty on $\mathcal{B}(D^0 \to K^- \pi^+)/\mathcal{B}(D^0 \to K^- \pi^+ \pi^0)$ [12], and by possible discrepancies between data and simulation in the Dalitz distribution of $D^0 \to K^- \pi^+ \pi^0$ decays, which are hard to decouple from π^0-related effects. Unless more precise measurements of $\mathcal{B}(D^0 \to K^- \pi^+)$

and $\mathcal{B}(D^0 \to K^- \pi^+ \pi^0)$ become available, this method remains therefore limited by the irreducible systematic uncertainty from the branching fraction ratio, and will be not suitable for future Belle II analyses.

As shown in table 3.2, a method that may circumvent the previous problems is the one yielding the absolute reconstruction efficiency from the process $e^+ e^- \to \gamma_{\mathrm{ISR}} \, \omega(\to \pi \, \pi \, \pi^0)$. Unlike other methods, where the π^0 reconstruction efficiency in data is determined relative to simulation, in this case one accesses the absolute π^0 efficiency through $e^+ e^-$ annihilation in three pions with an additional photon from initial state radiation. Here, we use partially and fully reconstructed events,

$$\varepsilon_{\pi^0} = \frac{N_{\pi^0}(\omega(\to \pi \, \pi \, \pi^0) \, \gamma_{\mathrm{ISR}})}{N_\omega(\omega(\to \pi \, \pi \, \pi^0) \, \gamma_{\mathrm{ISR}})},$$

where N_{π^0} is the number of events reconstructed after π^0 reconstruction and relevant selections, and N_ω is the number of events estimated using only the properties of the beam, the charged pions, and the ISR photon. By exploiting the kinematic constraints imposed by the conservation of the four-momentum and knowledge of the collision energy, it is possible to reconstruct the ω meson without using any information about the π^0. This method uses large samples, achieving an accuracy of less than 1% and a correction applicable to π^0 momenta of $0.2 - 4.5$ GeV/c. However, estimating efficiency with this method is nontrivial. The channels considered have large backgrounds, making it complex to model the shape of the background itself, which results in additional modeling systematic uncertainties. Indeed Belle II has not yet been able to finalize this method.

Another promising method is based on τ decays. Currently the collaboration compares the decay $\tau^- \to 3\pi^\pm \pi^0 \nu_\tau$ with $\tau^- \to 3\pi^\pm n\pi^0 \nu_\tau$ (n is π^0 multiplicity). This method probes a wide π^0 momentum range ($0.2 - 4.5$ GeV/c) and would achieve an accuracy of about 2%. The issue lies in the description of the kinematic properties of the decay $\tau^- \to 3\pi^\pm \pi^0 \nu_\tau$ which are not precisely known and are likely to differ between data and simulation, resulting in further hard-to-assess systematic uncertainties. Depending on how multibody kinematics is modeled in simulation, one can incur in apparent data-simulation differences in efficiency not arising from an erroneous π^0 reconstruction but arising from an incorrect description of the decay.

In summary, the accuracy in knowing the π^0 reconstruction efficiency is currently limited to about $3\% - 4\%$ in Belle II. Alternative methods to those used so far should be explored and developed in order to make optimal use of Belle II data.

3.4 A novel proposal

This thesis aims to measure the π^0 reconstruction efficiency using τ decays. Unlike the method based on multibody τ decays, this new approach uses the yield ratio between a three-body decay, $\tau^- \to \pi^- \pi^0 \nu_\tau$, and a two-body decay, $\tau^- \to \pi^- \nu_\tau$, in which kinematic modeling uncertainties are much reduced. In addition, the higher branching fractions of the channels considered (25.29% and 10.82% respectively) yield more abundant samples. These advantages are likely to allow for a more accurate estimation of the π^0 reconstruction efficiency.

On the other hand, since the multiplicity of particles in the final state is an important discriminating observable against low-multiplicity backgrounds such as Bhabha events, the presence of extra tracks, as in the multibody approach, is an advantage.

Also in this case the key idea is to use τ decays that differ only for one π^0 in the final state, such that the ratio of reconstructed signal yields in the same data set provides access

	$\varepsilon(\pi^0) =$	p(π^0) [GeV/c]	Expected π^0 systematic unc.	Resulting efficiency
D⁰ channels	$\dfrac{D^0 \to K\pi\pi^0}{D^0 \to K\pi} \cdot BR$	0.05 – 0.2 0.2 – 3.0	3.6% (~all from irreducible *BR* systematic)	Relative to MC
τ channels	$\dfrac{\tau \to 3\pi\pi^0}{\tau \to \pi X} \cdot BR$	0.2 – 4.5	1.8–2.4% (1.2% from irreducible *BR* systematic)	Relative to MC
ω ISR	$\dfrac{\gamma_{ISR}\omega \to (\pi\pi\pi^0)}{\gamma_{ISR}\pi\pi \text{ recoil}}$	0.2 – 4.5	Now: 1–4% Expected: <1%	Absolute
η channels	$\dfrac{\eta \to 3\pi^0}{\eta \to \gamma\gamma, \eta \to \pi\pi\pi^0}$	0.2 – 1.0	4% (0.7%—1.6% from irreducible *BR* systematic)	Relative to MC
S0 in D⁰ channels	Ratio of totally and partially reconstructed	0.2 – 1.5	n/a	Absolute
B⁰ → π·D⁽*⁾⁺	Ratio of totally and partially reconstructed	0.05 – 0.2	n/a	Absolute

Figure 3.2: Overview of the methods currently used for estimating π^0 reconstruction efficiency in Belle II and their features.

to π^0 reconstruction efficiency.

The signal yield of the numerator decay $\tau^- \to \pi^- \pi^0 \nu_\tau$ is

$$Y_n = \left[\sigma(e^+ e^- \to \tau^+ \tau^-) \int \mathcal{L}(t)\, dt\right] \cdot \left[\mathcal{B}(\tau^- \to \pi^- \pi^0 \nu_\tau)\mathcal{B}(\pi^0 \to \gamma\gamma)\right] \cdot \left[\varepsilon_{\pi^-}\varepsilon_{\pi^0}\right], \quad (3.1)$$

where σ is the cross section, $\int \mathcal{L}(t)\, dt$ is the integrated luminosity of the data set considered, $\mathcal{B}$ are the branching fractions of the decays, and ε are the reconstruction efficiencies of the single particles assuming that the joint efficiency factorizes into the product of single efficiencies.

The denominator decay $\tau^- \to \pi^- \nu_\tau$ features the same charged particles in the final state, and has yield

$$Y_d = \left[\sigma(e^+ e^- \to \tau^+ \tau^-) \int \mathcal{L}(t)\, dt\right] \cdot \left[\mathcal{B}(\tau^- \to \pi^- \nu_\tau)\right] \cdot \left[\varepsilon_{\pi^-}\right]. \quad (3.2)$$

Solving equations 3.1 and 3.2 for ε_{π^0}, we obtain

$$\varepsilon_{\pi^0} = \frac{Y_n \left(\tau^- \to \pi^- \pi^0 \nu_\tau\right)}{Y_d \left(\tau^- \to \pi^- \nu_\tau\right)} \left(\frac{\mathcal{B}(\tau^- \to \pi^- \nu_\tau)}{\mathcal{B}(\tau^- \to \pi^- \pi^0 \nu_\tau) \cdot \mathcal{B}(\pi^0 \to \gamma\gamma)}\right). \quad (3.3)$$

The only intrinsic limit of this method is related to the uncertainty associated with the τ lepton branching fractions [12],

$$\frac{\mathcal{B}(\tau^- \to \pi^- \nu_\tau)}{\mathcal{B}(\tau^- \to \pi^- \pi^0 \nu_\tau) \cdot \mathcal{B}(\pi^0 \to \gamma\gamma)} = 0.430 \pm 0.003 \quad (3.4)$$

which is 0.70%: this sets a bound to the minimum uncertainty achievable, which is a factor of about four better than current Belle II performance. In addition, as shown in figure 3.4, the processes cover a wide spectrum of π^0 momentum, from less than 0.2 GeV/c to 5 GeV/c, providing good overlaps with the typical momentum range of π^0 from B decays. After applying equation 3.3 to simulated and experimental data, the simulation correction factor $\varepsilon_{\pi^0}^{data}/\varepsilon_{\pi^0}^{MC}$ is derived. In this ratio, I assume that all differences between data and simulation are due to the π^0 reconstruction efficiency. Systematic uncertainties related to this assumption are discussed later in this thesis.

This method has not yet been developed in Belle II, but had been used in previous experiments. We expect the uncertainty of the results to be dominated by the systematic component as the involved processes have high rates. At SuperKEKB τ leptons are produced in the $e^+e^- \to \tau^+\tau^-$ processes with a cross section of 0.92 nb through the leading process whose Feynman diagram is shown in figure 3.3.
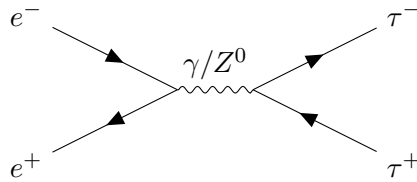
Figure 3.3: Leading Feynman diagram for $e^+e^- \to \tau^+\tau^-$ mediated by a photon or by a virtual Z^0 boson.

With a luminosity of about 4×10^{34} cm^{-2}s^{-1} as achieved recently, we would expect an event rate of $\tau^+\tau^-$ pairs of approximately 40 Hz. This, combined with the relevant branching fractions, provides abundant samples for reconstructing τ lepton decays.
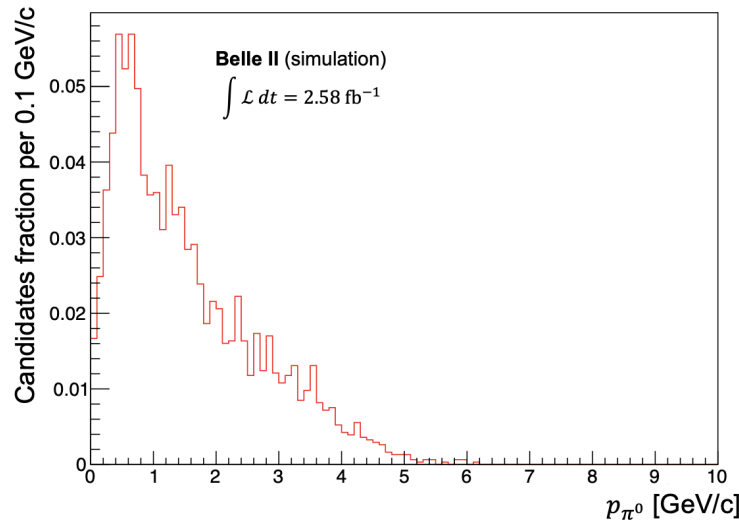
Figure 3.4: Distribution of π^0 momentum from simulated $\tau^- \to \pi^-\pi^0\nu_\tau$ decays in Belle II. Histogram is normalized to unit area. The integrated luminosity corresponds to $\int \mathcal{L}\,dt$ = 2.58 fb^{-1}.

3.5 Measurement strategy

The goal of this work is to measure the π^0 reconstruction efficiency using the approach
described in the previous section. Requirements for the proper application of this method
are

- The kinematic properties of the final-states particles shared between the numerator,
  $\tau^- \to \pi^- \pi^0 \nu_\tau$, and the denominator, $\tau^- \to \pi^- \nu_\tau$, should be as similar as possible,
  thus allowing for first-order cancellation of the common efficiencies for the charged
  pion in equation 3.3. Where these selections differ, reliable corrections must be
  applied to ensure the validity of the method;

- There should be no contamination between the numerator and denominator sam-
  ples, as this would compromise the independence of the two samples by introducing
  correlations that would not be easily accounted for in the efficiency;

- Because the denominator has a very minimal signature, based on a single track, it is
  very susceptible to contamination from background processes that mimic the signal
  decay. Hence, it is necessary to ensure the maximum purity of this sample.

To develop my efficiency estimation, I start with a simplified scenario that considers
only τ pair production events, and then extend the analysis to a more realistic simulated
scenario, to demonstrate its validity under realistic conditions.

In the analysis, to ensure consistency of selections, I adopt criteria that are as homoge-
neous as possible between the numerator and denominator, using simulation to correct for
any remaining discrepancies. In addition, to reduce the main background processes from
the outset, I choose to apply in reconstruction an exclusive requirement for leptonic decays
of the non-signal τ.

To avoid overlap between the samples, I define two disjoint samples by applying a
selection based on the number of photons in the signal side. Furthermore, to obtain a
highly pure sample of events $\tau^- \to \pi^- \nu_\tau$, I implement a targeted optimization. The
purity of the numerator is more straightforward, since the presence of the π^0 provides an
additional selection criterion through the diphoton mass.

I determine the signal yield for the $\tau^- \to \pi^- \nu_\tau$ channel through direct event counting
and I extract the signal yield for the $\tau^- \to \pi^- \pi^0 \nu_\tau$ decay channel performing a fit on the
π^0 invariant mass distribution.

Finally, using these yields, corrected for the respective branching fraction and selection
or reconstruction discrepancies, I estimate the π^0 reconstruction efficiency.

Chapter 4

τ-analysis generalities, samples and tools

This chapter describes τ-analysis generalities and the samples used. I provide a brief explanation of the processes that can mimic signal, followed by an overview of τ lepton decay topologies. I then discuss several observables that discriminate between τ pair production and other background processes used later in our analysis.

4.1 Signal processes

The production cross section of the main final states produced in e^+e^- collisions are summarized in figure 4.1. This is identical to figure 2.1 and I include it here for the reader's convenience.
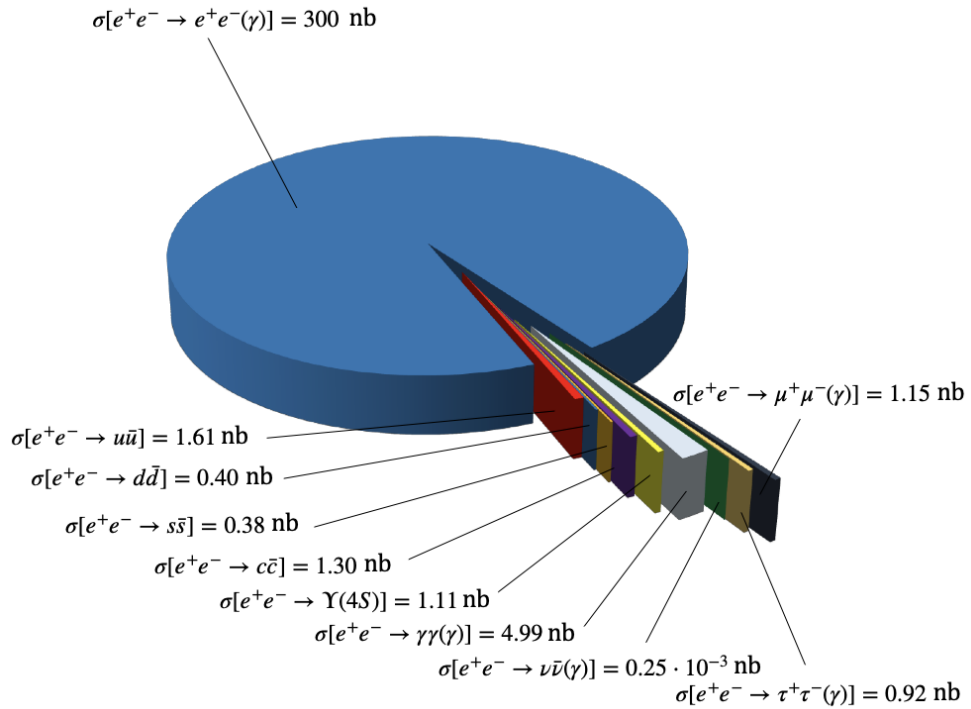
Figure 4.1: Pie chart of the cross sections for the main processes produced in e^+e^- collision at the $\Upsilon(4S)$ center-of-mass energy [8].

The τ pair production cross section, at 0.92 nb, is a small fraction of the total. These events are distributed over several decay channels (table 4.1). In the remainder of this thesis, by *numerator* I mean the data reconstructed to extract the $\tau^- \to \pi^- \pi^0 \nu_\tau$ yield (numerator in equation 3.3); by *denominator*, I mean the data reconstructed to extract the $\tau^- \to \pi^- \nu_\tau$ yield (denominator in equation 3.3). Both the numerator $\tau^- \to \pi^- \pi^0 \nu_\tau$ and denominator $\tau^- \to \pi^- \nu_\tau$ decays are *signals* of interest for this analysis.

Decay channel	Branching fraction $\mathcal{B}$
$\tau^- \to \pi^- \pi^0 \nu_\tau$	$(25.49 \pm 0.09)\%$
$\tau^- \to e^- \overline{\nu}_e \nu_\tau$	$(17.82 \pm 0.04)\%$
$\tau^- \to \mu^- \overline{\nu}_\mu \nu_\tau$	$(17.39 \pm 0.04)\%$
$\tau^- \to \pi^- \nu_\tau$	$(10.82 \pm 0.05)\%$
$\tau^- \to \pi^- 2\pi^0 \nu_\tau$	$(9.26 \pm 0.10)\%$
$\tau^- \to \pi^- 3\pi^0 \nu_\tau$	$(1.04 \pm 0.07)\%$
$\tau^- \to K^- \nu_\tau$	$(0.696 \pm 0.010)\%$
$\tau^- \to K^- \pi^0 \nu_\tau$	$(0.433 \pm 0.015)\%$
$\tau^- \to \pi^- 4\pi^0 \nu_\tau$	$(0.11 \pm 0.04)\%$

Table 4.1: τ decay channels considered in this analysis and their branching fraction [12].

4.2 Typical background processes

The measurement concept discussed in the previous chapter ideally assumes that only the signal is present in the analysis sample. However, in practice, as shown in table 4.1 and figure 4.1, the sample contains backgrounds. It is convenient to discuss in advance some generalities on the nature of these backgrounds, since they represent a primary challenge in this study and are a significant limitation for an accurate estimation of the π^0 meson reconstruction efficiency. This issue is particularly relevant for the denominator, which, being less distinctive, is the most vulnerable to contamination by background processes.

The principal distinguishing feature of $e^+e^- \to \tau^+\tau^-$ events is the low multiplicity in the number of particles produced in the final state. This allows to distinguish them from hadronic backgrounds like $e^+e^- \to q\overline{q}$, and $e^+e^- \to B\overline{B}$, which have competing production cross sections. These processes, which typically generate 5 to 10 charged particles in the final state, can be straightforwardly discriminated against τ pair-producing events by selections based on track multiplicity. However, several other background processes are also characterized by low multiplicity and can therefore contaminate our sample, emulating τ pair events. These processes can be classified into two specific categories.

The first category includes so-called low-multiplicity backgrounds. They consist mainly of Bhabha decays ($e^+e^- \to e^+e^-$), which, due to cross section 300 times larger (figure 4.1) and the presence of only two tracks in each event, represent the principal background. This category also includes muon-pair, four-electron, and two-muon and two-electron processes. For these events, multiplicity does not prove to be an effective suppression criterion. Therefore, it is necessary to use additional observables, discussed later, to discriminate them against signal.

The second category includes τ decays that are not relevant to our analysis (table 4.1) but could mimic the signal channels. Those expected to predominate are τ leptonic decays, i.e., $\tau^- \to \ell^- \nu_\tau \overline{\nu}_\ell$. These processes constitute about 34% of the total τ branching

fraction and yield a single track in the final state just as our denominator. Therefore, it is necessary to use other observables, discussed later, to improve discrimination between signal and these backgrounds.

4.3 τ decay topology
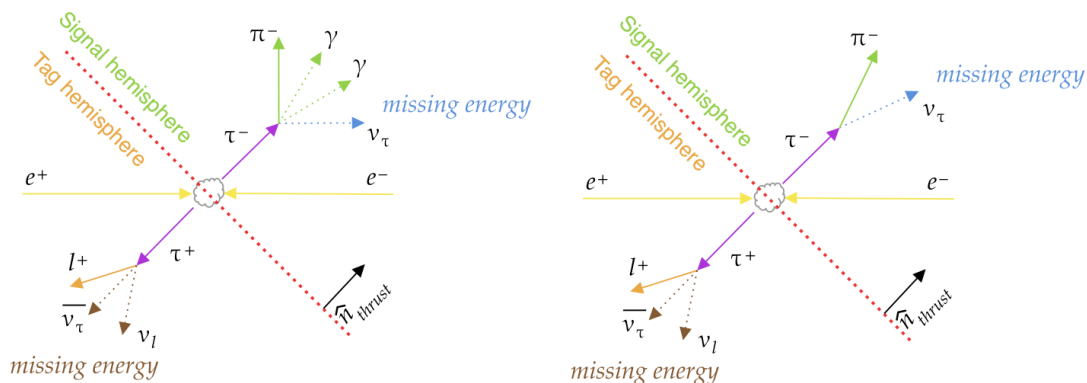
Figure 4.2: Illustration of the 1×1 topology in the center of mass system. Both the signal ("1-prong") $\tau^- \to \pi^- \pi^0 \nu_\tau$ (left) and $\tau^- \to \pi^- \nu_\tau$ (right) and leptonic tag side ("1-prong") are in opposite hemispheres.

In order to help the understanding of the subsequent description of the discriminating observables, I discuss some specific aspects related to τ-lepton analysis at Belle II. Here, I always refer to the center-of-mass reference frame (c.m.). Following the collision a pair of τ leptons are produced in an electromagnetic process mediated by a virtual photon or Z boson. In the c.m., the two leptons move away from each other in opposite directions each with energy equal to half the collision energy i.e., about 5 GeV. The τ leptons are charged particles with a mass 3500 times that of the electron i.e., about 1.8 GeV/c^2 and with an average lifetime of about 0.3 ps. After traveling a few tens of micrometers they decay into lighter products. Due to the largely inferior mass of the decay products than the τ mass, the decay products are highly collimated along the original τ flight direction.

The back-to-back production and the collimated character of decays allows the identification of two spatially separate regions in the c.m. called hemispheres. A hemisphere is defined as the portion of event space identified by a plane orthogonal to the τ direction of motion passing through the interaction point.

These two regions are called signal hemisphere and tag hemisphere. The signal hemisphere is defined as that containing the decay of interest, $\tau^- \to \pi^- \pi^0 \nu_\tau$ or $\tau^- \to \pi^- \nu_\tau$. The tag hemisphere corresponds to the rest of event, which contains the decay of the "other" τ lepton. Even if it does not contain signal particles, the tag hemisphere contains information that is usually convenient in an analysis as it allows us to impose kinematic constraints on the signal and reduce backgrounds. Depending on analysis needs in term of efficiency and purity, one can be inclusive by accepting any generic decay channel in the tag side or exclusive by admitting only a subset of decay channels.

In this analysis, to reduce the main background processes from the outset, I apply in reconstruction an exclusive requirement for leptonic decays of the τ tag. Although this choice results in a reduction in signal sample size, it is expected to contribute to background suppression.

4.4 Discriminant variables

In order to facilitate the understanding of the subsequent analysis steps, I briefly discuss below the main observables used in our, and other typical τ analyses at Belle II, which reduce the impact of the two categories of backgrounds described previously in section 4.2.

Thrust. Thrust is an important quantity that allows discrimination between $e^+e^+ \rightarrow \tau^+\tau^-$ and low-multiplicity background events and also $e^+e^- \rightarrow B\overline{B}$ events. It characterizes the shape of the event by measuring how collimated the event is along any preferred axis (the direction of flight of the signal τ in our case). For N momenta in an event $\mathbf{p}_i$ where $i = 1, ..., N$ (including those of neutral particles), thrust T is defined as

$$T = \frac{\sum_{i=1}^{N} |\hat{n} \cdot \mathbf{p}_i|}{\sum_{i=1}^{N} |\mathbf{p}_i|}, \tag{4.1}$$

where $\hat{n}$ is the unit vector, called thrust axis, that maximizes the total momentum projection [61]. By construction, thrust values range between 0.0 and 1.0, and the more collimated the event, the more the thrust will approach unity, indicating a more "jet-like" geometry of the event. This observable effectively distinguishes between $\tau^+\tau^-$ events and other processes, such as $B\overline{B}$ events, as well as low multiplicity events like $\mu^+\mu^-$ or e^+e^- production. In $B\overline{B}$ events the collision energy is distributed among a larger number of particles resulting in more spherical events. In contrast, μ or e pair production events, due to the lower lepton masses than the τ lepton, tend to result in higher momenta on average, making the event more jet-like than in τ production.

Sphericity. Sphericity is another variable, closely related to thrust and mathematically quantifying the spatial distribution of tracks within the detector volume. It is defined as

$$S = \frac{3}{2}\left(\lambda_2 + \lambda_3\right), \tag{4.2}$$

where λ_2 and λ_3 are the eigenvalues of the sphericity ellipsoid, ordered such that $\lambda_2 \geq \lambda_3$. The sphericity ellipsoid is constructed from the sphericity tensor

$$S_{ij} = \frac{\sum_k p_i^k p_j^k}{\sum_k |\vec{p}^k|^2}, \tag{4.3}$$

where p_i^k is the ith component of the momentum of the kth particle. The momentum components are summed over all particles in the event. The values of sphericity S range from 0.0 to 1.0. Values $S \approx 0.0$ mean that all particles are emitted along a single direction (jet-like events), while $S \approx 1.0$ indicates particles distributed isotropically (spherical events). For the same reasons discussed for thrust, sphericity discriminates between different types of events based on their spatial geometry.

Missing energy. Missing energy E_{miss} is another relevant quantity that allows discrimination between τ pairs and background events. It is defined as

$$E_{miss} = E_{tot} - E_{vis} \tag{4.4}$$

where E_{tot} denotes the total energy of the signal τ corresponding to half the energy of the collision and E_{vis} denotes the "visible" energy, corresponding to the sum of the observed energies of all reconstructed particles. All known τ decays have at least one neutrino in the final state due to the family-wise conservation of lepton number and Belle II does not directly detect neutrinos. Therefore, in τ decays, the maximum visible energy

is inferior to the energy of the τ emerging from the collision unlike in background events such as $e^+e^- \to q\bar{q}$ or $e^+e^- \to B\overline{B}$.

In addition, the missing energy is particularly discriminating against Bhabha and muon-pair-producing events. In τ pair production events, a missing energy component is present, whereas in Bhabha and muon pair production events, no significant energy loss is anticipated.

Charged-particle momentum. The momentum of the charged particle is determined by the curvature the track acquires within the magnetic field. Multibody decays such as those of τ leptons, distribute momentum across multiple particles, making momentum a sensible choice for discriminating against background processes, such as Bhabha events, which represent the main source of contamination in our sample.

Particle identification. Information associated with the identity of charged particles enhances discrimination against background, especially in candidates from misreconstructed τ decays. For example, it allows discriminating events in which the pion is misidentified as an electron or muon, thereby reducing the probability that a $\tau^- \to \mu^- \bar{\nu}_\mu \nu_\tau$ or $\tau^- \to e^- \bar{\nu}_e \nu_\tau$ decay is mistaken for a signal event of the denominator ($\tau^- \to \pi^- \nu_\tau$).

Energy/momentum ratio. E/p is the ratio of the energy of the cluster reconstructed in the calorimeter to the momentum of the corresponding charged particle measured in the tracker. A selection based on the E/p ratio is particularly discriminating between events where the charged particle is a pion or a muon and those where it is an electron. Electrons, upon impinging on the calorimeter, tend to deposit almost all their energy as an electromagnetic shower. This means that the E/p ratio for electrons is close to unity, since the energy measured in the calorimeter (E) approximately equals to the momentum of the corresponding charged particle (p). Muons, with a mass approximately 200 times greater than that of electrons, lose energy in the calorimeter primarily through ionization, leading to a much smaller fraction of energy loss compared to electrons. Consequently, the probability of electromagnetic shower formation is significantly reduced, resulting in an E/p ratio for muons that is considerably less than unity. Pions, which are hadrons of mass similar to that of muons, can interact both electromagnetically and via the strong interaction. Although pions can deposit some energy in the calorimeter, their E/p ratio is also generally less than unity, but can vary more compared to muons, depending on the specific interactions in the calorimeter.

Therefore, this variable does not provide a clear separation between pion or muon, but it does allow for discrimination between pion and electron events.

4.5 Samples

Most of this study is based on simulated data. However, I also look at experimental data for a preliminary assessment of data-simulation discrepancies.

4.5.1 Simulated data

I use simulated data to prototype, develop, refine, and validate my study.

Simulated samples are based on the Monte Carlo approach. Monte Carlo samples are produced using event generators, which are computer programs that use pseudorandom number generators to produce sets of four-vectors reproducing final states of e^+e^- collisions according to theoretical models of particle kinematic properties and interactions. Generated data are then subjected to detector simulation, where models of the detector geometry and material are interfaced with models of interactions of particles with matter

and signal formation to reproduce the expected values of the raw quantities observed in the detector. These are then subjected to processing and event reconstruction as if they were collision data. The resulting simulated data contain information about reconstructed particles and about the generated *true* particles. By matching these sets of information, we understand whether particles are reconstructed properly, or what are the most frequent misreconstruction occurrences, and what are principal backgrounds. This "truth-matching" procedure is useful to optimize selection requirements, calculate signal efficiency, classify sample components, and for many consistency checks.

Figure 4.3 shows a sketch of the generation sequence for a τ pair event in Belle II. The properties of virtual photons or Z boson, created in the electron-positron annihilation, and their subsequent splitting into a τ pair is simulated by `Pythia8` [62]. The decays of the τ pair are simulated by `TAUOLA` [63]. Photon emission by final-state charged particles known as final state radiation is simulated by `PHOTOS` [64].

For signal studies, I simulate exclusive samples of $e^+e^- \to \tau^+\tau^-$ events. Events are then fed to the standard Belle II detector simulation, based on the `GEANT4` package [65], which simulates interaction with matter and signal formation yielding simulated data in the same format as experimental data.

For τ pair background studies, I use centrally simulated $e^+e^- \to \tau^+\tau^-$ events based on `TAUOLA`, where τ lepton undergo all their allowed decays. The relative proportions among decay modes are based on known values or upper limits when available [12], and on arbitrary educated guesses otherwise.

For background and validation studies, I use centrally produced simulated samples corresponding to a subset of the on-resonance data available at the time of this writing. These include $e^+e^- \to \mu^+\mu^-$ and $e^+e^- \to e^+e^-$ (called *low-multiplicity backgrounds*), $e^+e^- \to q\bar{q}$, and $e^+e^- \to B\bar{B}$ events all generated using `KKMC` [66] interfaced with `Pythia8`, and `PHOTOS`.
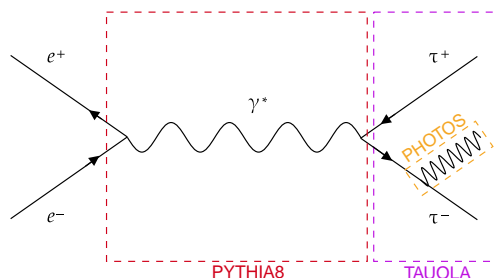
Figure 4.3: Sketch of the simulation sequence of a τ pair event in Belle II.

The simulation samples correspond to a realistic dataset that includes all components, with the observed level of beam background added, sampled run by run and plugged-in directly from the data. To quantify the background composition after the event reconstruction and selections, I generate generic and low multiplicity samples with the same beam background and data taking conditions as the signal samples. The samples are listed in table 4.2. The total integrated luminosity is 1.5 ab^{-1} (some samples require an appropriate rescaling). For my study, I use a sample corresponding to about 0.5% of the total simulated data available, i.e., equal to about 7.45 fb^{-1} to facilitate processing.

Process	$\int \mathcal{L}\, dt$ (fb^{-1})	Process	$\int \mathcal{L}\, dt$ (fb^{-1})
Generic		**Low multiplicity**	
$e^+e^- \to B^0\overline{B^0}$	7.45	$e^+e^- \to e^+e^-(\gamma)$	0.19
$e^+e^- \to B^+B^-$	7.45	$e^+e^- \to \mu^+\mu^-(\gamma)$	7.45
$e^+e^- \to \tau^+\tau^-$	7.45	$e^+e^- \to e^+e^-e^+e^-$	1.86
$e^+e^- \to u\overline{u}$	7.45	$e^+e^- \to e^+e^-\mu^+\mu^-$	1.86
$e^+e^- \to d\overline{d}$	7.45	$e^+e^- \to \ell^+\ell^-X^+X^-$	1.86
$e^+e^- \to s\overline{s}$	7.45	$e^+e^- \to h^+h^-ISR$	1.86
$e^+e^- \to c\overline{c}$	7.45	$e^+e^- \to \gamma\gamma$	3.72

Table 4.2: Process description and integrated luminosity of the simulated samples used in the analysis.

4.5.2 Experimental data

The Belle II experiment started physics data taking in March 2019, accumulating electron-positron collision data corresponding to an integrated luminosity of 531 fb^{-1}. In order to reconstruct the signal $\tau^- \to \pi^-\pi^0\nu_\tau$ and $\tau^- \to \pi^-\nu_\tau$ decays, for the preliminary assessment of data-simulation discrepancies described in section 7.2, I used only about 4.61 fb^{-1} corresponding to about 0.9% of the full data set collected up to July 2024. This reduction of sample size will be lifted when this work will be applied to Belle II data for the final determination of efficiency. The analysis does not use data collected at a collision energy higher than the $\Upsilon(4S)$ resonance.

4.5.3 Basic data structures

As many physics topics are studied in Belle II, data are analyzed multiple times by hundreds of collaborators. To ease the simultaneous analysis of such a large amount of data, various centralized data processing steps are implemented.

Raw data are processed centrally to produce summary data, which are reduced in size and focus on higher-level information related to primitives for physics analysis, including four-momenta, vertices, particle-identification information, and others. A second centralized step consists in applying loose selection criteria on summary data to obtain analysis-specific subsets (*skims*) further reduced in size so that each collaborator can access them and quickly process them. For τ physics at Belle II, there are three skims available: "thrust", "generic" and "LFV". However, due to the presence of selection criteria in each of these samples that would limit the extent of this π^0 efficiency study, which would compromise signal efficiency, we decide to use unskimmed samples for this analysis.

Chapter 5

Efficiency in a simulated $\tau^+\tau^-$ sample

In this chapter, I detail the initial determination of the π^0 reconstruction efficiency in the simplified case of τ pair production only. I outline the event reconstruction and the resulting sample composition. I discuss the optimization of the selection criteria and usage of the resulting sample to determine the numerator and denominator yields, including necessary corrections. Finally, I determine the efficiency in the simulated sample, demonstrating the method's feasibility within the context of this simplified scenario.

5.1 $\tau^+\tau^-$ event reconstruction

I am interested in τ pair production events that undergo leptonic decay in the tag side ($\tau^+ \to \mu^+ \, \nu_\mu \, \overline{\nu}_\tau$ or $\tau^+ \to e^+ \, \nu_e \, \overline{\nu}_\tau$) and $\tau^- \to \pi^- \, \pi^0 \, \nu_\tau$ or $\tau^- \to \pi^- \, \nu_\tau$ in the signal side.

Therefore, the events of interest for this analysis have a 1×1 topology for two total number of tracks.

The reconstruction requires exactly two tracks in the event, suppressing possible backgrounds from τ decays in the "3-prong" or "5-prong" modes. In order to reduce backgrounds from beam-beam interactions and ensure that tracks come from the interaction point (IP), all tracks are required to have radial distance $|dr| < 1$ cm from the IP and longitudinal distance $|dz| < 3$ cm.

On the tag side of the event, I explicitly require a leptonic decay to significantly reduce the most obvious background contributions. I apply a selection μID > 0.5 or eID > 0.5 on the particle identification of the tag track. To keep the reconstruction as general as possible, I do not apply any selection on the particle identification information of the signal track.

I do not impose explicit reconstruction of the π^0 meson in the numerator sample nor I apply any selection on photons. For photons, the reconstruction simply saves the kinematic, event, and Monte Carlo truth variables. Up to this point, the numerator reconstruction is equivalent to the denominator reconstruction.

I separate between numerator and denominator samples by selecting on the number of photons in the signal hemisphere. For the numerator, I select events with two photons in the signal side, while for the denominator, I exclude events that contain photons in the signal side. This ensures that numerator and denominator are distinct and non-overlapping.

To identify signal-side photons, I use the thrust angle, defined as the angle between the thrust vector and the signal track. If the cosine of the thrust angle for the signal τ is positive, then all photons with a positive thrust angle cosine are classified as belonging to the

signal hemisphere, while the remaining photons belong to the tag hemisphere. Conversely, the viceversa holds.

The photon selections used to distinguish the samples are not optimized and are considered as baseline selections applied to split the initial sample. Because this requirement introduces a selection difference between numerator and denominator, equation 3.3, which allows the estimation of the π^0 reconstruction efficiency, must be properly modified to account for the efficiencies of selecting on photons, which is denoted as ε^γ.

All event kinematic variables in both the laboratory and center-of-mass reference frames are saved. In addition, I record the Monte Carlo truth information for each particle, the reconstructed and generated particle matching variables, all event variables associated with each track and each τ. I also save the variables related to the event shape and triggers. All the information is stored in an ntuple. The result are two disjoint samples from which I extract the numerator and denominator signal and I make a first estimate of the π^0 reconstruction efficiency.

5.2 Hemisphere validation

I perform a check to validate in my ntuple the hemisphere construction and photon assignment.

By displaying in the two-dimensional space of the laboratory θ and ϕ coordinates of the signal track, of the tag track, and of each photon in the event, I expect photons labeled as belonging to the tag side to have coordinates close to those of the tag track if the hemisphere construction is correct, and similarly, for the signal track.

Figures 5.1 and 5.2 illustrate the test in the simple case of events in which the τ of the signal hemisphere decays in the channel $\tau^- \to \pi^- \pi^0 \nu_\tau$ (figure 5.1) and only two signal-side photons are reconstructed. To verify the proper separation between tag and signal photons, I repeat the test by requiring two photons in the tag hemisphere (figure 5.2).

In the scatter plots of azimuthal angle versus polar angle, I expect a total of four entries for each event: two related to photons, one related to the signal track and one related to the tag track. The blue point represents the θ and ϕ coordinates of the signal track, the red point the tag track, while the green and yellow points correspond to the coordinates of the two photons, respectively.

The results show that the separation between the signal and tag photons is consistent with expectations confirming the correctness of hemisphere construction and proper association.

5.3 Sample composition and validation of the reconstruction

The goal is to prototype and develop the analysis in a simpler configuration before facing more realisting conditions. As a simplified starting analysis, I use a sample of simulated data containing only τ pairs that decay according to table 4.1. I use about 0.17% of the total available simulated τ-pair data, corresponding to an integrated luminosity of about $\int \mathcal{L}\,dt \approx 2.58$ fb^{-1}. This significantly increases the efficiency of script execution and does not spoil the validity of results. A lepton tag is required in reconstruction.

I determine the true sample composition using the Monte Carlo truth codes available in `TAUOLA`, where each code uniquely corresponds to a decay channel of the generated τ. The sample composition for these samples is given in the tables 5.1 for the denominator and 5.2 for the numerator.
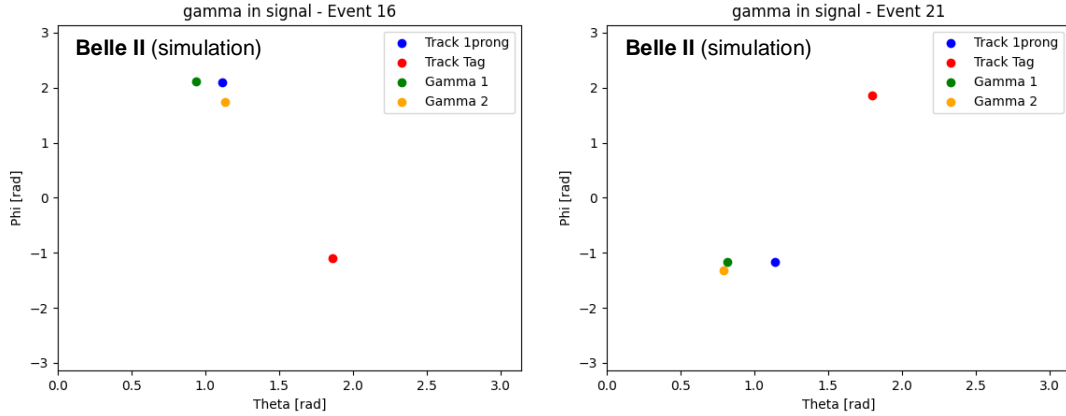
Figure 5.1: Azimuthal angle of simulated signal track, tag track, and photons as a function of polar angle for two selected events in which the τ of the signal hemisphere decays in the channel $\tau^- \to \pi^- \pi^0 \nu_\tau$, and only two photons are detected in the signal hemisphere.
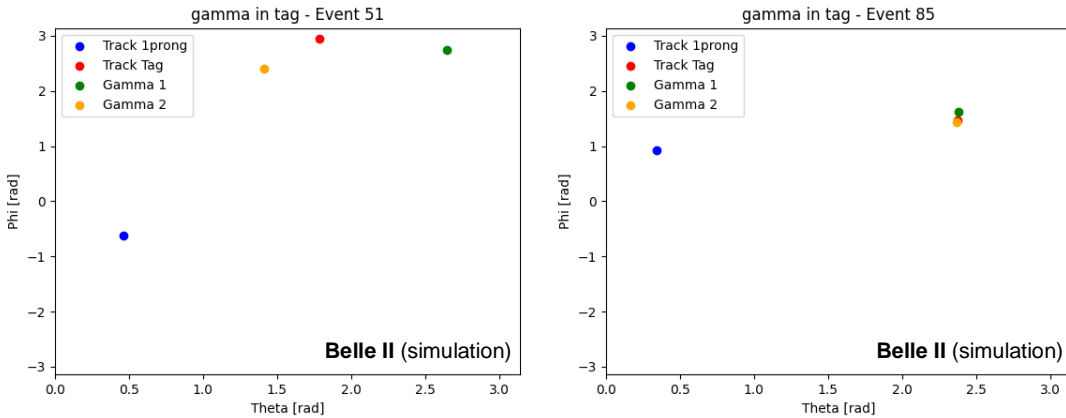
Figure 5.2: Azimuthal angle of simulated signal track, tag track, and photons as a function of polar angle for two selected events in which the τ of the tag hemisphere decays in the channel $\tau^- \to \pi^- \pi^0 \nu_\tau$, and only two photons are detected in the tag hemisphere.

		Denominator
Generation	Number of events	Fraction
$\tau^- \to \pi^- \nu_\tau$	3120	$(17.92 \pm 0.29)\%$
$\tau^- \to \pi^- \pi^0 \nu_\tau$	185	$(1.06 \pm 0.08)\%$
$\tau^- \to \pi^- 2\pi^0 \nu_\tau$	12	$(0.069 \pm 0.020)\%$
$\tau^- \to \pi^- 3\pi^0 \nu_\tau$	2	$(0.011 \pm 0.008)\%$
$\tau^- \to \pi^- 4\pi^0 \nu_\tau$	0	$-$
$\tau^- \to K^- \pi^0 \nu_\tau$	2	$(0.011 \pm 0.008)\%$
$\tau^- \to K^- \nu_\tau$	190	$(1.09 \pm 0.08)\%$
$\tau^- \to e^- \bar{\nu}_e \nu_\tau$	5664	$(32.53 \pm 0.36)\%$
$\tau^- \to \mu^- \bar{\nu}_\mu \nu_\tau$	8174	$(46.95 \pm 0.38)\%$

Table 5.1: Initial simulated denominator sample composition. The processes considered are the same as those listed in table 4.1. The associated uncertainties are statistical and calculated assuming binomial distributions.
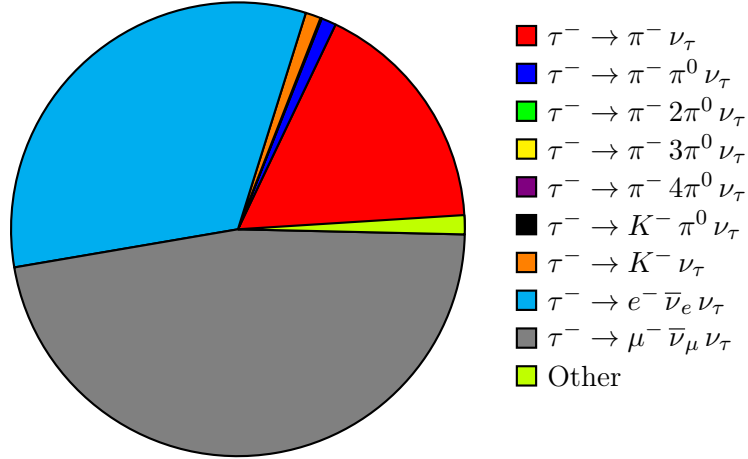
Figure 5.3: Pie chart of the initial simulated denominator sample composition. The processes considered are the same as those listed in table 4.1.

Due to the high branching fraction of leptonic τ decays and the absence of photons in these events, as expected, the predominant contribution to the denominator (table 5.1) are leptonic τ decays.

It is interesting to note how some decay processes involving a π^0 still manage to pass the selection even though that requires absence of photons. This residual contribution is of the order of about 1%. One can explain this background as caused by photons produced by the π^0 decay outside the geometric acceptance of the detector.

		Numerator
Generation	**Number of events**	**Fraction**
$\tau^- \to \pi^- \nu_\tau$	2466	$(13.05 \pm 0.24)\%$
$\tau^- \to \pi^- \pi^0 \nu_\tau$	8652	$(45.77 \pm 0.36)\%$
$\tau^- \to \pi^- 2\pi^0 \nu_\tau$	258	$(1.36 \pm 0.08)\%$
$\tau^- \to \pi^- 3\pi^0 \nu_\tau$	4	$(0.021 \pm 0.011)\%$
$\tau^- \to \pi^- 4\pi^0 \nu_\tau$	0	−
$\tau^- \to K^- \pi^0 \nu_\tau$	129	$(0.68 \pm 0.06)\%$
$\tau^- \to K^- \nu_\tau$	134	$(0.71 \pm 0.06)\%$
$\tau^- \to e^- \overline{\nu}_e \nu_\tau$	3923	$(20.75 \pm 0.29)\%$
$\tau^- \to \mu^- \overline{\nu}_\mu \nu_\tau$	3019	$(15.97 \pm 0.27)\%$

Table 5.2: Initial simulated numerator sample composition. The processes considered are the same as those listed in table 4.1. The associated uncertainties are statistical and calculated assuming binomial distributions.

Due to the high branching fraction of the $\tau^- \to \pi^- \pi^0 \nu_\tau$ decay and the enforced presence of only two photons, the predominant contribution to the numerator (table 5.2) are $\tau^- \to \pi^- \pi^0 \nu_\tau$ decays.

Also leptonic decay processes, and other processes with only one track in the final state, successfully pass the requirement of two photons in the signal hemisphere. These channels make up about 50% of the composition of the total sample. One can explain this
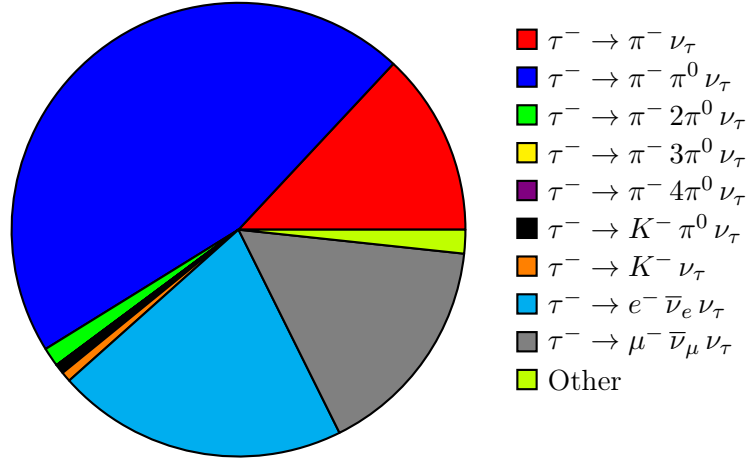
Figure 5.4: Pie chart of the initial simulated numerator sample composition. The processes considered are the same as those listed at table 4.1.

by recalling that leptons and pions often emit photons in the form of final-state radiation. In this case, the photons present in the signal hemisphere do not come from the decay of a π^0 meson, but are emitted by the charged particles themselves.

Then, I perform a qualitative check of the correctness of the reconstruction. This is done by inspecting simple yield ratios between similar decays and comparing them with known rates. Convenient comparisons are available between the processes $\tau^- \to h_1^- \nu_\tau$ and $\tau^- \to h_2^- \nu_\tau$ with $h_i^- = \pi^-, K^-$ and $h_1^- \neq h_2^-$; $\tau^- \to h_1^- \pi^0 \nu_\tau$ and $\tau^- \to h_2^- \pi^0 \nu_\tau$ with $h_i^- = \pi^-, K^-$ and $h_1^- \neq h_2^-$ and between $\tau^- \to \ell_1^- \nu_\tau \overline{\nu}_{\ell_1}$ and $\tau^- \to \ell_2^- \nu_\tau \overline{\nu}_{\ell_2}$ with $\ell_i^- = e^-, \mu^-$ and $\ell_1^- \neq \ell_2^-$. The kinematic properties of these processes are similar and no selection on the particle identification is made. The only major difference concerns the flavor of the charged particle. From the reconstruction point of view, therefore, these channels are approximately equivalent, and I expect the ratio of the number of reconstructed events for each process to be proportional to the native rates, quantified by the ratio of the respective branching fractions [12]. Expressions 5.1, 5.2, 5.3 show the comparison between the ratios of yields and the ratios of branching fractions $\mathcal{B}$ for the denominator. Expressions 5.4, 5.5, 5.6 show similar quantities for the numerator. In both numerator and denominator, the ratios between observed yields and known branching fractions are similar.

Denominator :

$$\frac{N(\tau^- \to K^- \nu_\tau)}{N(\tau^- \to \pi^- \nu_\tau)} = 0.06 \longleftrightarrow \frac{\mathcal{B}(\tau^- \to K^- \nu_\tau)}{\mathcal{B}(\tau^- \to \pi^- \nu_\tau)} = 0.06 \tag{5.1}$$

$$\frac{N(\tau^- \to K^- \pi^0 \nu_\tau)}{N(\tau^- \to \pi^- \pi^0 \nu_\tau)} = 0.011 \longleftrightarrow \frac{\mathcal{B}(\tau^- \to K^- \pi^0 \nu_\tau)}{\mathcal{B}(\tau^- \to \pi^- \pi^0 \nu_\tau)} = 0.017 \tag{5.2}$$

$$\frac{N(\tau^- \to e^- \nu_\tau \overline{\nu}_e)}{N(\tau^- \to \mu^- \nu_\tau \overline{\nu}_\mu)} = 0.7 \longleftrightarrow \frac{\mathcal{B}(\tau^- \to e^- \nu_\tau \overline{\nu}_e)}{\mathcal{B}(\tau^- \to \mu^- \nu_\tau \overline{\nu}_\mu)} = 1.03 \tag{5.3}$$

Numerator :

$$\frac{N(\tau^- \to K^- \nu_\tau)}{N(\tau^- \to \pi^- \nu_\tau)} = 0.05 \longleftrightarrow \frac{\mathcal{B}(\tau^- \to K^- \nu_\tau)}{\mathcal{B}(\tau^- \to \pi^- \nu_\tau)} = 0.06 \tag{5.4}$$

$$\frac{N(\tau^- \to K^- \pi^0 \nu_\tau)}{N(\tau^- \to \pi^- \pi^0 \nu_\tau)} = 0.015 \longleftrightarrow \frac{\mathcal{B}(\tau^- \to K^- \pi^0 \nu_\tau)}{\mathcal{B}(\tau^- \to \pi^- \pi^0 \nu_\tau)} = 0.017 \tag{5.5}$$

$$\frac{N(\tau^- \to e^- \nu_\tau \overline{\nu}_e)}{N(\tau^- \to \mu^- \nu_\tau \overline{\nu}_\mu)} = 1.30 \longleftrightarrow \frac{\mathcal{B}(\tau^- \to e^- \nu_\tau \overline{\nu}_e)}{\mathcal{B}(\tau^- \to \mu^- \nu_\tau \overline{\nu}_\mu)} = 1.03 \tag{5.6}$$

The dataset obtained from the reconstruction produce reasonable results consistent with expectations.

5.4 Selection and optimization

After inspecting the sample composition and verifying that it is consistent with expectations both at the numerator and denominator, I search for discriminating observables to extract the purest possible signal at denominator.

In principle, each selection provides a different level of accuracy in the efficiency estimation. The optimal selection would be defined as the one that minimizes the uncertainty in estimating the final efficiency. This is a task that would require a detailed model of the systematic effects and their interplay with the statistical effects. I consider the above outside the scope of this thesis and I only optimize the denominator purity. The choice is supported primarily by two arguments:

- Allowing a suboptimal numerator is more acceptable than having a suboptimal denominator. The signal yield in the numerator is obtained through a fit of the diphoton mass distribution. In contrast, the yield in the denominator is obtained by just counting events. This implies that it is more likely that background events get included inadvertently in the denominator than in the numerator. A suboptimal numerator sample may include background events that pass the selections, but would be properly separated by the fit. This separation capability is not applicable to the denominator;

- By looking at the sample composition obtained after a few attempts at arbitrary selection on the discriminating observables, I observe that the denominator yield is consistently smaller than the numerator yield. This implies that the final statistical uncertainty on π^0 reconstruction efficiency is likely to be dominated by the statistical uncertainty of the denominator rather than by that of the numerator.

Therefore, optimizing the denominator seems a motivated strategy. Based on the composition of the denominator sample as shown in table 5.1, I identify selection observables that are sensitive to differences between the main backgrounds and signal, and vice versa.

As evidenced by table 5.1, the main backgrounds are leptonic decays $\tau^- \to \ell^- \overline{\nu}_\ell \nu_\tau$, where $\ell^- = e^-, \mu^-$. Given that the principal difference with respect to our denominator is the charged particle, I suppress the leptonic component by applying selections on the pion identification and E/p.

A selection on the pion identification allows to enrich the sample in pions, thereby reducing misidentification events where a muon or an electron is mistaken for a pion.

A selection on E/p is particularly discriminating between events where the charged particle is a pion or a muon and those where it is an electron due to the different interactions these charged particles have.

Figures 5.5 and 5.6, which show the distributions of these observables for simulated signal (shown in red) and for simulated background (shown in blue), illustrate the discriminating power of these observables and substantiate the validity of our observations.
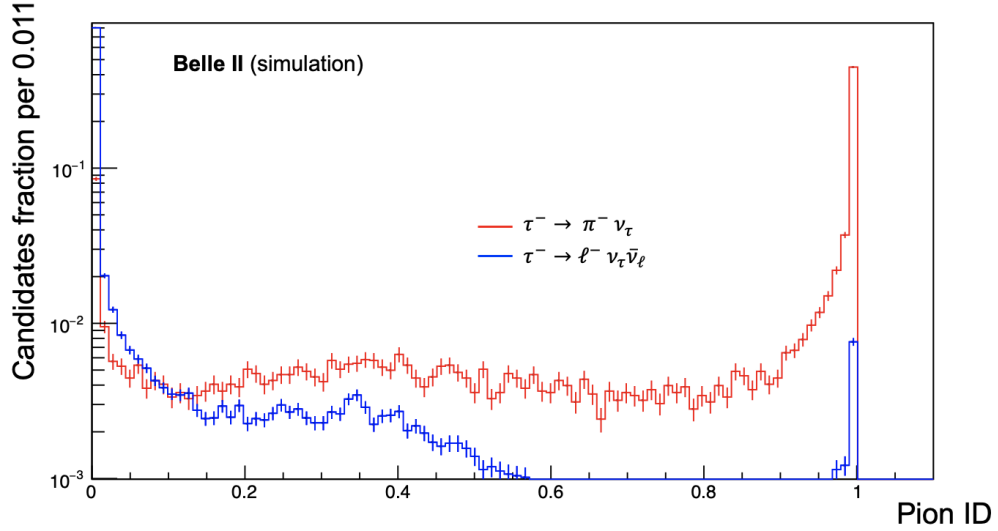
Figure 5.5: Pion particle identification distribution for simulated signal (red) and simulated leptonic background (blue). Distributions are normalized to unity. The integrated luminosity corresponds to $\int \mathcal{L}\, dt = 2.58$ fb^{-1}.
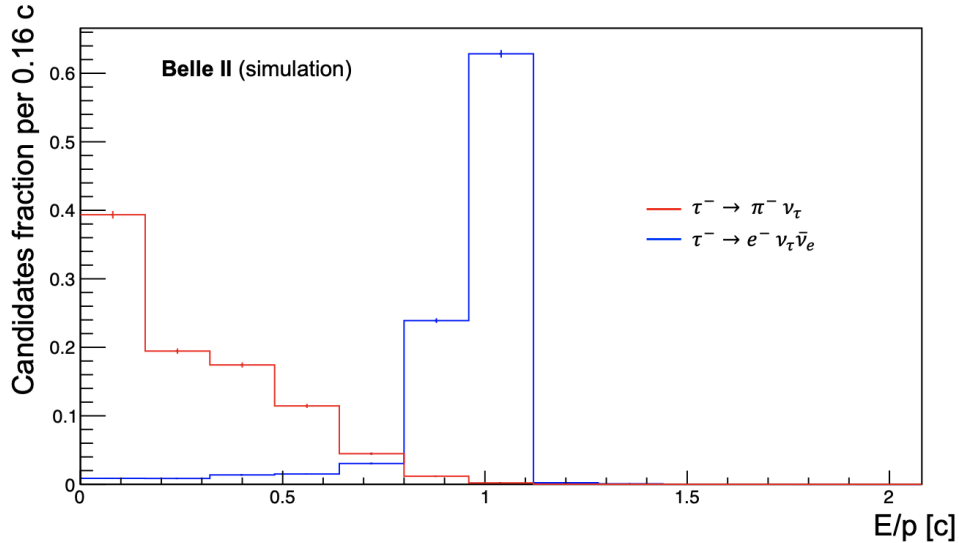
Figure 5.6: E/p distribution for simulated signal (red) and simulated $\tau^- \to e^-\, \nu_\tau\, \overline{\nu}_e$ background (blue). Distributions are normalized to unity. The integrated luminosity corresponds to $\int \mathcal{L}\, dt = 2.58$ fb^{-1}.

I then proceed to optimize the denominator selection criteria for these quantities. In this case, optimization is the process of identifying a configuration of selections on the chosen quantities that maximizes the signal fraction at the denominator. It is crucial to obtain the purest possible sample at the denominator for accurately estimating the signal yield, which in turn allows for a reliable estimation of the desired π^0 reconstruction efficiency.

If the physical quantities are independent, optimizing the selection for each individual observable independently and optimizing the selection for multiple variables simultaneously would yield equivalent results. However, in general it is convenient to perform a multidi-

mensional optimization that considers selections on all observables simultaneously. This approach accounts for potential dependencies and allows for a more accurate approximation of the maximum signal fraction.

I write an optimization program that scans a large number of possible selection criteria to maximize the fraction of signal in the denominator. After defining the range of variation of pion identification and E/p and the number of test selections for each, the program applies the sequence of unique configurations criteria ij to the initial sample, returning the fraction of denominator signal events that meet the selection. This is repeated iteratively until all possible combinations are tested.

Signal is the number of $\tau^- \to \pi^- \nu_\tau$ decays; while the total number of events are events in which the signal τ decays in all possible decay channels (inclusive).

By displaying the fraction of signal corresponding to a selection versus the complete set of pair ij selections (properly parametrized) yields the figure of merit. The absolute maximum of the figure of merit corresponds to the configuration of selections that optimizes the percentage of signal at the denominator.

In this case, I apply 50 different criteria in pion identification, denoted as $0.9 < \pi\mathrm{ID} < 1.0$, 50 criteria in E/p of the track with $0.0 < \mathrm{E/p} < 1.0\ c$. To ensure the bijectivity of the figure of merit, I parametrize the coordinates in the abscissa x as

$$x = i + j * 100 \tag{5.7}$$

with index i identifying the ith requirement in $\pi\mathrm{ID}$ and j the jth requirement in E/p and x the abscissa.

Figure 5.7 shows the resulting figure of merit as a function of selection. Due to the large number of combinations, the resolution of the graph is insufficient to make all structures distinctly visible.

Scanning over each individual observable is associated with a specific pattern. Due to the parametrization chosen, the visible pattern is that related to the index j, which varies on a scale of hundreds (given the same i). At each iteration in j, there is in turn a pattern in which i varies.
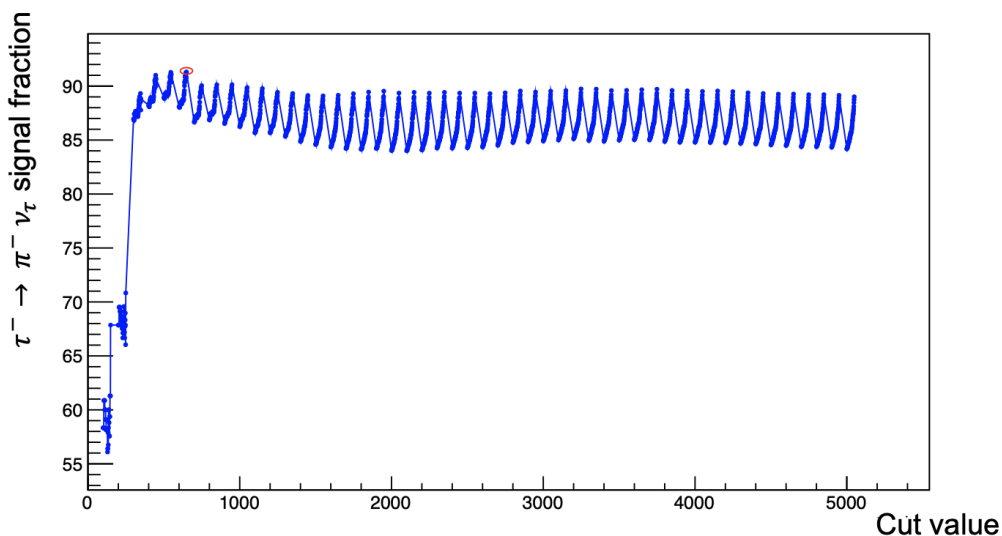
Figure 5.7: Purity as a function of selection in simulation. The maximum is highlighted by a red circle.

The absolute maximum of the denominator fraction derives from the configuration

- πID > 0.998;

- E/p $< 0.12\ c$.

This selection achieves a denominator signal percentage of about 90.91% with 620 signal events remaining.

5.5   Sample composition after optimization

Tables 5.3 and 5.4 show the sample composition obtained after applying the combination of selections derived from the optimization.

Similar to what observed in table 5.1, the main contribution to the denominator background are lepton decays, which remain prevalent even after optimization, accounting for about 6% of the total. In addition, a background contribution of about 2% comes from the channel that forms the numerator of this analysis. The contribution of the remaining processes is suppressed to negligible values.

The purity of the numerator is about 75%. The main contribution to the background comes from a denominator contamination, which accounts for almost 21% of the total. However, this contribution is statistically subtracted in the diphoton mass fit, so there is no pressing need to reduce it further. In addition, a background contribution of about 2% is due to events $\tau^- \to \pi^- 2\pi^0 \nu_\tau$. The remaining contributions are of subpercent order.

		Denominator
Generation	Number of events	Fraction
$\tau^- \to \pi^- \nu_\tau$	620	$(90.91 \pm 1.10)\%$
$\tau^- \to \pi^- \pi^0 \nu_\tau$	14	$(2.05 \pm 0.54)\%$
$\tau^- \to \pi^- 2\pi^0 \nu_\tau$	1	$(0.15 \pm 0.15)\%$
$\tau^- \to \pi^- 3\pi^0 \nu_\tau$	0	–
$\tau^- \to \pi^- 4\pi^0 \nu_\tau$	0	–
$\tau^- \to K^- \pi^0 \nu_\tau$	0	–
$\tau^- \to K^- \nu_\tau$	1	$(0.15 \pm 0.15)\%$
$\tau^- \to e^- \bar{\nu}_e \nu_\tau$	15	$(2.20 \pm 0.56)\%$
$\tau^- \to \mu^- \bar{\nu}_\mu \nu_\tau$	25	$(3.67 \pm 0.72)\%$

Table 5.3: Simulated denominator sample composition resulting from optimization. The processes considered in the signal side are the same as those listed at table 4.1. The associated uncertainty is statistical and is calculated assuming a binomial distribution.
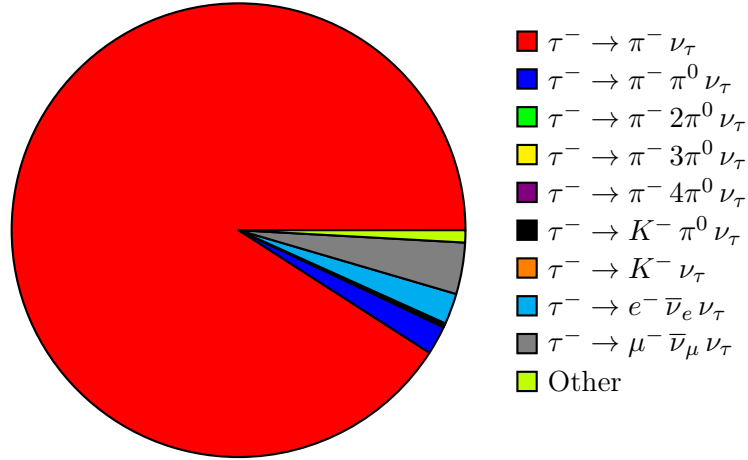
Figure 5.8: Pie chart of the simulated denominator composition resulting from the optimization. The processes considered are the same as those listed at table 4.1.

| | | *Numerator* |
Generation	Number of events	Fraction
$\tau^- \to \pi^- \, \nu_\tau$	258	$(20.69 \pm 1.15)\%$
$\tau^- \to \pi^- \, \pi^0 \, \nu_\tau$	935	$(74.98 \pm 1.22)\%$
$\tau^- \to \pi^- \, 2\pi^0 \, \nu_\tau$	26	$(2.09 \pm 0.40)\%$
$\tau^- \to \pi^- \, 3\pi^0 \, \nu_\tau$	0	–
$\tau^- \to \pi^- \, 4\pi^0 \, \nu_\tau$	0	–
$\tau^- \to K^- \, \pi^0 \, \nu_\tau$	1	$(0.08 \pm 0.08)\%$
$\tau^- \to K^- \, \nu_\tau$	0	–
$\tau^- \to e^- \, \overline{\nu}_e \, \nu_\tau$	3	$(0.24 \pm 0.14)\%$
$\tau^- \to \mu^- \, \overline{\nu}_\mu \, \nu_\tau$	8	$(0.64 \pm 0.22)\%$

Table 5.4: Simulated numerator sample composition resulting from the optimization. The processes considered are the same as those listed at table 4.1. The associated uncertainty is statistical and is calculated assuming a binomial distribution.

5.6 Additional corrections

Equation 3.3 is valid if the kinematic and topological properties of the reconstructed particles are congruent between the two channels. Any difference in the combination of native distributions and selections that results in differences in properties calls for additional corrective terms.

Our approach requires largely different selections for the number of photons in the signal hemisphere between numerator and denominator; therefore, aditional corrections are needed. In addition, there might be kinematic differences between the charged particle at the numerator and at the denominator because the numerator is a three-body process, while the denominator is two-body.

The formula that includes the associated correction terms and allows a consistent estimate of the π^0 meson reconstruction efficiency is
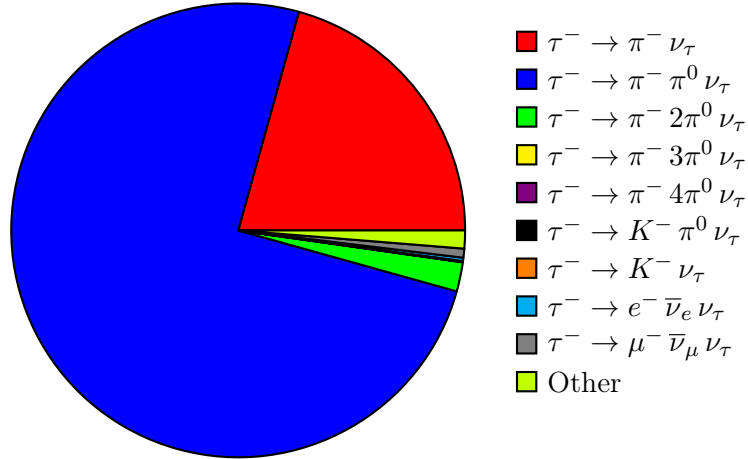
Figure 5.9: Pie chart of the simulated numerator composition resulting from the optimization. The processes considered are the same as those listed at table 4.1.

$$\varepsilon_{\pi^0} = \frac{Y_n\left(\tau^- \to \pi^- \pi^0 \nu_\tau\right)}{Y_d\left(\tau^- \to \pi^- \nu_\tau\right)} \left(\frac{\mathcal{B}(\tau^- \to \pi^- \nu_\tau)}{\mathcal{B}(\tau^- \to \pi^- \pi^0 \nu_\tau) \cdot \mathcal{B}(\pi^0 \to \gamma\,\gamma)}\right) \left(\frac{\varepsilon_d^\gamma \cdot \varepsilon_d^{track}}{\varepsilon_n^\gamma \cdot \varepsilon_n^{track}}\right), \quad (5.8)$$

where ε_n^γ and ε_d^γ represent the selection efficiencies on photons for the numerator and denominator, respectively, while ε_n^{track} and ε_d^{track} represent the selection efficiencies on tracks for the numerator and denominator, respectively. Our approach is to assess these efficiencies using simulation for the purpose of this study. In view of a future application to data, one would need to validate in control samples of data that these corrections are reliably modeled in simulation.

5.6.1 Photon multiplicity selection, ε^γ

The selection efficiency on photons is approximated as the fraction of the number of simulated numerator or denominator events that meet the selection,

$$\varepsilon^\gamma = \frac{N(\text{signal meeting the } \gamma \text{ criterion})}{N(\text{signal})} \quad (5.9)$$

To determine it I start from the simulated sample obtained from reconstruction, without any other selections than those listed in paragraph 5.1. I use Monte Carlo truth to identify the signal $\tau^- \to \pi^- \pi^0 \nu_\tau$ decays for the numerator and $\tau^- \to \pi^- \nu_\tau$ for the denominator. Then I apply the selection on the number of signal-side photons.

The resulting efficiency on the number of photons is

$$\varepsilon_d^\gamma = (23.56 \pm 0.37)\,\% \quad (5.10)$$

for the denominator, and

$$\varepsilon_n^\gamma = (24.86 \pm 0.23)\,\% \quad (5.11)$$

for the numerator. The associated uncertainty is statistical and calculated assuming a binomial distribution for both.

5.6.2 Optimized selection on tracks, ε^{track}

Now I determine the efficiency of the selection that maximizes the purity of the denominator. Since the decays considered involve three bodies and two bodies, respectively, even an identical selection can isolate different kinematic properties between numerator and denominator for the charged particle of each decay. It is crucial to account for these dynamic differences by quantifying them and checking possible discrepancies between selection efficiencies.

Such efficiency is defined as the fraction of signal events meeting the optimized selection,

$$\varepsilon^{track} = \frac{N(\text{signal meeting track criterion})}{N(\text{signal})}. \tag{5.12}$$

Starting from the sample used in the previous section, I use Monte Carlo truth to identify the decays $\tau^- \to \pi^- \pi^0 \nu_\tau$ for the numerator and $\tau^- \to \pi^- \nu_\tau$ for the denominator.

I then add to the previous conditions the optimized selection on πID and E/p discussed in section 5.4 .

The resulting selection efficiency on the application of the optimized selections is

$$\varepsilon_d^{track} = (16.51 \pm 0.66)\,\% \tag{5.13}$$

for the denominator, and

$$\varepsilon_n^{track} = (10.81 \pm 0.33)\,\%, \tag{5.14}$$

for the numerator. The associated uncertainty is statistical and calculated assuming a binomial distribution in both.

The difference in selection efficiencies might seem counterintuitive and unexpected. However, the source of the difference can be identified.

Our optimized selection includes a requirement on particle identification. The efficiency of particle identification is a function of several properties of the charged particle, including the momentum and the orientation in θ and ϕ of the track. Considering that the numerator is a three-body decay, while the signal denominator is a two-body decay, it is plausible that kinematic differences between the pion at the numerator and the pion at the denominator exist that yield different particle identification performances.

To verify this hypothesis, I equalize the kinematic properties between the two channels by restricting to a narrow charged particle momentum region in both the numerator and denominator. In this region, I estimate the efficiency of the optimized selections for both the numerator and the denominator thus reducing possible momentum dependence. If the hypothesis is correct, I would expect to observe selection efficiencies for the numerator and denominator closer than those found in equation 5.13 and 5.14.

Figure 5.10 shows the distribution of momentum for both simulated numerator and denominator. I restrict the analysis to a very narrow momentum interval, $2 < p_{track} < 2.1$ GeV/c.

For the denominator in the $2 < p_{track} < 2.1$ GeV/c momentum range the efficiency on the application of the optimized selections in this restricted range is

$$\varepsilon_d^{track} = (33.7 \pm 5.0)\,\%, \tag{5.15}$$

which is consistent with the result on the numerator,

$$\varepsilon_n^{track} = (29.6 \pm 3.8)\,\%. \tag{5.16}$$

However, the statistical uncertainties are large and hinders a precise check.
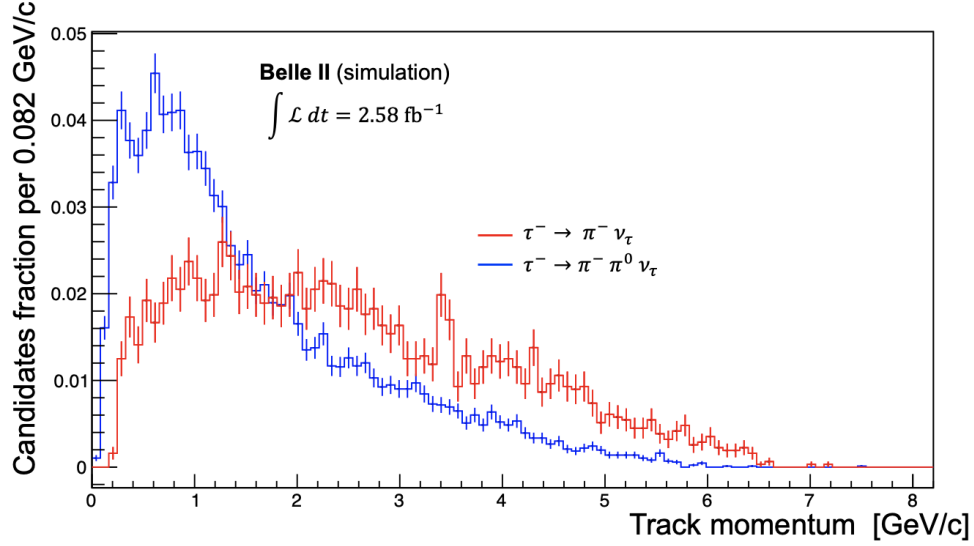
Figure 5.10: Distribution of the charged-particle momentum for simulated numerator signal $\tau^- \to \pi^- \pi^0 \nu_\tau$ (blue) and for denominator signal $\tau^- \to \pi^- \nu_\tau$ (red). Distributions are normalized to unity. The integrated luminosity corresponds to $\int \mathcal{L} \, dt = 2.58 \text{ fb}^{-1}$.

A second approach is to select a region in which the momentum spectra of the numerator and denominator signals are similar. I look for a *plateau* region that allows for a larger sample. In this case, I choose a region between $3 < p_{track} < 3.5$ GeV/c obtaining

$$\varepsilon_d^{track} = (22.8 \pm 2.5)\,\%, \tag{5.17}$$

which is consistent with the result on the numerator,

$$\varepsilon_d^{track} = (22.3 \pm 2.0)\,\%. \tag{5.18}$$

These results indicate that the efficiency discrepancies in the initial optimized selections, are attributable to the fact that the signal at the numerator and denominator have different spectra in momentum and orientation.

For further confirmation, it would be useful to perform similar restrictions in angle θ. However, due to the significant reduction in sample size of events passing this further selection, I do not perform this additional test, deeming the momentum study sufficiently convincing.

5.7 Inputs to the π^0 reconstruction efficiency

For the corrective factors of the efficiency,

$$\varepsilon_{\pi^0} = \frac{Y_n\left(\tau^- \to \pi^- \pi^0 \nu_\tau\right)}{Y_d\left(\tau^- \to \pi^- \nu_\tau\right)} \left(\frac{\mathcal{B}(\tau^- \to \pi^- \nu_\tau)}{\mathcal{B}(\tau^- \to \pi^- \pi^0 \nu_\tau) \cdot \mathcal{B}(\pi^0 \to \gamma\,\gamma)}\right) \left(\frac{\varepsilon_d^\gamma \cdot \varepsilon_d^{track}}{\varepsilon_n^\gamma \cdot \varepsilon_n^{track}}\right). \tag{5.19}$$

I find the following values:

- $\varepsilon_n^\gamma = (24.86 \pm 0.23)\%$;

- $\varepsilon_d^{\gamma} = (23.56 \pm 0.37)\%$;

- $\varepsilon_n^{track} = (10.81 \pm 0.33)\%$;

- $\varepsilon_d^{track} = (16.51 \pm 0.66)\%$;

- $\dfrac{\mathcal{B}(\tau^- \to \pi^- \nu_\tau)}{\mathcal{B}(\tau^- \to \pi^- \pi^0 \nu_\tau) \cdot \mathcal{B}(\pi^0 \to \gamma\,\gamma)} = 0.430 \pm 0.003$.

The ratio of the branching fractions of the relevant processes is determined by taking values and uncertainties from known values [12]. The associated total uncertainty is calculated by considering all decay channels independent of each other and applying standard uncertainty propagation.

All terms of equation 5.19 are known except the signal yields at the numerator and denominator. In the next paragraphs, I focus on estimating these two missing quantities. This first efficiency estimate is made as a validation against a known selection, which according to standard and independent Belle II determinations should be about 40%. However, before proceeding, I briefly study also the composition of the tag side of the event.

5.8   Tag sample composition

So far, I have not considered the composition of the tag sample, implicitly assuming that, (*i*) as a result of the reconstruction, the tag is predominantly composed of leptonic decays and (*ii*) any imperfections or impurity in the tag reconstruction does not affect the π^0 efficiency estimate since signal and tag are hemispheres are independent. However, the reconstruction process is known to be prone to inaccuracies and unexpected signal-tag correlation could make the assumptions unrealistic. I therefore verify the expected independence between the signal and tag hemispheres and if imperfections may affect the π^0 efficiency. For this purpose, I analyze the tag composition and its evolution as a function of the various selection criteria applied to the signal hemisphere. If the composition remains stable through the various selection steps, I can conclude that the two hemispheres are indeed independent and that the efficiency estimation method is robust against tag imperfections.

Tables 5.5 and 5.6 show the tag-side sample composition and its evolution as a function of the selection criteria applied in the signal hemisphere in the following cases: simulated data without any selection but those used in reconstruction (columns two and three), sample after the selection on the number of photons in the signal hemisphere (columns four and five), and sample after optimized selections on the tracks (columns six and seven). In these tables, no explicit restriction is applied to the true composition of the signal τ sample.

Before any selection about 15% of the tags are not actually leptonic. However, this significant impurity of the tag side is irrelevant since tables 5.5 and 5.6 indicate that, for the main decay channels relevant in this study, the sample composition remain essentially unchanged as a function of signal selections. The most significant discrepancy is found to be compatible within 3σ.

Hence, the tag hemisphere is independent of the signal hemisphere and any inaccuracies in the reconstruction of the tag track do not affect the π^0 reconstruction efficiency.

	No selections		γ selections		γ and optimized selections	
Channel	**Yield**	**%**	**Yield**	**%**	**Yield**	**%**
$\tau^- \to \pi^- \nu_\tau$	3471	$(2.71 \pm 0.05)\%$	603	$(2.87 \pm 0.12)\%$	18	$(2.64 \pm 0.61)\%$
$\tau^- \to \pi^- \pi^0 \nu_\tau$	11624	$(9.09 \pm 0.08)\%$	1976	$(9.41 \pm 0.20)\%$	72	$(10.56 \pm 1.18)\%$
$\tau^- \to \pi^- 2\pi^0 \nu_\tau$	4068	$(3.18 \pm 0.05)\%$	727	$(3.46 \pm 0.13)\%$	21	$(3.08 \pm 0.66)\%$
$\tau^- \to \pi^- 3\pi^0 \nu_\tau$	464	$(0.36 \pm 0.02)\%$	86	$(0.41 \pm 0.04)\%$	4	$(0.59 \pm 0.29)\%$
$\tau^- \to \pi^- 4\pi^0 \nu_\tau$	50	$(0.039 \pm 0.006)\%$	3	$(0.014 \pm 0.008)\%$	0	–
$\tau^- \to K^- \pi^0 \nu_\tau$	46	$(0.036 \pm 0.005)\%$	7	$(0.03 \pm 0.01)\%$	0	–
$\tau^- \to K^- \nu_\tau$	87	$(0.068 \pm 0.007)\%$	17	$(0.08 \pm 0.02)\%$	0	–
$\tau^- \to e^- \overline{\nu}_e \nu_\tau$	55795	$(43.63 \pm 0.14)\%$	8963	$(42.71 \pm 0.34)\%$	296	$(43.40 \pm 1.90)\%$
$\tau^- \to \mu^- \overline{\nu}_\mu \nu_\tau$	51311	$(40.13 \pm 0.14)\%$	8448	$(40.25 \pm 0.34)\%$	268	$(39.30 \pm 1.87)\%$

Table 5.5: Simulated tag sample composition as a function of selection criteria progressively applied in the signal hemisphere. Downstream of the photon selections, the sample considered is the denominator sample. The associated uncertainty is statistical and is calculated assuming a binomial distribution.

	No selections		γ selections		γ and optimized selections	
Channel	**Yield**	**%**	**Yield**	**%**	**Yield**	**%**
$\tau^- \to \pi^- \nu_\tau$	3471	$(2.71 \pm 0.05)\%$	611	$(2.71 \pm 0.11)\%$	29	$(1.98 \pm 0.36)\%$
$\tau^- \to \pi^- \pi^0 \nu_\tau$	11624	$(9.09 \pm 0.08)\%$	2003	$(8.90 \pm 0.19)\%$	130	$(8.87 \pm 0.74)\%$
$\tau^- \to \pi^- 2\pi^0 \nu_\tau$	4068	$(3.18 \pm 0.05)\%$	726	$(3.22 \pm 0.12)\%$	46	$(3.14 \pm 0.46)\%$
$\tau^- \to \pi^- 3\pi^0 \nu_\tau$	464	$(0.36 \pm 0.02)\%$	67	$(0.30 \pm 0.04)\%$	3	$(0.20 \pm 0.12)\%$
$\tau^- \to \pi^- 4\pi^0 \nu_\tau$	50	$(0.039 \pm 0.006)\%$	6	$(0.03 \pm 0.01)\%$	0	–
$\tau^- \to K^- \pi^0 \nu_\tau$	46	$(0.036 \pm 0.005)\%$	9	$(0.04 \pm 0.01)\%$	0	–
$\tau^- \to K^- \nu_\tau$	87	$(0.068 \pm 0.007)\%$	12	$(0.05 \pm 0.02)\%$	1	$(0.068 \pm 0.068)\%$
$\tau^- \to e^- \overline{\nu}_e \nu_\tau$	55795	$(43.63 \pm 0.14)\%$	9821	$(43.62 \pm 0.33)\%$	665	$(45.39 \pm 1.30)\%$
$\tau^- \to \mu^- \overline{\nu}_\mu \nu_\tau$	51311	$(40.13 \pm 0.14)\%$	9082	$(40.33 \pm 0.33)\%$	582	$(39.37 \pm 1.28)\%$

Table 5.6: Simulated tag sample composition as a function of selection criteria progressively applied in the signal hemisphere. Downstream of the photon selections, the sample considered is the numerator sample. The associated uncertainty is statistical and is calculated assuming a binomial distribution.
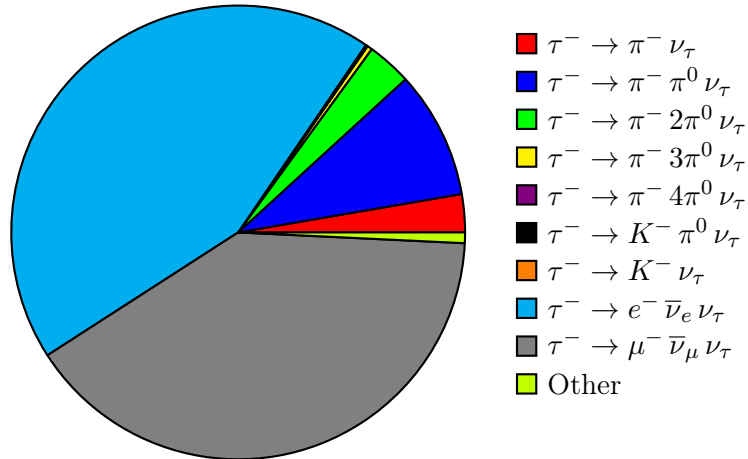
Figure 5.11: Pie chart of the simulated tag sample composition without any selection. The processes considered are the same as those listed at table 4.1.

5.9 Estimation of the number of $\tau^- \to \pi^- \nu_\tau$ events (denominator)

The denominator process $\tau^- \to \pi^- \nu_\tau$ does not offer a straightforward characteristic distribution that can be fit. Therefore, I proceed to estimate the signal yield by counting the number of remaining events following the application of all selections.

All events that pass the optimized selections *number of signal* $\gamma = 0$, πID > 0.998, and E/p < 0.12 c, are considered signal events at the denominator and contribute to the final estimate of the signal yield which is

$$Y_d(\tau^- \to \pi^- \nu_\tau) = (682 \pm 26), \tag{5.20}$$

where the associated uncertainty is statistical, and assumed distributed as a Poisson since these are counts.

However, a fraction of those event are not genuine $\tau^- \to \pi^- \nu_\tau$ but other sources. This approach makes the results dependent on the purity of the denominator: suboptimal purity results in overestimation of the total yield of signal events at the denominator, causing an underestimation of the final efficiency.

5.9.1 Correction for denominator impurity

Taking into account the sample composition of table 5.3, only 620 events out of 682, about 90.91%, are actually signal events generated as $\tau^- \to \pi^- \nu_\tau$. The remaining approximately 9.1% are background events that meet the optimized selections and in our approach would be erroneously considered as denominator signal events. Hence, I apply this additional 9% correction to the π^0 reconstruction efficiency.

5.10 Estimation of the number of $\tau^- \to \pi^- \pi^0 \nu_\tau$ events (numerator)

I determine $Y_n(\tau^- \to \pi^- \pi^0 \nu_\tau)$ with a fit of the invariant mass distribution of the two photons reconstructed in the signal hemisphere.

I apply to the numerator sample a standard combination of selections on all photons in the event, which, based on standard and independent Belle II determinations, is expected to yield an efficiency of approximately 40%:

- Number of activated crystals > 1.5: each of the photons must release energy in more than one crystal since the development of the electromagnetic shower normally extends in the lateral direction exciting multiple crystals, while electronic noise is typically confined to a single crystal;

- $0.2967 <$ cluster's polar angle $\theta < 2.6180$: polar angle of the cluster is within the CDC;

- if the photon is detected in the forward region of the calorimeter, it must have an energy greater than 0.08 GeV; if in the barrel, it must have an energy greater than 0.03 GeV; if in the backward, it must have an energy greater than 0.06 GeV. This requirement accounts for polar-dependent differences in the distribution of photon backgrounds;

- invariant digamma mass range $0.120 < m(\gamma\gamma) < 0.145$ GeV/c^2.

With these selections on the photons, I reconstruct the π^0 invariant mass using the photons kinematic variables and

$$m(\gamma\gamma) = \sqrt{2E_1 E_2 \left(1 - \cos\theta\right)} \tag{5.21}$$

where E_i is the energy of the ith photon and θ the angle beetween the two photons in the laboratory frame.

Figure 5.12 shows the result. As expected, the distribution shows a clear peak centered around the π^0 mass, about 0.135 GeV/c^2 [12].
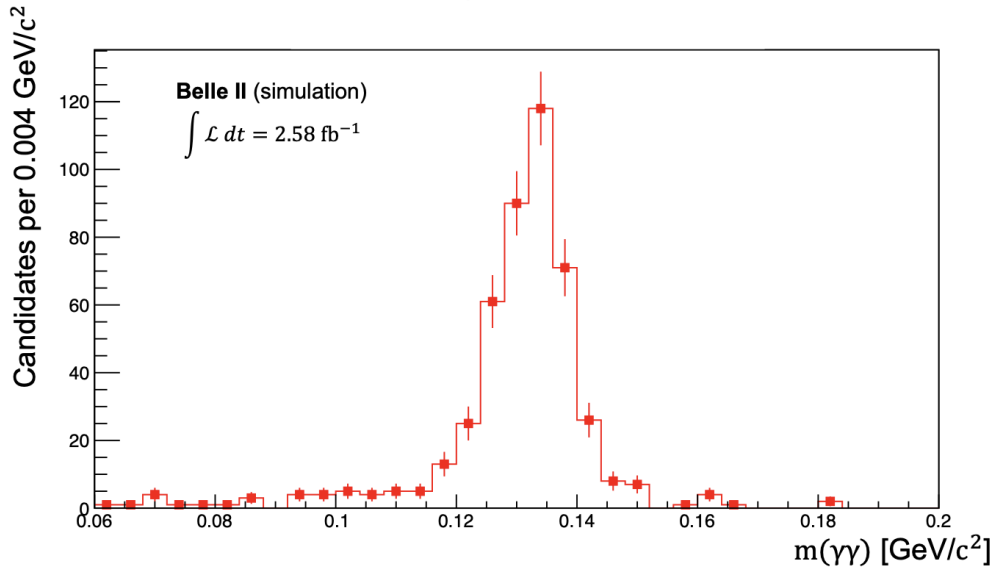
Figure 5.12: Diphoton mass distribution obtained in the simulated numerator sample. The integrated luminosity corresponds to $\int \mathcal{L}\, dt = 2.58$ fb^{-1}.

In order to extract the numerator signal yield at the numerator $Y_n(\tau^- \to \pi^- \pi^0 \nu_\tau)$ I fit the distribution of figure 5.12.

The distribution shows a central peak with asymmetric tails. I model it with a Crystal Ball function [67], a function commonly used in particle physics, which intuitively combines of a core Gaussian function and an exponential power function for the tails

$$f\left(x; \alpha, n, m_0, \sigma\right) = N \cdot \begin{cases} \exp\left(-\frac{(x-m_0)^2}{2\sigma^2}\right), & \text{for } \frac{x-m_0}{\sigma} > -\alpha \\[2mm] A \cdot \left(B - \frac{x-m_0}{\sigma}\right)^{-n}, & \text{for } \frac{x-m_0}{\sigma} \le -\alpha, \end{cases} \tag{5.22}$$

where x is the digamma mass, α is an asymmetry parameter, n represents the tail exponent, m_0 is the parameter representing the mean of the distribution, and σ represents the width of the Gaussian component. The last four are free parameters in the modeling fit and the following relations hold

$$A = \left(\frac{n}{|\alpha|}\right)^n \cdot \exp\left(-\frac{|\alpha|^2}{2}\right),$$

$$B = \frac{n}{|\alpha|} - |\alpha|,$$

$$N = \frac{1}{\sigma(C+D)}, \tag{5.23}$$

$$C = \frac{n}{|\alpha|} \cdot \frac{1}{n-1} \cdot \exp\left(-\frac{|\alpha|^2}{2}\right),$$

$$D = \sqrt{\frac{\pi}{2}} \left(1 + \mathrm{erf}\left(\frac{|\alpha|}{\sqrt{2}}\right)\right).$$

The background follows an exponential distribution $e^{-\lambda x}$, where x represents the $\gamma\gamma$ invariant mass in GeV/c^2 and the slope λ is a free parameter.

The full model is

$$PDF = N_s \cdot PDF_s + N_b \cdot PDF_b \tag{5.24}$$

where N_s represents the signal yield in the interval used in the fit, N_b the background yield, PDF_s the fit model for signal events, and PDF_b that for background events.

In addition to the signal and background yields, the model has five shape parameters to be estimated: four related to the signal shape and one related to the background shape.

I use the default software package Minuit from the RooFit framework [68]. By default, Minuit uses the MIGRAD (gradient minimization) algorithm. The function to be minimized, is $-2log(\mathcal{L})$, where

$$\mathcal{L} = \prod_i \frac{e^{-\nu_i}(\nu_i^{n_i})}{(n_i)!}$$

is the binned likelihood function, which is the product of the individual likelihood functions for Poissonian distributed variables. The i index runs on the number of bins in the histogram, n_i is the number of observed events for the ith bin, and ν_i is the expectation value of the Poisson mean of the ith bin.

The result of the fit is shown in figure 5.13. The parameter relevant for the π^0 reconstruction efficiency N_s is

$$N_s = (428 \pm 26), \tag{5.25}$$

where the uncertainty is statistical as obtained from the fit. This differs from the numerator, $Y_n(\tau^- \to \pi^- \pi^0 \nu_\tau)$ because the standard photon selection we are validating against includes a restriction on the π^0 mass range $0.120 < m(\gamma\gamma) < 0.145$ GeV/c^2 while N_s is the yield over the entire fitting range.

Hence, the fit should be corrected by a factor of about 9% to equalize the diphoton mass range to the range relevant for $Y_n(\tau^- \to \pi^- \pi^0 \nu_\tau)$ and obtain

$$Y_n(\tau^- \to \pi^- \pi^0 \nu_\tau) = (389 \pm 21). \tag{5.26}$$

At this point, I have estimates for all terms of equation 5.19 and I am able to calculate the π^0 reconstruction efficiency. This estimate is then compared with the known value for the chosen π^0 selection, which is known to be 40% based on independent Belle II determinations.

5.11 First estimate of the π^0 reconstruction efficiency

By inserting the values of the various terms
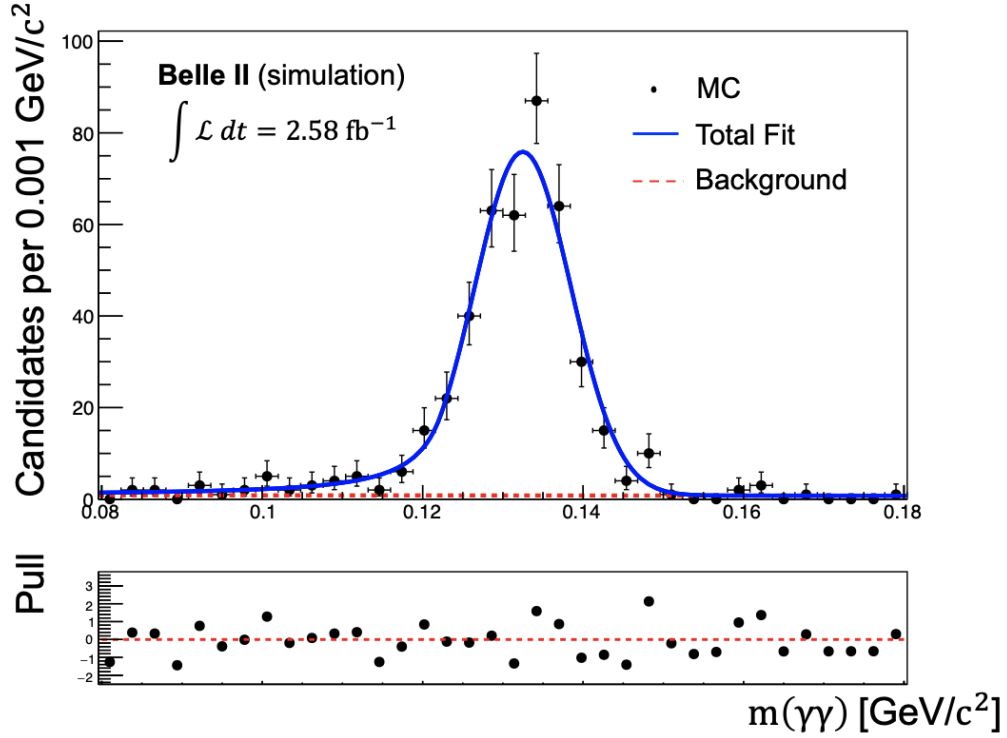
Figure 5.13: (Above): Diphoton mass distribution for simulated numerator events with fit overlaid. Simulated data are shown in black, the total fit is shown in blue and the background fit is shown as a dashed red line. The integrated luminosity corresponds to $\int \mathcal{L}\, dt = 2.58$ fb^{-1}. (Bottom): difference between observed and predicted values, divided by the standard deviation of the observed values.

- $Y_n(\tau^- \to \pi^- \pi^0 \nu_\tau) = (389 \pm 21)$;

- $Y_d(\tau^- \to \pi^- \nu_\tau) = (682 \pm 26)$;

- $\frac{\mathcal{B}(\tau^- \to \pi^- \nu_\tau)}{\mathcal{B}(\tau^- \to \pi^- \pi^0 \nu_\tau) \cdot \mathcal{B}(\pi^0 \to \gamma\gamma)} = (0.430 \pm 0.003)$;

- $\varepsilon_n^\gamma = (24.86 \pm 0.23)\%$;

- $\varepsilon_d^\gamma = (23.56 \pm 0.37)\%$;

- $\varepsilon_n^{track} = (10.81 \pm 0.33)\%$;

- $\varepsilon_d^{track} = (16.51 \pm 0.66)\%$,

along with the 9% correction that takes into account for the bias due to the impurity of the sample at the denominator, into the equation defining the π^0 meson reconstruction efficiency

$$\varepsilon_{\pi^0} = \frac{Y_n\left(\tau^- \to \pi^- \pi^0 \nu_\tau\right)}{Y_d\left(\tau^- \to \pi^- \nu_\tau\right)} \left(\frac{\mathcal{B}\left(\tau^- \to \pi^- \nu_\tau\right)}{\mathcal{B}\left(\tau^- \to \pi^- \pi^0 \nu_\tau\right) \cdot \mathcal{B}\left(\pi^0 \to \gamma\gamma\right)}\right) \left(\frac{\varepsilon_d^\gamma \cdot \varepsilon_d^{track}}{\varepsilon_n^\gamma \cdot \varepsilon_n^{track}}\right), \quad (5.27)$$

the first estimate of the π^0 efficiency using our approach is achieved,

$$\varepsilon_{\pi^0} = (39.6 \pm 3.3)\% \qquad\qquad (5.28)$$

where the associated uncertainty is statistical and based on standard uncertainty propagation.

The result is compatible with the expected value of 40% known from independent studies. The efficiency exhibits a relative uncertainty of 8%, significantly higher than the subpercent precision goal our method could theoretically achieve. However, this is expected. A closer analysis of the terms contributing to the efficiency estimate suggests that most of them contribute similarly to the final uncertainty, with an incidence on the order of one percent each. However, most of them are statistical in nature and will reduce once the method is consolidated and a dataset with larger size will be used.

We explore if there is a way to further increase the purity of the signal at the denominator, thereby reducing the magnitude of the correction for non-purity and consequently decreasing the systematic uncertainty without compromising excessively the sample size, which would result in an increase in statistical uncertainty.

5.12 Further developments

5.12.1 A new discriminating observable

The sample composition given in table 5.3 shows that the main (5.9%) source of impurity in the denominator are leptonic decays followed by about 2% of $\tau^- \to \pi^- \pi^0 \nu_\tau$ decays. A possible strategy to reduce the second source would be to select on the momentum of the charged particle exploiting the differences between two- and three-body decays. However, applying a selection based on momentum variable may result in a significant restriction of the π^0 momentum range, thus limiting the applicability of our approach. In fact, as shown in figure 5.14, progressively stringent upper bounds on the charged-particle momentum results in progressive reductions of the π^0 momentum range.

As for leptonic decays, they, too, are three-body decays, as opposed to the two-body signal channel, and thus exhibit different kinematic properties. Again, a selection on the momentum of the charged particle could provide discrimination against this background, but the π^0 momentum limitation persists. Alternatively, discrimination between signal and leptonic background may be based on the presence of two neutrinos in the leptonic final states, compared with one neutrino in signal. The missing energy, defined as the difference between the expected total energy of the system (based on collision energy conservation) and the sum of the energies measured from reconstructed particles, is expected to be higher on average in leptonic decays than in signal. An additional selection based on missing energy could improve the purity of the signal at the denominator, reducing leptonic background processes and significantly decreasing the size of the needed correction.

However, it is important to evaluate the penalty in sample size after any further selection is applied. A selection that ensures denominator purity close to 100% but significantly reduces sample size, leading to an increase in relative statistical uncertainty, may not be optimal and would not represent improvement. The goal is to optimize the purity of the signal at the denominator while keeping a sufficient number of remaining events.

Figure 5.15 shows the distributions of missing energy in the center-of-mass reference frame for events with a leptonic decay in the signal hemisphere and for events with signal denominator. On average, leptonic decays (blue) have higher missing energy than signal decays (red), a difference that can be exploited.
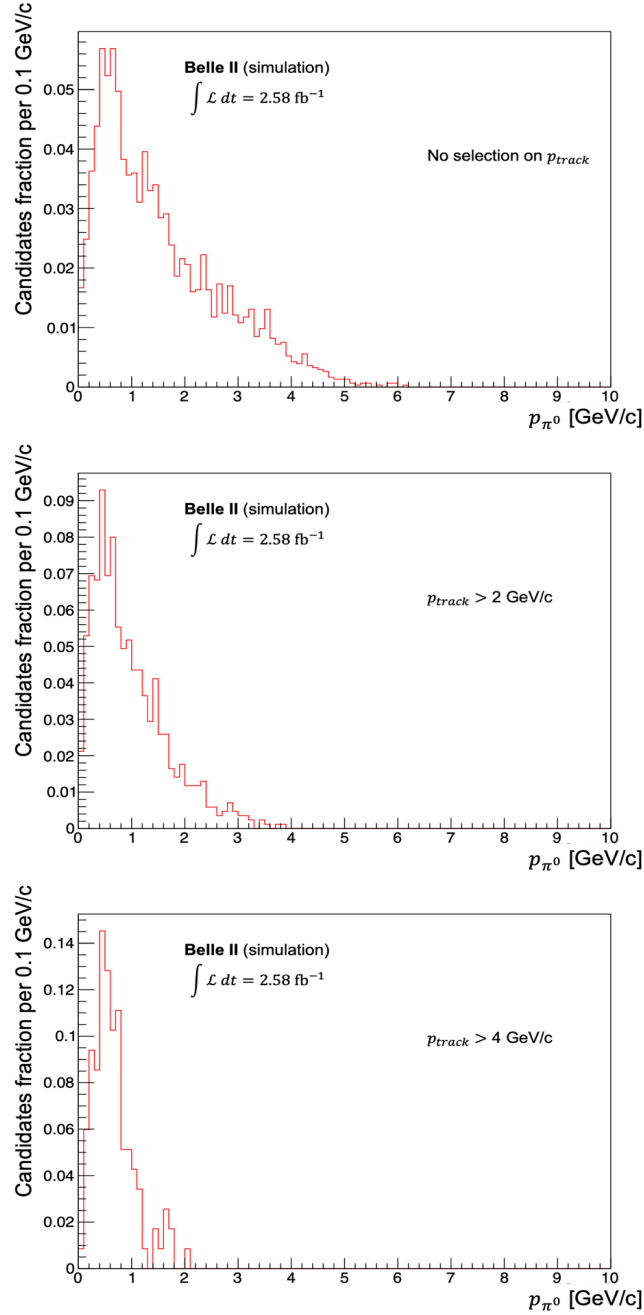
Figure 5.14: Distributions of π^0 momentum as functions of selection on the momentum of the charged-particle in the signal hemisphere for simulated signal events. (Top panel): distribution obtained without any selection on charged-particle momentum; (Middle panel): distribution resulting from applying $p_{track} > 2$ GeV$/c$; (Bottom panel): distribution obtained by imposing $p_{track} > 4$ GeV$/c$. The integrated luminosity corresponds to $\int \mathcal{L}\, dt = 2.58$ fb^{-1}.

I therefore explore further this promising observable. I explore about ten selections in the energy range $1.5 < E_{miss} < 9.5$ GeV. For simplicity, I keep fixed all other selections even though a simultaneous multidimensional selection could offer further advantage.

Denominator signal purity is defined as the ratio of the number of denominator signal
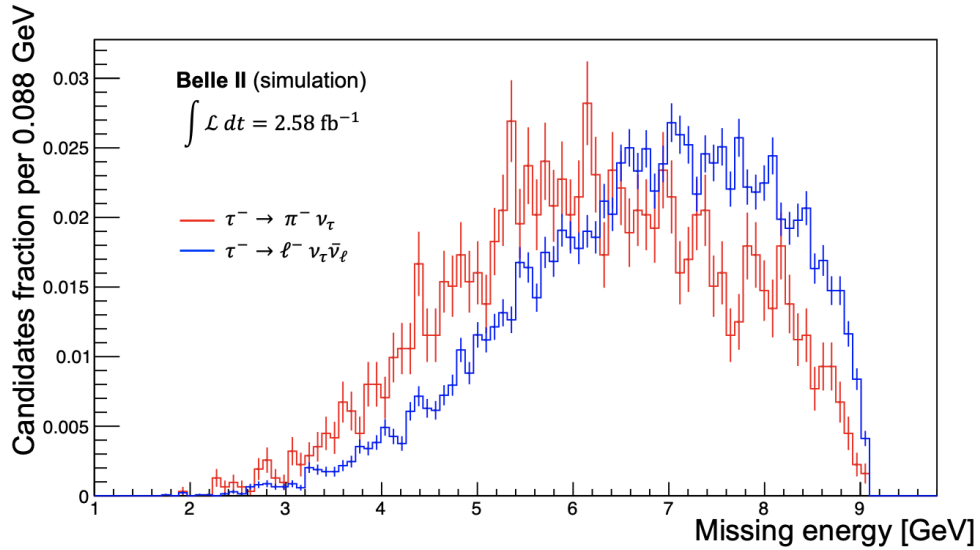
Figure 5.15: Distribution of missing energy of the event in the center-of-mass frame. The denominator signal is the red component ($\tau^- \to \pi^- \nu_\tau$), while the leptonic background ($\tau^- \to \ell^- \bar{\nu}_\ell \nu_\tau$) is the blue histogram. Both distributions are normalized to unity. The integrated luminosity corresponds to $\int \mathcal{L}\, dt = 2.58$ fb^{-1}.

events that meet all imposed selection criteria to the total number of events that meet those criteria.

Requirement	Signal yield	Normalization yield	Signal purity
$E_{miss} < 1.5$ GeV	0	0	–
$E_{miss} < 2.3$ GeV	2	2	100%
$E_{miss} < 3.1$ GeV	13	13	100%
$E_{miss} < 3.9$ GeV	32	33	96.97%
$E_{miss} < 4.7$ GeV	90	94	95.74%
$E_{miss} < 5.5$ GeV	185	191	96.86%
$E_{miss} < 6.3$ GeV	320	335	95.52%
$E_{miss} < 7.1$ GeV	420	448	93.75%
$E_{miss} < 7.9$ GeV	485	527	92.03%
$E_{miss} < 8.7$ GeV	515	564	91.31%
No restriction	515	564	91.31%

Table 5.7: Signal purity in the denominator as a function of selection in missing energy.

Table 5.7 shows the results. A requirement on the missing energy allows for a significant increase in the denominator signal purity. However, this increase results in a significant reduction of the sample size. Thus, a possibly useful selection would be one that maximizes the purity of the signal while minimizing the increase in statistical uncertainty due sample-size reduction.

A selection that approximately satisfies this requirement is $E_{miss} < 6.3$ GeV. In this configuration I lose about 38% of signal paying an (absolute) 1.2% increase in statistical

uncertainty but gaining a 4.4% (absolute) in purity.

This is a simple demonstration that it is possible to further increase the denominator purity while maintaining sufficient data size.

5.12.2 Robustness versus π^0 selection

In order to further validate the robustness of our approach against π^0 selection criteria, I apply it to a different class of photons reconstructed with looser selection criteria and known to yield π^0 with 50% efficiency from an independent analysis. The selections are

- Number of activated crystals > 1.5;

- $0.2967 <$ cluster's polar angle $\theta <2.6180$;

- if the photon is detected in the forward region of the calorimeter, it must have an energy greater than 0.025 GeV; if in the barrel, it must have an energy greater than 0.025 GeV; if in the backward, it must have an energy greater than 0.04 GeV;

- invariant digamma mass range $0.105 < m(\gamma\gamma) < 0.150$ GeV/c^2.

Using equation 5.27, which defines the reconstruction efficiency with the appropriate corrective terms, all the quantities obtained in the case of the selections at 40% remain unchanged except for the signal yield at the numerator $Y_n(\tau^- \to \pi^- \pi^0 \nu_\tau)$. To estimate it I perform an additional fit on the diphoton mass with the same model as in section 5.10.

The fit result is shown in figure 5.16.

The resulting number of signal events is

$$N_s = (493 \pm 29), \tag{5.29}$$

where the uncertainty is statistical and obtained from the fit. The resulting numerator, properly rescaled in the appropriate diphoton mass interval, equals

$$Y_n(\tau^- \to \pi^- \pi^0 \nu_\tau) = (479 \pm 24). \tag{5.30}$$

The inputs to the efficiency equation

$$\varepsilon_{\pi^0} = \frac{Y_n\left(\tau^- \to \pi^- \pi^0 \nu_\tau\right)}{Y_d\left(\tau^- \to \pi^- \nu_\tau\right)} \left(\frac{\mathcal{B}(\tau^- \to \pi^- \nu_\tau)}{\mathcal{B}(\tau^- \to \pi^- \pi^0 \nu_\tau) \cdot \mathcal{B}(\pi^0 \to \gamma\gamma)}\right) \left(\frac{\varepsilon_d^\gamma \cdot \varepsilon_d^{track}}{\varepsilon_n^\gamma \cdot \varepsilon_n^{track}}\right), \tag{5.31}$$

are

- $Y_n(\tau^- \to \pi^- \pi^0 \nu_\tau) = (479 \pm 24)$;

- $Y_d(\tau^- \to \pi^- \nu_\tau) = (682 \pm 26)$;

- $\frac{\mathcal{B}(\tau^- \to \pi^- \nu_\tau)}{\mathcal{B}(\tau^- \to \pi^- \pi^0 \nu_\tau) \cdot \mathcal{B}(\pi^0 \to \gamma\gamma)} = (0.430 \pm 0.003)$;

- $\varepsilon_n^\gamma = (24.86 \pm 0.23)\%$;

- $\varepsilon_d^\gamma = (23.56 \pm 0.37)\%$;

- $\varepsilon_n^{track} = (10.81 \pm 0.33)\%$;

- $\varepsilon_d^{track} = (16.51 \pm 0.66)\%$;
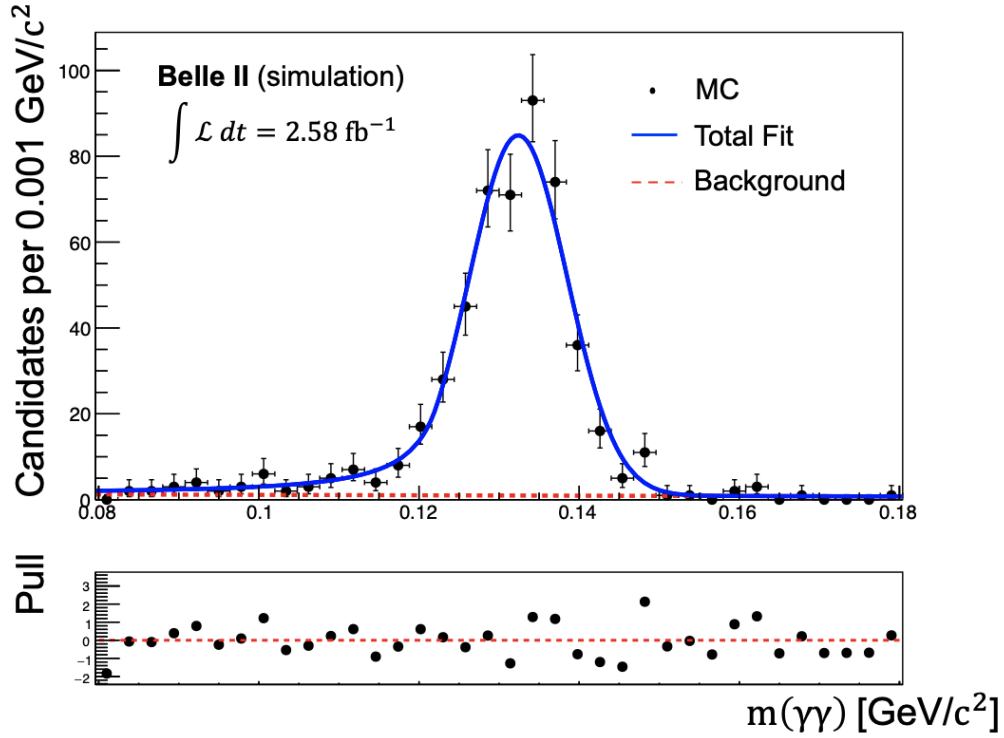
Figure 5.16: (Above): Diphoton mass distribution for simulated numerator events with fit overlaid. Simulated data are shown in black, the total fit is shown in blue and the background fit is shown as a dashed red line. The integrated luminosity corresponds to $\int \mathcal{L} \, dt = 2.58$ fb^{-1}. (Bottom): difference between observed and predicted values, divided by the standard deviation of the observed values.

- purity correction 9%.

The resulting estimate of the π^0 meson reconstruction efficiency is

$$\varepsilon_{\pi^0} = (48.1 \pm 4.0)\% \tag{5.32}$$

where the associated uncertainty is statistical and resulting from standard uncertainty propagation. The result is compatible with the expected value of 50%.

This result, combined with that achieved for the 40% efficiency, provides validation and significant evidence of the reliability of the method applied in two different working points. The two estimates are encouraging and suggest that the approach is conceptually correct. However, these results are obtained in a simplified background configuration and need further refinement to be applicable in real data.

Chapter 6

Determination of efficiency in a realistic simulated sample

In this chapter, I discuss the extension of the analysis to a more realistic scenario. I use a sample that simulates more faithfully an e^+e^- collision and consolidates the demonstration of feasibility of our approach.

6.1 Introduction

In the previous chapter, I demonstrate the feasibility to our estimate of the π^0 reconstruction efficiency in a simplified scenario based on a sample of τ lepton pairs only. However, as shown by figure 4.1, this sample represents only a small and unrepresentative fraction of the overall set of processes that occur during an e^+e^- collision. In order to test the soundness of our approach on experimental data, it is first necessary to extend the analysis to a simulated sample that is as much realistic possible.

Table 4.2 lists all processes included in the full Monte Carlo sample. The amount of data available for analysis corresponds to an integrated luminosity of $\int \mathcal{L}\,dt \approx 1.5$ ab^{-1}. For notation convenience, the processes $e^+e^- \to B^0\overline{B}^0$ and $e^+e^- \to B^+\overline{B}^-$ are unified under the generic term $e^+e^- \to B\overline{B}$. Similarly, the processes $e^+e^- \to u\overline{u}$, $e^+e^- \to d\overline{d}$, $e^+e^- \to s\overline{s}$, and $e^+e^- \to c\overline{c}$ are grouped together as $e^+e^- \to q\overline{q}$.

At this preliminary stage, I use only about 0.5% of the total available simulated data, corresponding to an integrated luminosity of $\int \mathcal{L}\,dt \approx 7.45$ fb^{-1}, keeping the proportions of the various contributions unchanged. This significantly increases the speed of our analysis and does not spoil the validity of results. The remaining 99.5% of the sample could be used once the final configuration of the analysis is defined.

6.2 Initial sample composition

In e^+e^- collisions at the $\Upsilon(4S)$ center-of-mass energy, the number of Bhabha events is orders of magnitude higher than that of the other processes (figure 4.1). In addition, other large background sources contribute to the so-called low multiplicity processes, i.e., $\mu^+\mu^-$, $e^+e^-\mu^+\mu^-$, $e^+e^-e^+e^-$, and generic processes referred to as $\ell^+\ell^-X^+X^-$, which altogether constitute more than 99% of the initial reconstructed sample. The contributions from $q\overline{q}$, $B\overline{B}$, h^+h^-ISR (hadron-hadron pairs originating from initial state radiation) and $\gamma\gamma$ are reasonably small thanks to the restriction imposed of only two tracks per event.

Process	Number of events	Fraction
$e^+e^- \to \tau^+\tau^-$	368762	0.091%
$e^+e^- \to q\,\bar{q}$	18817	0.0047%
$e^+e^- \to B\,\overline{B}$	369	0.000091%
$e^+e^- \to \mu^+\mu^-$	1092022	0.27%
$e^+e^- \to e^+e^-\mu^+\mu^-$	6041746	1.50%
$e^+e^- \to e^+e^-e^+e^-$	8833557	2.19%
$e^+e^- \to \ell^+\ell^-X^+X^-$	288542	0.071%
$e^+e^- \to h^+h^-$	1042	0.00026%
$e^+e^- \to e^+e^-$	386946885	95.87%
$e^+e^- \to \gamma\gamma$	1578	0.00039%

Table 6.1: Composition of the full simulated sample after just offline reconstruction.
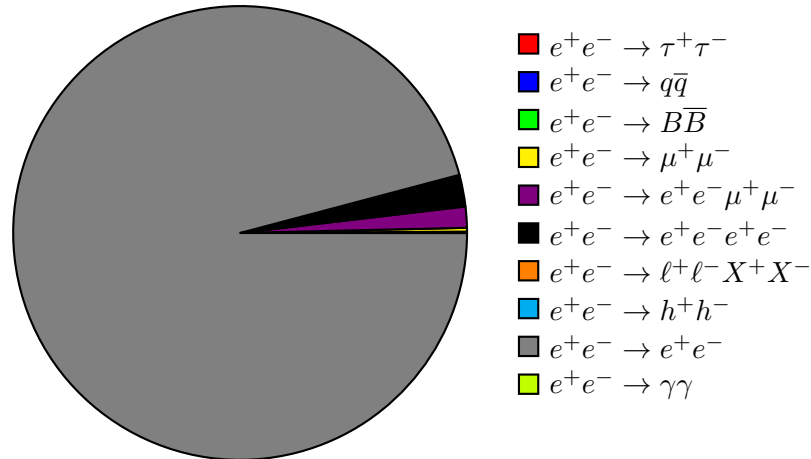
Figure 6.1: Pie chart of the composition of the full simulated sample after just offline reconstruction.

6.3 Trigger selection

In order to use the realistically simulated sample in collision-like conditions, I take into account the effect of trigger selections, which are present in data.

The trigger selection adopted here is a combination of drift-chamber based or calorimeter-based triggers commonly employed in τ physics at Belle II, which is particularly efficient in extracting events with 1prong×1prong topology, as in our case. The following is the combination of level-1 triggers used

$$(\textbf{lml0} \text{ or } \textbf{lml1} \text{ or } \textbf{lml2} \text{ or } \textbf{lml4} \text{ or } \textbf{lml6} \text{ or } \textbf{lml7} \text{ or } \textbf{lml8} \text{ or } \textbf{lml9} \text{ or } \textbf{lml10}) \text{ and } \textbf{ffo}, \quad (6.1)$$

where the meaning of each string is outlined in the following for ECL triggers,

- **lml0**: number of ECL clusters > 2 with $12.4° < \theta < 154.7°$ (full ECL), at least one with $E_{lab} > 0.3$ GeV and event inconsistent with an ECL three-dimensional Bhabha;

- **lml1**: number of ECL clusters ≥ 1 with $E_{CM} > 2$ GeV in $32.2° < \theta < 124.6°$ (almost the full ECL coverage);

- **lml2**: number of ECL clusters ≥ 1 with $E_{CM} > 2$ GeV in $18.5° < \theta < 32.2°$ or $124.6° < \theta < 139.3°$ and event inconsistent with an ECL three-dimensional Bhabha;

- **lml4**: number of ECL clusters ≥ 1 with $E_{CM} > 2$ GeV in $\theta < 18.5°$ or $\theta > 139.3°$ and event inconsistent with an ECL three-dimensional Bhabha;

- **lml6**: number of ECL clusters $= 1$ with $E_{CM} > 1$ GeV in $32.2° < \theta < 128.7°$ (full ECL barrel) and no other cluster with $E_{lab} > 0.3$ GeV;

- **lml7**: number of ECL clusters $= 1$ with $E_{CM} > 1$ GeV in $18.5° < \theta < 31.9°$ or $128.7° < \theta < 139.3°$ and no other cluster with $E_{lab} > 0.3$ GeV;

- **lml8**: two clusters with $170 < \Delta\phi_{CM} < 190$ deg., both with $E_{lab} > 0.25$ GeV, and no cluster with $E_{lab} > 2$ GeV;

- **lml9**: two clusters with $170 < \Delta\phi_{CM} < 190$ deg., $E_{lab}^{low} < 0.25$ GeV, $E_{lab}^{high} > 0.25$ GeV, and no cluster with $E_{lab} > 2$ GeV;

- **lml10**: two clusters with $160 < \Delta\phi_{CM} < 200$ deg., and $160 < \sum\theta_{CM} < 200$ deg., no cluster with $E_{lab} > 2$ GeV;

and for CDC trigger,

- **ffo**: two or more two-dimensional tracks and opening angle of two two-dimensional tracks, $\Delta\phi > 90$ deg., and event inconsistent with an ECL three-dimensional Bhabha and SuperKEKB Injection veto.

where E_{CM} is the cluster energy in the center of mass frame; E_{lab} is that in the laboratory frame; θ is the polar angle of the ECL cluster in the laboratory frame; θ_{CM} is that in the center of mass frame; $\Delta\phi_{CM}$ is the difference in azimuthal angle between two ECL clusters in the center of mass frame; E_{lab}^{low} is the lowest cluster energy between two clusters in the laboratory frame; E_{lab}^{high} is the highest cluster energy between two clusters in the laboratory frame; $\sum\theta_{CM}$ is the sum of the polar angle of two clusters in the center of mass frame; ECL three-dimensional Bhabha is defined as two high energy clusters back to back in θ and ϕ in the center of mass frame with $160 < \sum\theta_{CM} < 190$ deg. and $160 < \Delta\phi_{CM} < 200$ deg. and c.m. energy greater than 3 GeV and 4.5 GeV. The SuperKEKB Injection veto is a signal that inhibits data acquisition if machine operators are injecting beams into SuperKEKB.

From now on, when I refer to *trigger selections*, I mean the combination of selections given in equation 6.1.

Table 6.2 reports the sample composition after applying the triggers selections.

A comparison of the tables 6.1 and 6.2 shows that triggers have already a significant impact. There is an enrichment in τ-pair events, which increase from 0.091% to 1.18%. On average, all background contributions are reduced, particularly the major backgrounds due to e^+e^- events (reduced from 95.87% to 92.54%), $e^+e^-e^+e^-$ events (reduced from 2.19% to 1.36%), $e^+e^-\mu^+\mu^-$ (from 1.50% to 0.52%), $\ell^+\ell^-X^+X^-$ (from 0.071% to 0.057%) and $\gamma\gamma$ (from 0.00039% to 0.0002%). The only contributions that is comparatively more abundant after trigger selection are $\mu^+\mu^-$ events (from 0.27% to 4.30%), $q\bar{q}$ (from 0.0047%

to 0.47%), $B\overline{B}$ (from 0.000091% to 0.001%). The contribution of h^+h^- events remains
almost constant (0.0003%).

After trigger and reconstruction, the main contributions to the sample are the backgrounds consisting of e^+e^- (92.54%), $\mu^+\mu^-$ (4.30%), $e^+e^-e^+e^-$ (1.36%), $e^+e^-\mu^+\mu^-$ (0.52%)
and τ-pair events (1.18%). All other contributions, are already at the subpercent level and
are neglected.

Process	Number of events	Fraction
$e^+e^- \to \tau^+\tau^-$	180952	1.18%
$e^+e^- \to q\overline{q}$	7141	0.047%
$e^+e^- \to B\overline{B}$	206	0.001%
$e^+e^- \to \mu^+\mu^-$	657542	4.30%
$e^+e^- \to e^+e^-\mu^+\mu^-$	79129	0.52%
$e^+e^- \to e^+e^-e^+e^-$	208368	1.36%
$e^+e^- \to \ell^+\ell^- X^+X^-$	8746	0.057%
$e^+e^- \to h^+h^-$	45	0.0003%
$e^+e^- \to e^+e^-$	14162952	92.54%
$e^+e^- \to \gamma\gamma$	34	0.0002%

Table 6.2: Composition of the realistically simulated full sample after trigger selections.
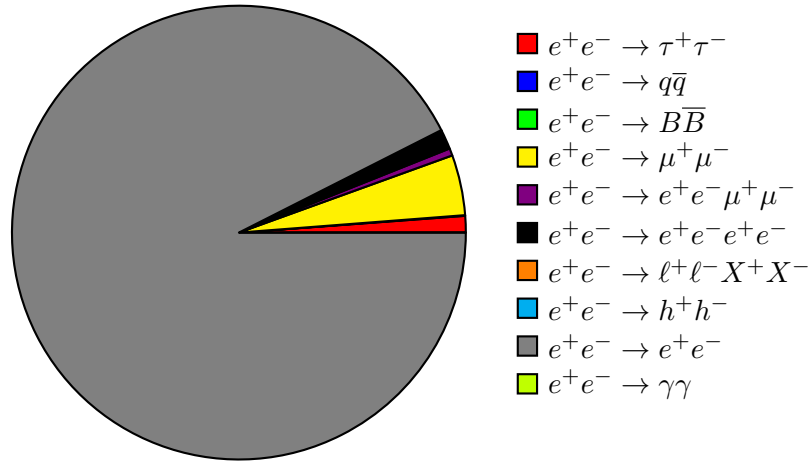
Figure 6.2: Pie chart of composition of the realistically simulated full sample after trigger
selections.

In the next section I use the resulting sample to identify a configuration of selections
on the discriminant observables, with the goal of extracting a pure sample of τ-pair events,
even in the presence of the background represented by Bhabha events generalizing what
done in chapter 5.

6.4   Selections on realistic simulation

To generalize the optimization discussed in section 5.4 to a realistic Monte Carlo sample, I consider only the contributions of background processes that are of the same order of magnitude as the signal. $B\overline{B}$, $q\overline{q}$, h^+h^-, $\gamma\gamma$ and $\ell^+\ell^-X^+X^-$ contributions are neglected.

I identify a set of criteria to apply to the discriminating observables, aiming to minimize the contribution of Bhabha events and obtain the purest possible τ-pair sample as follows:

- I construct normalized histograms of all relevant contributions to the observable under consideration, to visually identify shape differences that can offer discriminating power;

- I isolate the contribution of the τ-pair signal (shown in red), and compare it with contributions of the main background processes, e^+e^- (gray), $e^+e^-e^+e^-$ (green), $e^+e^-\mu^+\mu^-$ (magenta), and $\mu^+\mu^-$ (blue);

- I define qualitatively selections for each observable by restricting the sample to the domain where the contribution of the τ-pair signal seems enhanced over the backgrounds;

This empirical procedure does not consider all background contributions simultaneously thereby not representing a global optimization of selections. However, it provides a first-order estimate consistent with our initial exploratory approach. Based on the results, I will evaluate whether it will be necessary to implement further optimization.

I use thrust as one discriminating observable (see section 4.4). Figure 6.3 (top panel) shows the thrust distribution for the various relevant contributions. As expected, the distribution of $\mu^+\mu^-$ events (in blue) and e^+e^- events (in gray) are biased toward higher thrust values than τ pair production. The selection applied, $0.915 < \text{thrust} < 0.98$, is indicated by the orange dashed vertical lines and isolates a range where signal is relatively more prominent.

Then, I consider the visible energy in the center of mass. I expect it to be particularly discriminating between $\tau^+\tau^-$ events and Bhabha or muon-pair-producing events. Because τ-pairs decay producing at least two neutrinos, a selection on visible energy also discriminates against $e^+e^-e^+e^-$, and $e^+e^-\mu^+\mu^-$ events. Figure 6.3 (bottom panel) shows the visible energy in the collision's center of mass distribution for the various relevant contributions. The distribution of $e^+e^-e^+e^-$ events (green), $e^+e^-\mu^+\mu^-$ events (magenta) is centered on lower visible energy values than the τ pair production events. On the other hand, the distribution of e^+e^- events (gray) and $\mu^+\mu^-$ events (blue) is centered on higher visible energy values allowing effective discrimination against signal events. The chosen selection is enclosed by the orange dashed vertical lines, $2.95 < \text{visible energy} < 7.45$ GeV.

It is likeliy that one or more particles in four-body events may exit the detector's acceptance region leading to a significant loss of visible energy. A selection based on this variable is therefore expected to allow effective isolation of τ-pair production events, significantly reducing the contribution of all background processes previously mentioned.

In addition to selecting on thrust and visible energy, I also revisit selections on the observables discussed in the previous chapter: the particle identification of the pion associated with the track in the signal hemisphere of the event, and E/p.

Figure 6.4 shows distributions of these observables for the various relevant contributions. I take advantage of the differences among distributions of the various components to restrict the analysis sample to a region of pion identification > 0.54 and $0.07 < \text{E/p} < 0.69\ c$ in which the contribution of $\tau^+\tau^-$ events is enhanced.
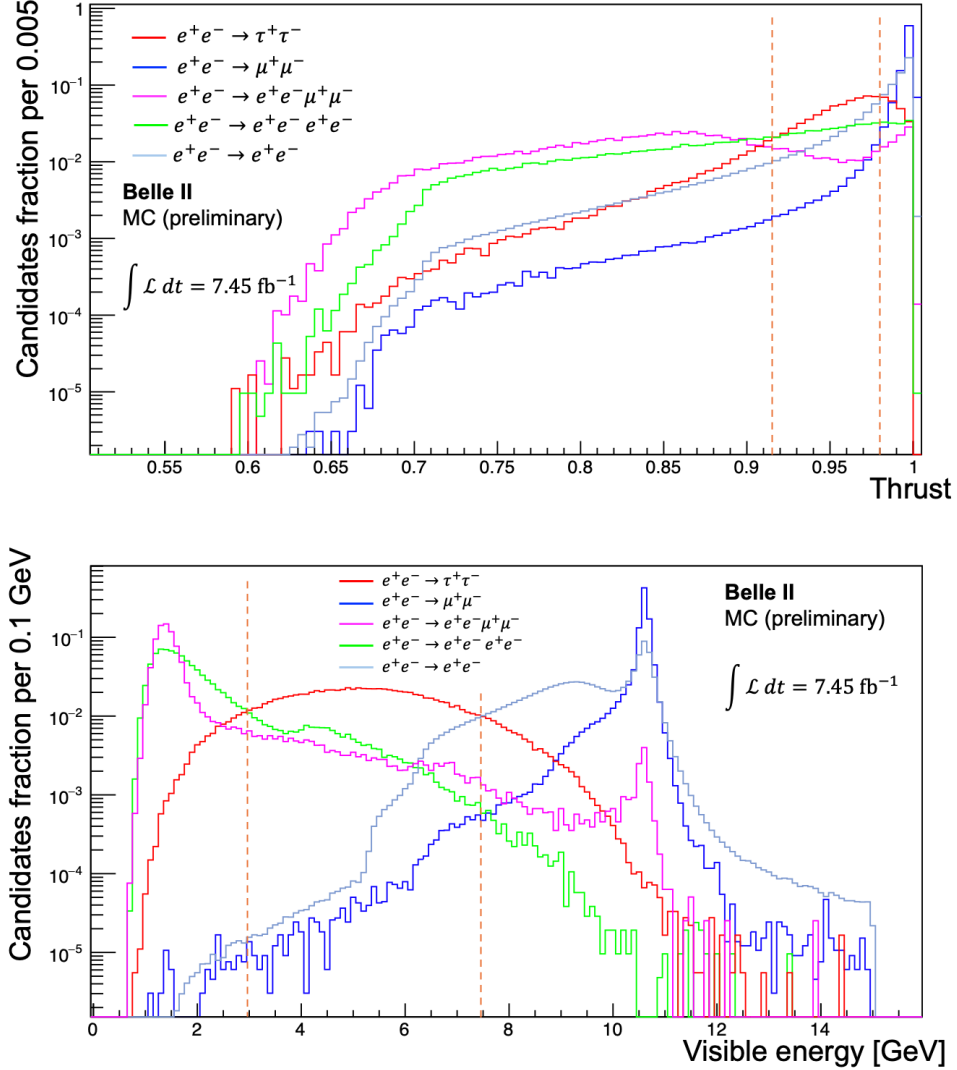
Figure 6.3: (Top panel): distribution of event thrust for simulated $\tau^+\tau^-$ events (red) and relevant background contributions, e^+e^- (gray), $e^+e^-e^+e^-$ (green), $e^+e^-\mu^+\mu^-$ (magenta), $\mu^+\mu^-$ (blue). (Bottom panel): distribution of visible energy in the center of mass for the same components. The orange dashed lines enclose the signal selections. All histograms are normalized to unit area. The integrated luminosity corresponds to $\int \mathcal{L}\,dt = 7.45$ fb^{-1}.

In order to further reduce the contribution of Bhabha events, I perform an additional selection on the momentum of the charged particle in the tag hemisphere $p_{track\,tag}$. I focus on the tag hemisphere in order not to bias the signal charged-particle momentum which could then restrict excessively the π^0 momentum range.

In fact, while in τ decays the τ momentum gets distributed among multiple decay products, including a charged particle (e.g., a pion or muon) that may have a relatively lower momentum, in Bhabha events the electrons and positrons are directly produced in the collision and tend to have high momentum.

Figure 6.5 shows the momentum of the tag charged particle $p_{track\,tag}$ for various relevant components. The distributions of e^+e^- events (gray) and $\mu^+\mu^-$ events (blue) are centered
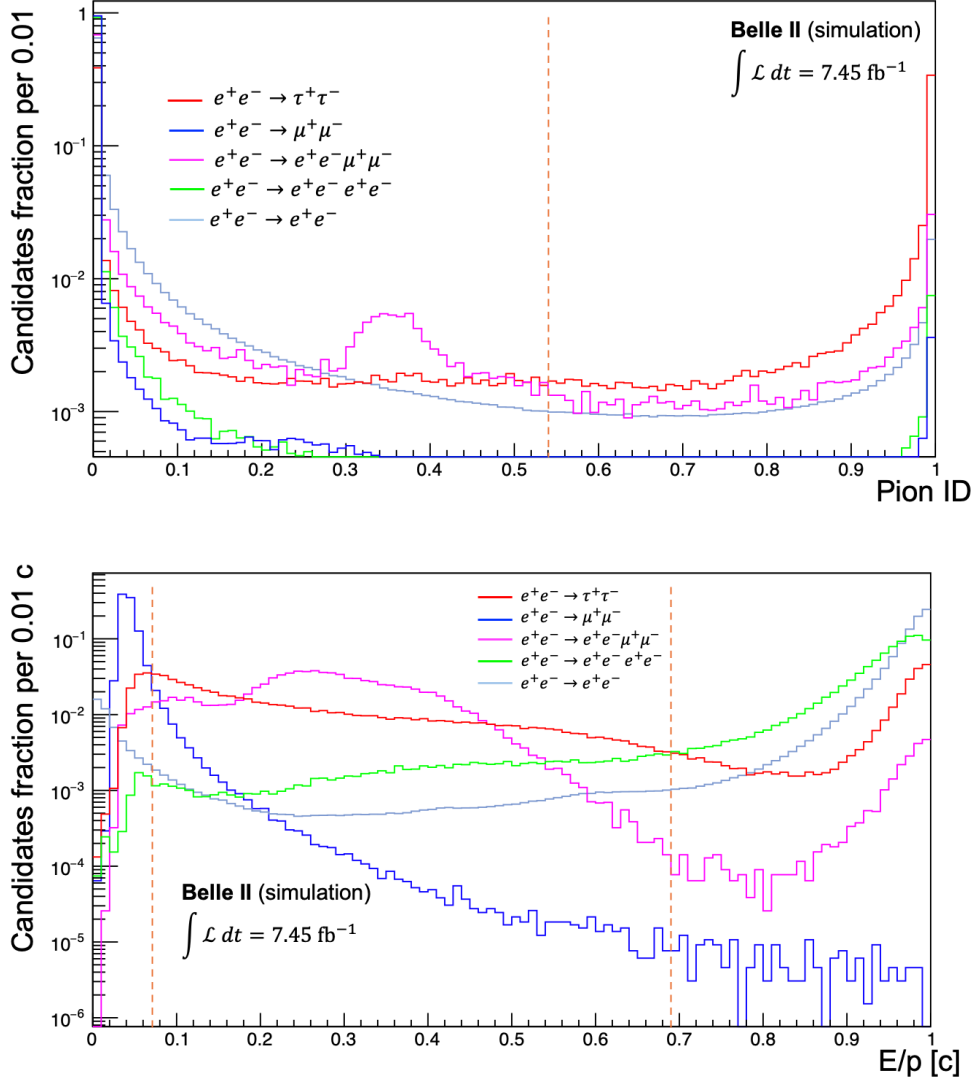
Figure 6.4: (Top panel): distribution of pion identification for the signal track in $\tau^+\tau^-$ events (red) and relevant backgrounds, e^+e^- (gray), $e^+e^-e^+e^-$ (green), $e^+e^-\mu^+\mu^-$ (magenta), $\mu^+\mu^-$ (blue). The orange dashed line correspond to the signal selection. (Bottom panel): distribution of E/p for the same categories. The orange dashed lines enclose the signal selections. All histograms are normalized to unit area. The integrated luminosity corresponds to $\int \mathcal{L}\, dt = 7.45$ fb^{-1}.

on higher momentum values than the τ pair production events (red). The selection applied is indicated by the orange dashed vertical line and is $p_{track\,tag} < 3.15$ GeV/c.

From now on, when I refer to $low-multiplicity\,selections\,(LM)$, I mean the combination of selections described in this paragraph.

The full sample composition resulting from all previous low-multiplicity selections is in table 6.3.
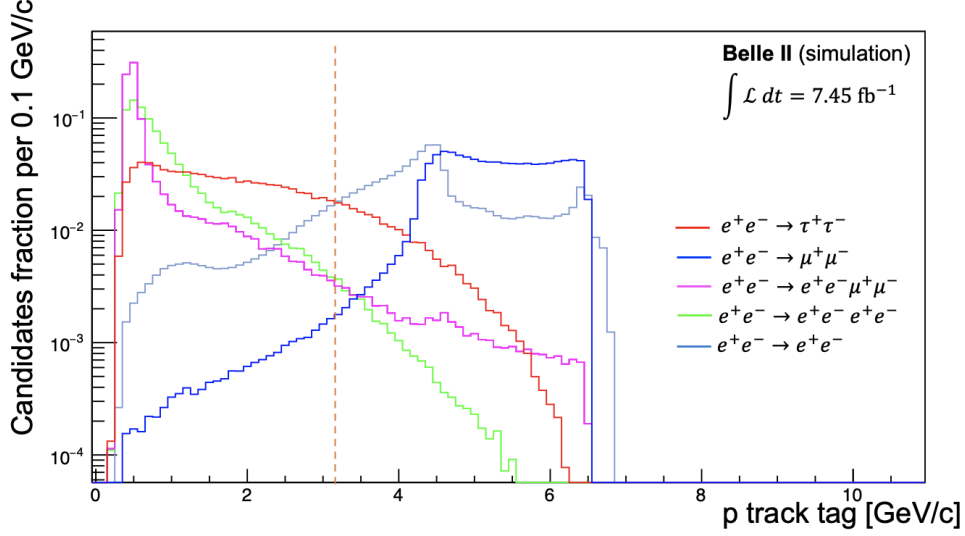
Figure 6.5: Distribution of $p_{track\,tag}$ for the tag track in $\tau^+\tau^-$ events (red) and relevant backgrounds, e^+e^- (gray), $e^+e^-e^+e^-$ (green), $e^+e^-\mu^+\mu^-$ (magenta), $\mu^+\mu^-$ (blue). The orange dashed line correspond to the signal selection. All histograms are normalized to unit area. The integrated luminosity corresponds to $\int \mathcal{L}\,dt = 7.45$ fb^{-1}.

Process	Number of events	Fraction
$e^+e^- \to \tau^+\tau^-$	35853	96.56%
$e^+e^- \to q\bar{q}$	170	0.46%
$e^+e^- \to B\overline{B}$	0	–
$e^+e^- \to \mu^+\mu^-$	2	0.005%
$e^+e^- \to e^+e^-\mu^+\mu^-$	55	0.15%
$e^+e^- \to e^+e^-e^+e^-$	52	0.14%
$e^+e^- \to \ell^+\ell^- X^+ X^-$	105	0.28%
$e^+e^- \to h^+h^-$	0	–
$e^+e^- \to e^+e^-$	892	2.40%
$e^+e^- \to \gamma\gamma$	0	–

Table 6.3: Composition of the realistic simulated full sample after all selections.

The result is interesting: with a realistic sample composition, I obtain a τ pair purity of about 97%, demonstrating that the method used for efficiency estimation should remain valid even when considering realistic data.

Due to the high purity achieved I do not proceed with further optimization, assuming that any improvement in signal purity due to optimization would be negligible when compared to the major gain already achieved.
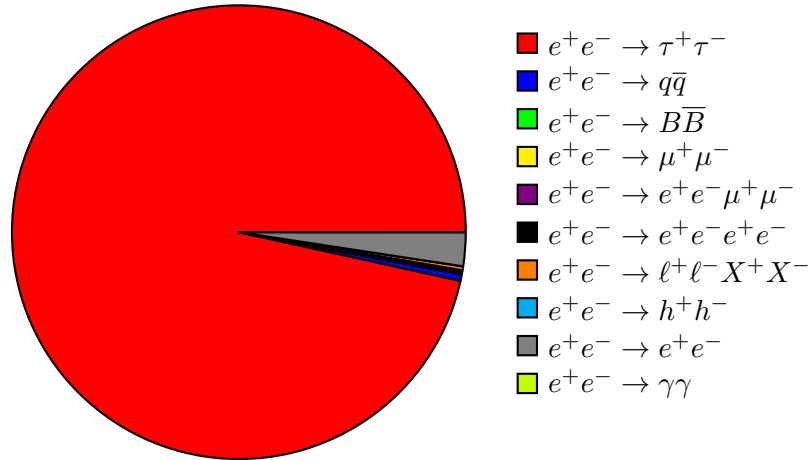
Figure 6.6: Pie chart of the composition of the realistic simulated full sample after all
selections.

6.5 Optimized $\tau^+\tau^-$ selections

To validate the analysis as developed in realistic simulation, it is important to compare the
resulting π^0 efficiency with a known reference.

The only difference between the study of the τ-pair-only sample of chapter 5 and the
realistic sample is the application of a combination of trigger selection and selections on
further discriminanting observables.

However, since the full Monte Carlo sample is also subjected to low-multiplicity selec-
tions that may affect the distributions of the discriminanting observables used in chapter
5, the optimized selections found previously may not be optimal for this realistic dataset.
In order to assess the impact of low-multiplicity selections, I first assess the sample com-
position of the fully simulated sample selected through optimized selections of chapter 5
($\tau\tau$ $selections$ from now on).

Tables 6.4 shows the results. The dominant background processes are a numerator con-
tamination (about 4.5%), $\tau^- \to \mu^- \bar{\nu}_\mu \nu_\tau$ (about 7%) caused by misidentification between
muon and pion and by Bhabha processes (about 6%). The denominator signal achieves a
purity of about 79%. This purity is insufficient for a reliable estimate of the π^0 reconstruc-
tion efficiency. Therefore, I re-optimize the signal purity at the denominator to identify a
new configuration of selections possibly optimal for this generic sample ($final$ $selections$
from now on).

I therefore perform a dedicated selection optimization using the same approach de-
scribed in paragraph 5.4. Figure 6.7 shows the resulting figure of merit as a function of
the criteria combination.

The absolute maximum of the purity is derived from the configuration of selections that
corresponds to

- πID > 0.84;

- E/p < 0.0815 c.

The resulting sample composition is shown in tables 6.5 and 6.6. The denominator signal
fraction has increased to about 84.44% with 114 signal events remaining.

| | | Denominator |
Generation	Number of events	Fraction
$\tau^- \to \pi^- \nu_\tau$	248	$(78.98 \pm 2.30)\%$
$\tau^- \to \pi^- \pi^0 \nu_\tau$	14	$(4.46 \pm 1.16)\%$
$\tau^- \to \mu^- \overline{\nu}_\mu \nu_\tau$	22	$(7.01 \pm 1.44)\%$
$e^+e^- \to e^+e^- \mu^+\mu^-$	3	$(0.96 \pm 0.55)\%$
$e^+e^- \to e^+e^- e^+e^-$	1	$(0.32 \pm 0.32)\%$
$e^+e^- \to \ell^+\ell^- X^+X^-$	3	$(0.96 \pm 0.96)\%$
$e^+e^- \to e^+e^-$	20	$(6.37 \pm 1.38)\%$

Table 6.4: Denominator composition resulting from the application of the optimization of
chapter 5 ($\tau\tau$ selections) to the fully simulated sample. Only processes showing a non zero
yield are included. The associated uncertainty is statistical and is calculated assuming a
binomial distribution.
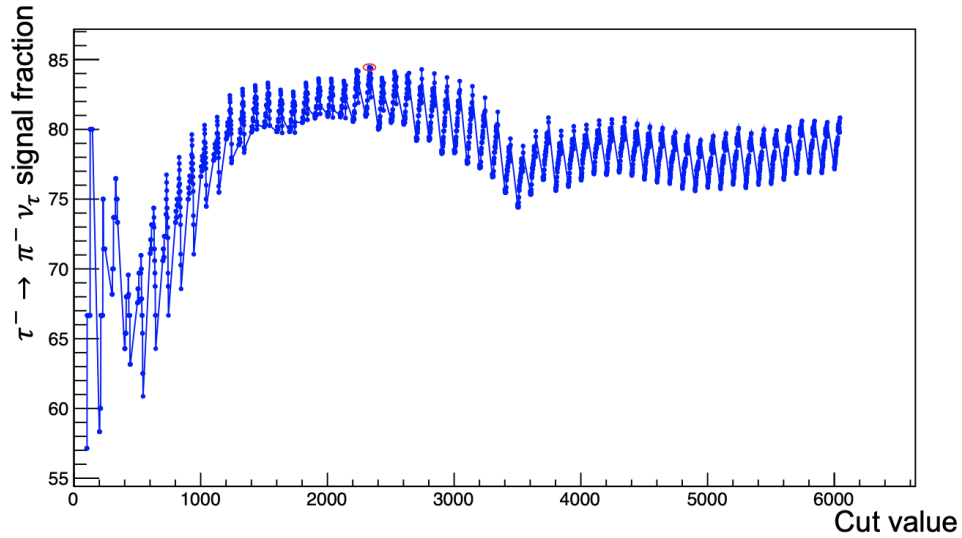
Figure 6.7: Purity as a function of selection. The absolute maximum is highlighted by a
red circle.

| | | Denominator |
Generation	Number of events	Fraction
$\tau^- \to \pi^- \nu_\tau$	114	$(84.44 \pm 3.12)\%$
$\tau^- \to \pi^- \pi^0 \nu_\tau$	2	$(1.48 \pm 1.04)\%$
$\tau^- \to K^- \nu_\tau$	1	$(0.74 \pm 0.74)\%$
$\tau^- \to \mu^- \overline{\nu}_\mu \nu_\tau$	4	$(2.96 \pm 1.46)\%$
$e^+e^- \to e^+e^- \mu^+\mu^-$	1	$(0.74 \pm 0.74)\%$
$e^+e^- \to e^+e^- e^+e^-$	1	$(0.74 \pm 0.74)\%$
$e^+e^- \to e^+e^-$	10	$(7.41 \pm 2.25)\%$

Table 6.5: Denominator composition resulting from re-optimization of the realistically
simulated sample (final selections). Only processes showing a non zero yield are included.
The associated uncertainty is statistical and is calculated assuming a binomial distribution.
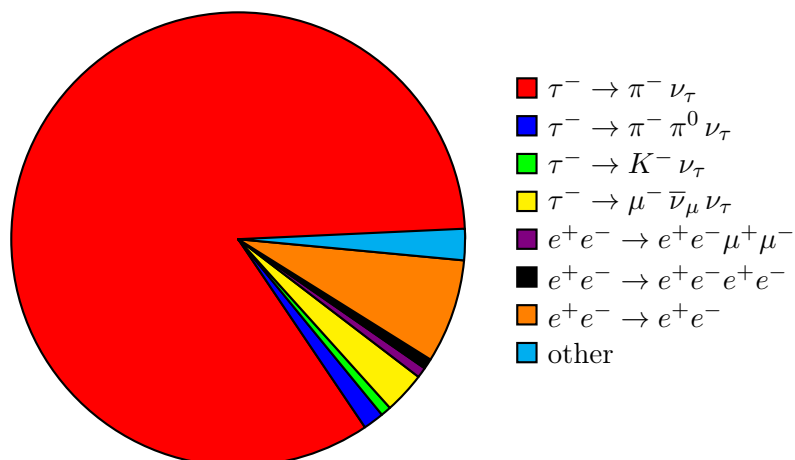
Figure 6.8: Pie chart of the re-optimized denominator composition on the realistic sample
(see table 6.5).

| | | Numerator |
Generation	Number of events	Fraction
$\tau^- \to \pi^- \nu_\tau$	45	$(11.03 \pm 1.55)\%$
$\tau^- \to \pi^- \pi^0 \nu_\tau$	338	$(82.84 \pm 1.87)\%$
$\tau^- \to \pi^- 2\pi^0 \nu_\tau$	4	$(0.98 \pm 0.49)\%$
$\tau^- \to K^- \nu_\tau$	1	$(0.25 \pm 0.24)\%$
$\tau^- \to \mu^- \overline{\nu}_\mu \nu_\tau$	2	$(0.49 \pm 0.35)\%$
$e^+e^- \to \ell^+\ell^- X^+ X^-$	2	$(0.49 \pm 0.35)\%$
$e^+e^- \to e^+e^-$	10	$(2.45 \pm 0.77)\%$

Table 6.6: Numerator composition resulting from re-optimization of the realistically simu-
lated sample (final selection). Only processes showing a non zero yield are included. The
associated uncertainty is statistical and is calculated assuming a binomial distribution.

Table 6.5 shows the resulting denominator sample composition. The main contribution
to the background are Bhabha events, which remain prevalent even after optimization,
accounting for about 7% of the total. About 3% of the total is attributed to $\tau^- \to \mu^- \overline{\nu}_\mu \nu_\tau$
decays, which are a major source of background in the sample of only-τ-pair events. In
addition, a contribution of about 1.5% comes from the numerator.

Table 6.6 shows the numerator sample composition. The signal purity at the numerator
is about 83%. The main contribution to the background comes from a denominator con-
tamination, which accounts for almost 11% of the total. This contribution is statistically
subtracted in the diphoton mass fit, so there is no pressing need to reduce it further. In
addition, a background contribution of about 2% is due to Bhabha events. The remaining
contributions are subpercent.

Comparing the tables 6.4 and 6.5 shows that the updated optimization results in an
absolute gain of about 5% in the purity of the signal at the denominator. This reflects the
differences between the realistic Monte Carlo sample and the τ-pair exclusive sample. The
introduction of additional background components in the realistic Monte Carlo generates
bias in the distributions, which spoils optimality. Howerver, an 84% purity can preliminarly
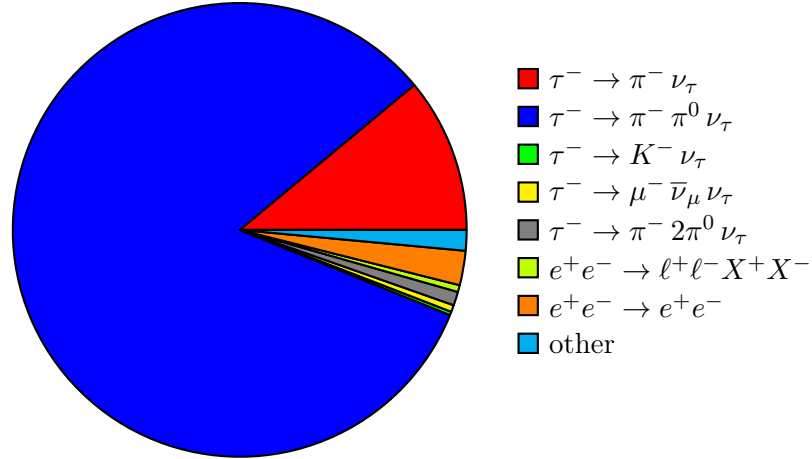
Figure 6.9: Pie chart of the re-optimized numerator composition on the realistic sample
(see table 6.6).

be considered sufficient for our objective. As in chapter 5, I proceed to estimate the
correction factors to be included in the π^0 reconstruction efficiency formula.

6.6   Corrective terms to the efficiency formula

Similarly to chapter 5, needed corrective terms are determined from simulation.

The efficiency of the low-multiplicity selections used to extract the purest possible τ
pair sample, is evaluated in a similar way as the previous corrective terms and is

$$\varepsilon_d^{LM} = (19.06 \pm 0.52)\,\%, \tag{6.2}$$

for the denominator and

$$\varepsilon_n^{LM} = (33.35 \pm 0.35)\,\% \tag{6.3}$$

for the numerator.

The selection efficiency on photons for the denominator is

$$\varepsilon_d^{\gamma} = (21.73 \pm 0.58)\,\%, \tag{6.4}$$

and for numerator is

$$\varepsilon_n^{\gamma} = (30.74 \pm 0.33)\,\%. \tag{6.5}$$

The efficiency of the final selections for the denominator is

$$\varepsilon_d^{final} = (10.35 \pm 0.92)\,\%, \tag{6.6}$$

and for numerator is

$$\varepsilon_n^{final} = (5.50 \pm 0.29)\,\%, \tag{6.7}$$

where all the associated uncertainties are statistical and calculated assuming a binomial
distribution.

The only missing ingredients for estimating the π^0 reconstruction efficiency with the
realistic Monte Carlo dataset are the signal yields at the numerator ($Y_n(\tau^- \to \pi^- \pi^0 \nu_\tau)$)
and at the denominator ($Y_d(\tau^- \to \pi^- \nu_\tau)$).

6.7 Extraction of the denominator signal yield

Similarly to what done in chapter 5, the denominator signal yield is

$$Y_d(\tau^- \to \pi^- \nu_\tau) = (135 \pm 12), \tag{6.8}$$

where the associated uncertainty is statistical, and assumed to be Poisson.

6.7.1 Correction for denominator impurity

Due to non-purity in the denominator sample, this efficiency needs to be corrected.

Table 6.5 shows that only 114 events out of 135, about 84.4%, are actually signal events generated as $\tau^- \to \pi^- \nu_\tau$. The remaining approximately 16% are background events that meet all the selections and that in our method are erroneously considered as denominator signal events. Hence, I apply this additional 16% correction to π^0 reconstruction efficiency.

6.8 Extraction of the numerator signal yield

I apply to the numerator sample the same standard combination of selections on all photons in the event and invariant mass restriction (see section 5.10).

I perform the usual fit on the π^0 invariant mass and obtain the result shown in figure 6.10. The number of signal events in the fit interval is

$$N_s = (159 \pm 14), \tag{6.9}$$

where the associated uncertainty is purely statistical. The signal yield of the numerator is

$$Y_n(\tau^- \to \pi^- \pi^0 \nu_\tau) = (150 \pm 23), \tag{6.10}$$

after correction for the fit range.

6.9 Final π^0 reconstruction efficiency

At this point, I have all the inputs for calculating the π^0 reconstruction efficiency using the full simulated sample,

- $Y_n(\tau^- \to \pi^- \pi^0 \nu_\tau) = (150 \pm 23)$;

- $Y_d(\tau^- \to \pi^- \nu_\tau) = (135 \pm 12)$;

- $\frac{\mathcal{B}(\tau^- \to \pi^- \nu_\tau)}{\mathcal{B}(\tau^- \to \pi^- \pi^0 \nu_\tau) \cdot \mathcal{B}(\pi^0 \to \gamma\gamma)} = (0.430 \pm 0.003)$;

- $\varepsilon_n^\gamma = (30.74 \pm 0.33)\%$;

- $\varepsilon_d^\gamma = (21.73 \pm 0.58)\%$;

- $\varepsilon_n^{final} = (5.50 \pm 0.29)\%$;

- $\varepsilon_d^{final} = (10.35 \pm 0.92)\%$,

- $\varepsilon_n^{LM} = (33.35 \pm 0.35)\%$;
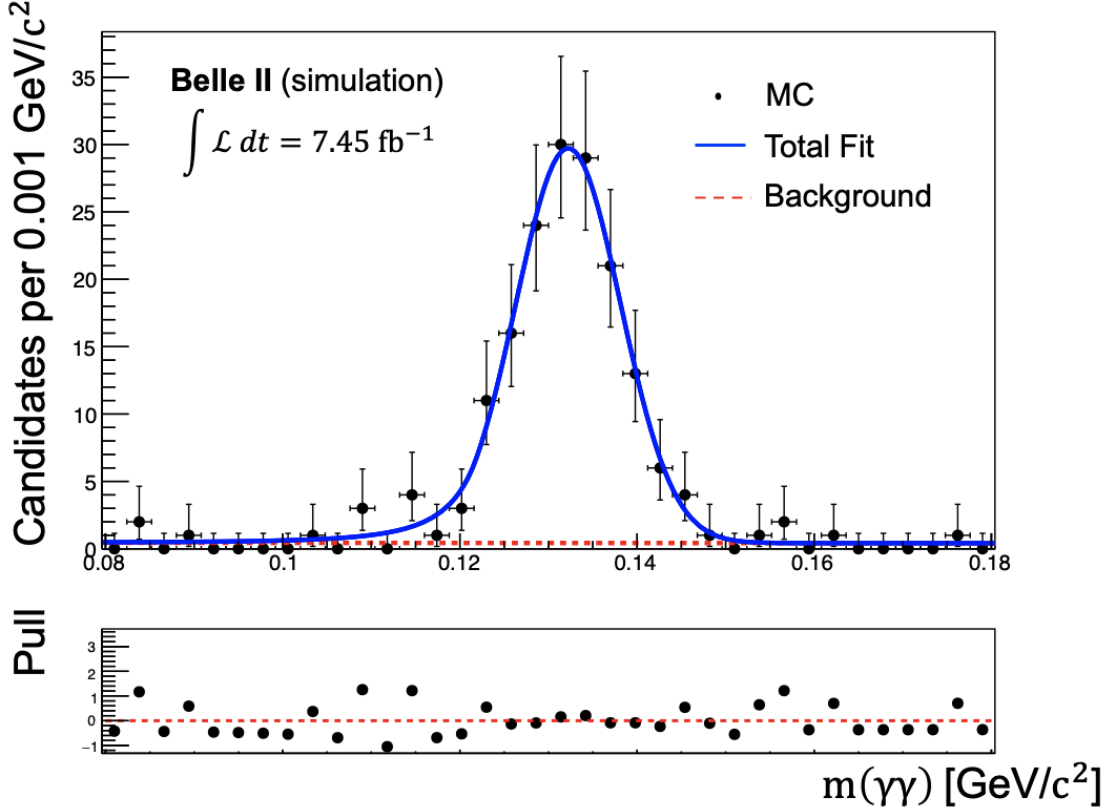
Figure 6.10: (Above): Diphoton mass distribution for simulated numerator events with fit overlaid. Simulated data are shown in black, the total fit is shown in blue and the background fit is shown as a dashed red line. The integrated luminosity corresponds to $\int \mathcal{L}\,dt = 7.45$ fb^{-1}. (Bottom): difference between observed and predicted values, divided by the standard deviation of the observed values.

- $\varepsilon_d^{LM} = (19.06 \pm 0.52)\%$;

- non-purity 16%,

substituting those into the equation defining the π^0 meson reconstruction efficiency

$$\varepsilon_{\pi^0} = \frac{Y_n\left(\tau^- \to \pi^-\,\pi^0\,\nu_\tau\right)}{Y_d\left(\tau^- \to \pi^-\,\nu_\tau\right)} \left(\frac{\mathcal{B}(\tau^- \to \pi^-\,\nu_\tau)}{\mathcal{B}(\tau^- \to \pi^-\,\pi^0\,\nu_\tau)\cdot\mathcal{B}(\pi^0 \to \gamma\,\gamma)}\right)\left(\frac{\varepsilon_d^\gamma\cdot\varepsilon_d^{final}\cdot\varepsilon_d^{LM}}{\varepsilon_n^\gamma\cdot\varepsilon_n^{final}\cdot\varepsilon_n^{LM}}\right),$$

(6.11)

I obtain the final estimate of the π^0 meson reconstruction efficiency in realistic conditions,

$$\varepsilon_{\pi^0} = (43 \pm 9)\%,$$

(6.12)

where the associated uncertainty is statistical and based on standard uncertainty propagation. The result is compatible with the expected value of 40% known from independent studies.

The efficiency exhibits a relative uncertainty of 20%, significantly higher than the sub-percent precision goal our method could theoretically achieve. However, as discussed in

section 5.11 most of it is driven by our choice of using small samples for practical convenience. During the development of the method in a real application, one would use the full samples of simulation and data available at Belle II thus reducing the uncertainty down to the irreducible limit due to branching fractions.

This result supports the reliability of our approach and its promising potential. The fact that the result obtained from a realistic sample remains consistent with the expected outcome provides a convincing validation of the approach. The consistency of these estimates as obtained in varying scenarios of sample composition and selection is remarkable and indicates promising opportunities of applications in real data.

Chapter 7

Toward an application to Belle II data

In this chapter I present preliminary comparisons between experimental data and Monte Carlo simulations for relevant observables, to qualitatively assess the possibility of extending the method to Belle II collision data. The chapter concludes with a concise overview of most relevant systematic uncertainties that might affect the final estimate of the efficiency in a sample of experimental data.

7.1 Introduction

In this thesis work, I thoroughly demonstrated the feasibility of the method in simulated data. The natural next and final step would be to estimate the applicability to experimental data.

In preparation for this, I start with a preliminary, qualitative comparison between relevant distributions in experimental and simulated data to identify any differences that would require dedicated studies before a data application. I study E/p, tag track momentum, pion identification, thrust, and visible energy in the center of mass because these are the observables we use in the selection.

7.2 Data-simulation comparison

Figures 7.1 and 7.2 show the comparison of data and simulation for the observables E/p and the tag particle momentum, respectively after all selections. Here and in any subsequent similar plots, data distributions are normalized to simulated distributions. Good agreement exists for these observables, with no statistically significant signs of mismodeling.

Analyzing in detail the bottom panel in the figure 7.1, a seemingly oscillating structure in the data points as a function of E/p emerges, the origin of which may not be attributable to simple statistical fluctuations. In particular, the presence of sequences of adjacent points (i.e. bin 1-2 and bin 27-28) coherently about two standard deviations away from the simulated distribution suggests a potential, albeit slight, discrepancy in shape between the two distributions. Similarly, the bottom panel in figure 7.2 shows evidence of an increasing monotonic structure in the data-simulation ratio that stabilizes at unity. Again, this behavior is unlikely to be due to statistical fluctuation but rather suggests to a slight discrepancy in the shape of the two distributions.

In both cases, systematic deviations are minimal and therefore not a reason of concern.
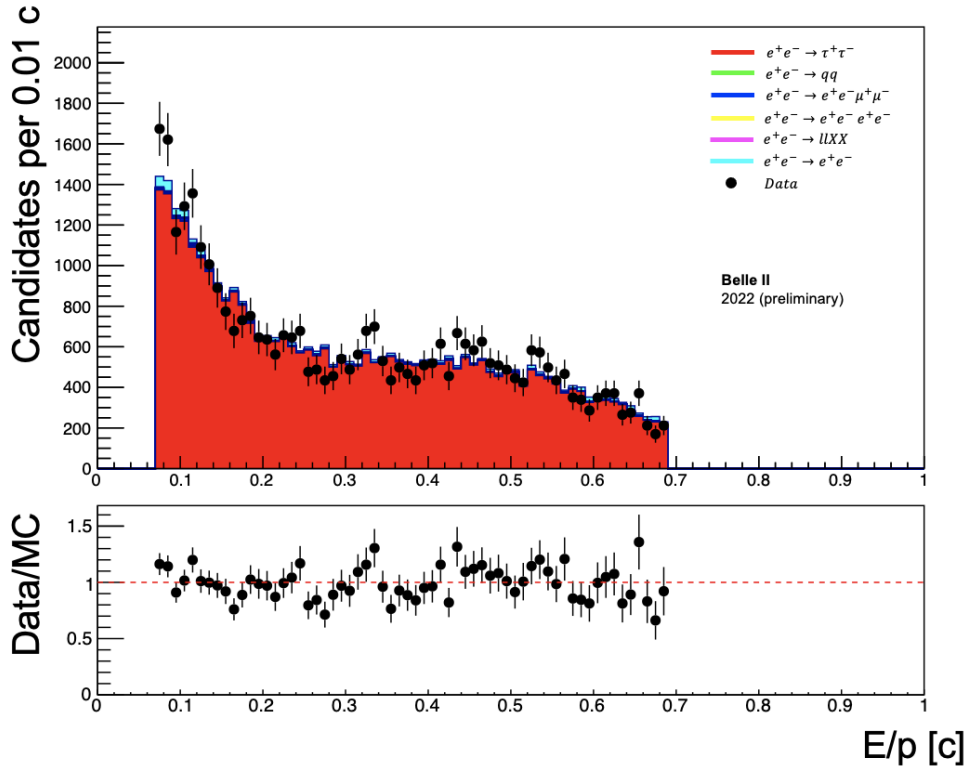
Figure 7.1: (Top panel): data-simulation comparison for the observable E/p after applying all selections. Data (black points) are normalized to the simulated distribution (colored histogram) whose sample size corresponds to $\int \mathcal{L}\,dt = 7.45$ fb^{-1}. (Bottom panel): data-to-simulation ratio.

Figure 7.3 shows the comparison for the pion identification observable, which shows a visible shape discrepancy in the highest pion-identification bin.

This discrepancy is known in Belle II from other studies [69] and could be mitigated by using dedicated centrally produced corrections based on control samples in data that weigh the simulated distribution to mirror data as a function of particle momentum and θ.

Figures 7.4 and 7.5 show the comparison for the visible energy in the center of mass and thrust, respectively. Serious disagreements are observed for these observables, particularly for the thrust. For the visible energy distribution, the shapes of the data and simulation distributions appear to be consistent, except for a major shift of the data distribution toward higher values. For the thrust distribution, the mismodeling is even more pronounced, with shapes that are completely different. This behavior merits further investigation. By studying the data-simulation comparison for thrust after each of the steps in the sequence of selection criteria, I find that the mismodeling primarily occurs after the visible energy selection is applied. Given that visible energy and thrust are correlated as shown in figure 7.6, I study the visible energy to investigate the possible origin of this mismodeling. Figure 7.7 shows the visible energy comparison before any analysis selection. The distribution show large mismodeling and significant shape discrepancies. The position of the peaks in energy is poorly reproduced by the simulation, resulting in large data-to-simulation ratios. Consequently, the significant discrepancy observed in thrust, as illustrated in figure 7.5, is likely attributable to this initial visible energy mismodeling.
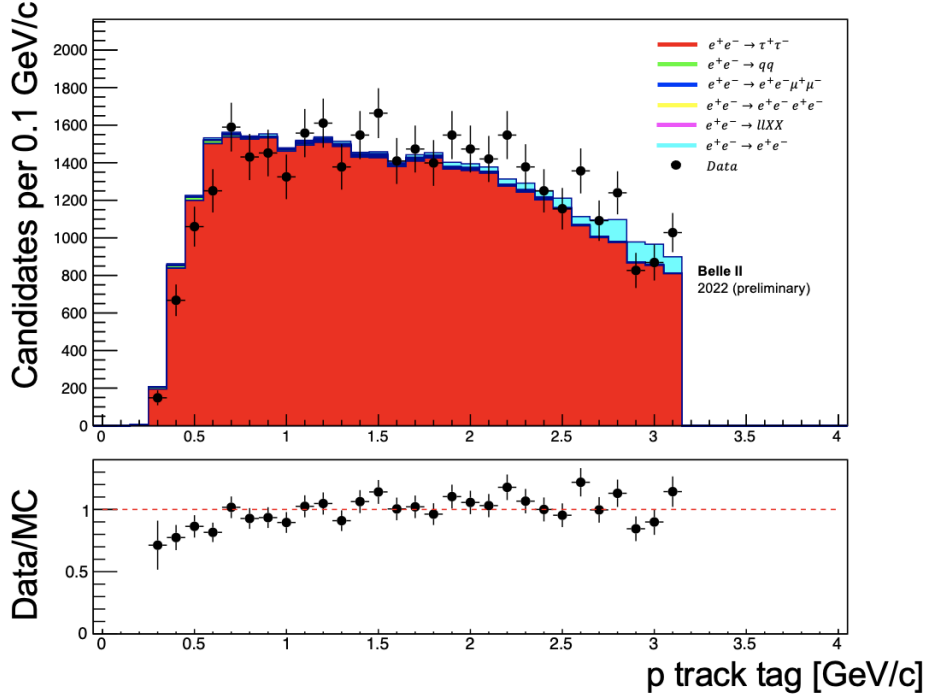
Figure 7.2: (Top panel): data-simulation comparison for the particle's tag momentum after applying all selections. Data (black points) are normalized to the simulated distribution (colored histogram) whose sample size corresponds to $\int \mathcal{L}\, dt = 7.45$ fb^{-1}. (Bottom panel): data-to-simulation ratio.

To fully resolve this discrepancy, a dedicated study of visible energy modeling and its correlation with thrust would be required before applying the analysis to data. Such a study, however, goes beyond the scope of this thesis. In case that such a study would not expose concusively the source of the mismatch, a two-dimensional reweighting in the thrust-visible energy plane would probably be sufficient to apply the method in data.

7.3 Systematic uncertainties

When extending the method to experimental data, it would be necessary to consider a number of sources of systematic uncertainties.

To facilitate understanding, I report below the equation that defines the π^0 meson reconstruction efficiency, along with the relevant correction terms

$$\varepsilon_{\pi^0} = \frac{Y_n\left(\tau^- \to \pi^- \pi^0 \nu_\tau\right)}{Y_d\left(\tau^- \to \pi^- \nu_\tau\right)} \left(\frac{\mathcal{B}(\tau^- \to \pi^- \nu_\tau)}{\mathcal{B}(\tau^- \to \pi^- \pi^0 \nu_\tau) \cdot \mathcal{B}(\pi^0 \to \gamma\,\gamma)}\right) \left(\frac{\varepsilon_d^\gamma \cdot \varepsilon_d^{final} \cdot \varepsilon_d^{LM}}{\varepsilon_n^\gamma \cdot \varepsilon_n^{final} \cdot \varepsilon_n^{LM}}\right), \;(7.1)$$

First, the statistical uncertainties associated with corrective efficiencies, due to the finite size of the simulated samples used to determine them, propagate into the final result as systematic uncertainties.

Other main sources of systematic uncertainty identified in this method include

- *Systematic uncertainty from uncertainties of corrective efficiencies*: throughout this thesis, I describe in detail the corrective terms to be included for estimating the π^0
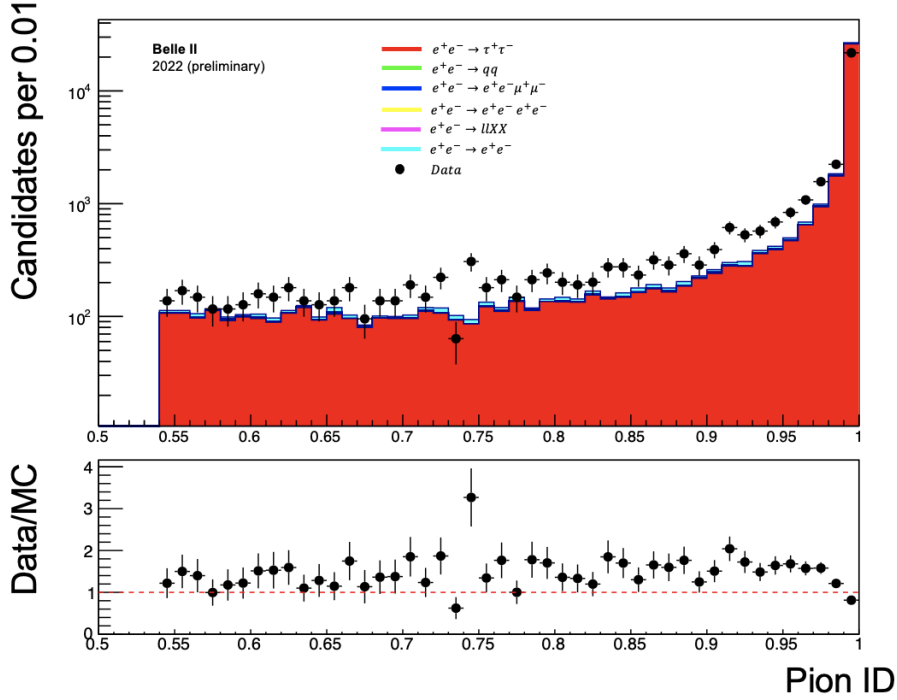
Figure 7.3: (Top panel): data-simulation comparison for the pion identification observable after applying all selections. Data (black points) are normalized to the simulated distribution (colored histogram) whose sample size corresponds to $\int \mathcal{L}\, dt = 7.45$ fb^{-1}. (Bottom panel): data-to-simulation ratio.

meson reconstruction efficiency: the efficiency of selection on photons ε^{γ}, used to separate the numerator sample from the denominator sample; the efficiency of applying the low-multiplicity selections ε^{LM}, used to isolate the purest τ-pair production sample from a generic simulated sample; and the efficiency of the final selections ε^{final}, used to obtain the purest possible sample of signal at the denominator ($\tau^{-} \rightarrow \pi^{-}\, \nu_{\tau}$).

I evaluate these quantities through simulation under the assumption that all discrepancies between numerator and denominator channels are accurately described by Monte Carlo. However, this is likely true only up to a certain accuracy. Consequently, it is necessary to assign a systematic uncertainty to each correction term introduced in the reconstruction efficiency estimate, reflecting such accuracy.

To estimate the systematic uncertainty associated with mismodeling these correction factors, one possible approach would involve using control channels sensitive to those auxiliary efficiencies and whose branching ratios are known with high precision. By applying the same selections described in this analysis to these channels, it might be possible to measure the branching fraction in both experimental data and Monte Carlo simulation and use the fractional difference as an estimate of the relevant uncertainty.

- *Systematic uncertainties associated with denominator impurity*: I correct the denominator yield by a factor related to the non-purity of the signal at the denominator. Again, I rely on Monte Carlo simulation to quantify the correction factor, assuming that the estimation of the sample composition at the denominator provided by the simulation is realistic. Incorrect modeling would result in an inaccurate sample com-
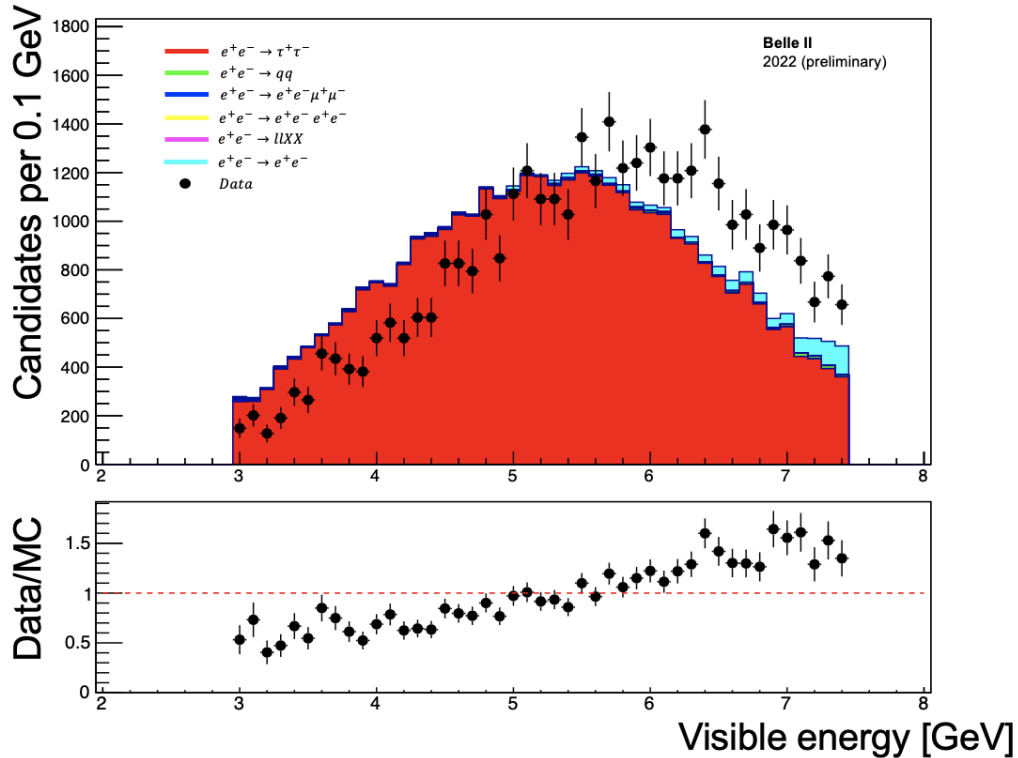
Figure 7.4: (Top panel): data-simulation comparison for the visible energy observable after applying all selections. Data (black points) are normalized to the simulated distribution (colored histogram) whose sample size corresponds to $\int \mathcal{L}\,dt = 7.45$ fb^{-1}. (Bottom panel): data-to-simulation ratio.

position and, consequently, an inaccurate estimate of the correction factor related to denominator non-purity which would bias the results.

Quantifying the systematic uncertainty associated with denominator non-purity is more involved. One possible option would be to rely on the accumulated experience of various Belle II analyses of $\tau^- \to \pi^- \nu_\tau$ that contribute to validate the general accuracy of Belle II simulated $\tau^+\tau^-$ sample composition. Another could be to perform an auxiliary analysis devoted exclusively to the denominator, aimed at quantitatively measuring purity and estimating the associated systematic uncertainty.

- *Systematic uncertainties related to the fit model*: in the numerator I use a fit of the π^0 invariant mass distribution to estimate the yield. As discussed in section 5.10, I choose an empirical fit model to describe the signal and the background. This choice introduces systematic uncertainty since the model generating the data most probably differs from the model I adopted.

  To assess the systematic uncertainty associated with the signal yield estimate at the numerator, I would repeat the fit using a few combinations of equally adequate models for signal and background and use the fractional difference between the yields obtained as uncertainty.

- *Systematic uncertainties related to the branching fractions*: in the final equation 7.1, which defines the π^0 reconstruction efficiency, we use as external inputs the branch-
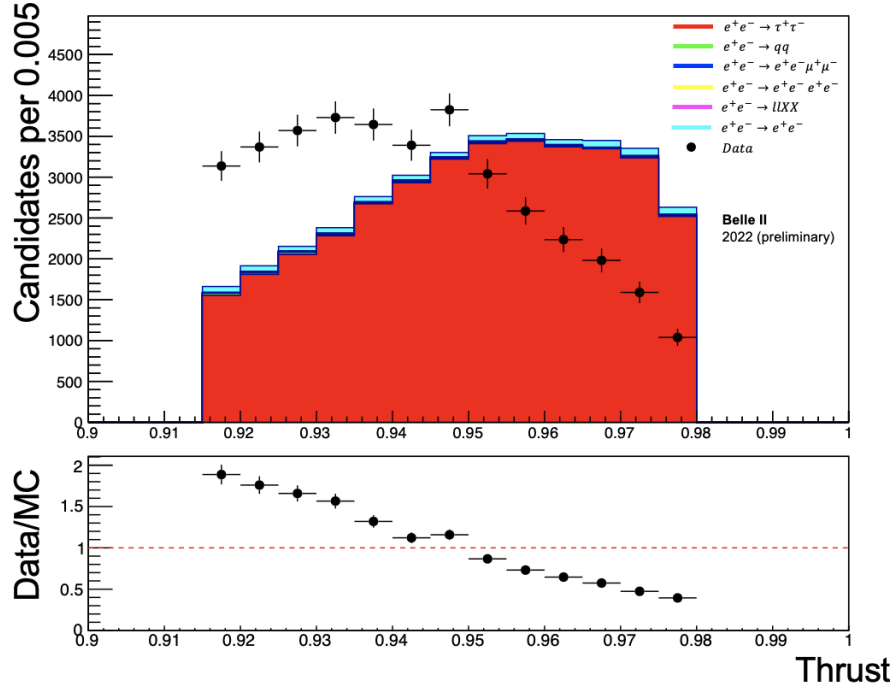
Figure 7.5: (Top panel): data-simulation comparison for the thrust observable after applying all selections. Data (black points) are normalized to the simulated distribution (colored histogram) whose sample size corresponds to $\int \mathcal{L}\,dt = 7.45$ fb^{-1}. (Bottom panel): data-to-simulation ratio.
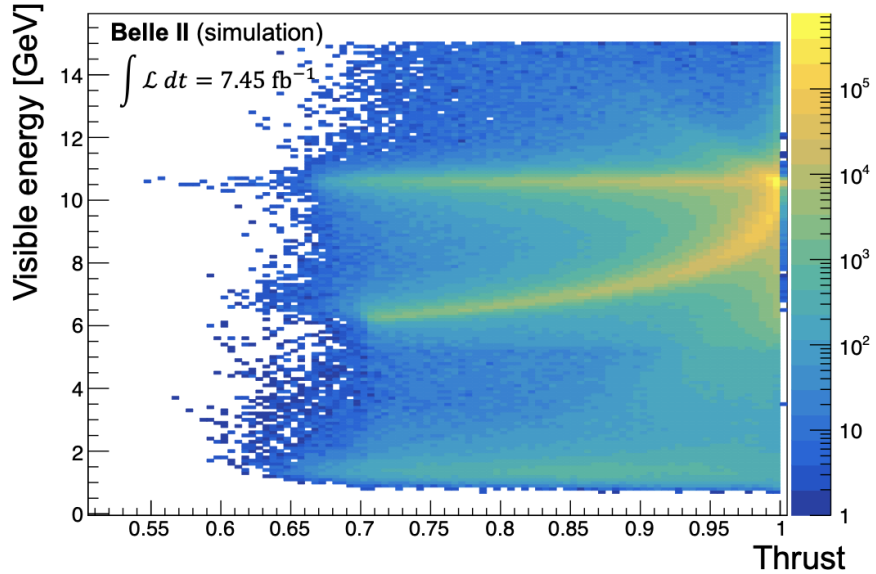
Figure 7.6: Visible energy as a function of thrust for a realistic sample of simulated data after trigger selections. The integrated luminosity corresponds to $\int \mathcal{L}\,dt = 7.45$ fb^{-1}.

ing fractions of the decay channels considered in this analysis, $\mathcal{B}(\tau^- \to \pi^- \pi^0 \nu_\tau)$, $\mathcal{B}(\tau^- \to \pi^- \nu_\tau)$ and $\mathcal{B}(\pi^0 \to \gamma\gamma)$. These are known within their uncertainties [12].
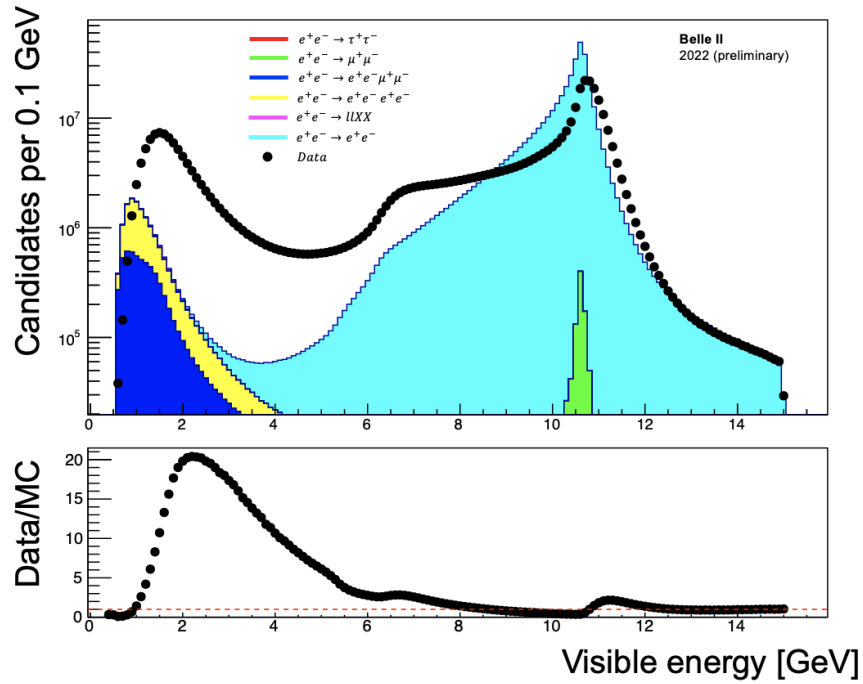
Figure 7.7: (Top panel): data-simulation comparison for the visible energy observable before any selection. Data (black points) are normalized to the simulated distribution (colored histogram) whose sample size corresponds to $\int \mathcal{L}\, dt = 7.45$ fb^{-1}. (Bottom panel): data-to-simulation ratio.

The relevant systematic uncertainties would be obtained by propagating those uncertainties in the final results.

Chapter 8

Summary

This thesis explores the feasibility of a new method for determining the π^0 reconstruction efficiency in Belle II with performances superior to those of existing methods which are limited to 3%-4% by irreducible uncertainties.

Improving the accuracy on the efficiency is important. Many processes sensitive to physics beyond the Standard Model require the measurement of absolute decay rates involving π^0 mesons, in which the π^0 reconstruction efficiency is often the main source of systematic uncertainty, significantly limiting the reach.

The method described in this work determines the π^0 meson reconstruction efficiency in data, relative to simulation, using the rate ratio between $\tau^- \to \pi^- \pi^0 \nu_\tau$ and $\tau^- \to \pi^- \nu_\tau$ decays.

Due to the high accuracy with which these rates are known, the low background, and the wide momentum spectrum covered by π^0, this method could potentially allow for fractional accuracy in the π^0 efficiency of the order of 10^{-2} or lower.

I isolate two mutually disjoint samples, signal enriched via dedicated optimizations, of $\tau^- \to \pi^- \pi^0 \nu_\tau$ and $\tau^- \to \pi^- \nu_\tau$ decays, to extract the yields needed for estimating the π^0 reconstruction efficiency. I start from a simplified scenario based on a sample containing only τ pair events. Then, I generalize the method to a complete simulated sample, demonstrating its validity in realistic conditions. Special care is devoted to identify and determine the necessary corrections to account for the differences between the numerator and denominator. Finally, a qualitative preliminary analysis of the experimental data distributions, compared with realistic simulations reveals unexpected discrepancies. I discuss these discrepancies and possible solutions to work around them.

The results validated against samples of known efficiency demonstrate the conceptual feasibility of the method, illustrate its detailed practical implementation, and confirm its promising potential for application in Belle II data.

Bibliography

[1] S. Weinberg, *A Model of Leptons*, Phys. Rev. Lett. **19** (1967) 1264.

[2] S. L. Glashow, *Partial-Symmetries of Weak Interactions*, Nuclear Physics **22** (1961) 579.

[3] A. Salam, *Weak and Electromagnetic Interactions*, Conf. Proc. C **680519** (1968) 367.

[4] F. Englert and R. Brout, *Broken Symmetry and the Mass of Gauge Vector Mesons*, Phys. Rev. Lett. **13** (1964) 321.

[5] P. W. Higgs, *Broken Symmetries and the Masses of Gauge Bosons*, Phys. Rev. Lett. **13** (1964) 508.

[6] G. Guralnik, C. Hagen, and T. Kibble, *Global Conservation Laws and Massless Particles*, Phys. Rev. Lett. **13** (1964) 585.

[7] To a good approximation, the attractive force between quarks grows linearly with distance. As two quarks are separated, putting energy into the bounded system, it becomes energetically favorable for a new quark–antiquark pair to appear, rather than extending the distance further. As a consequence new bounded states are generated instead of separeted and free quarks.

[8] R. Manfredi, *Measurement of the properties of $B^+ \rightarrow \rho^+ \rho^0$ decays at Belle II. PhD thesis, University of Trieste*, 2022.

[9] G. Lüders, *Proof of the TCP Theorem*, Annals of Physics **2** (1957) 1.

[10] W. Pauli, *Exclusion Principle, Lorentz Group, and Reversal of Space-time and Charge*, Niels Bohr and the Development of Physics (1955) 1.

[11] C. B. Adams *et al.*, *Axion Dark Matter*, 2023. `arXiv:2203.14923 [hep-ex]`.

[12] R. L. Workman and Others, Particle Data Group, *Review of Particle Physics*, PTEP **2022** (2022) 083C01.

[13] M. Gell-Mann and M. Lévy, *The Axial Vector Current in Beta Decay*, Il Nuovo Cimento **16** (1960) 705.

[14] N. Cabibbo, *Unitary Symmetry and Leptonic Decays*, Phys. Rev. Lett. **10** (1963) 531.

[15] S. L. Glashow, J. Iliopoulos, and L. Maiani, *Weak Interactions with Lepton-Hadron Symmetry*, Phys. Rev. D **2** (1970) 1285.

[16] M. Kobayashi and T. Maskawa, *CP-Violation in the Renormalizable Theory of Weak Interaction*, Prog. Theor. Phys. **49** (1973) 652.

[17] A general $N{\times}N$ complex matrix U is defined with $2N^2$ free parameters. The unitary condition $UU^\dagger = \mathbb{1}$ eliminates N^2 degrees of freedom. We can then redefine $(N-1)$ quark fields to absorb $(N-1)^2$ free parameters.
We end up with $2N^2 - N^2 - (2N-1) = (N-1)^2$ free parameters.

[18] L. Wolfenstein, *Parametrization of the Kobayashi-Maskawa Matrix*, Phys. Rev. Lett. **51** (1983) 1945.

[19] C. Jarlskog, *Commutator of the Quark Mass Matrices in the Standard Electroweak Model and a Measure of Maximal CP Violation*, Phys. Rev. Lett. **55** (1985) 1039.

[20] C. Jarlskog, *A Basis Independent Formulation of the Connection Between Quark Mass Matrices, CP Violation and Experiment*, Z. Phys. C **29** (1985) 491.

[21] I. Dunietz, O. W. Greenberg, and D. Wu, *A Priori Definition of Maximal CP Nonconservation*, Phys. Rev. Lett. **55** (1985) 2935.

[22] W. Hulsbergen, *Constraining new physics in meson mixing*, Modern Physics Letters A **28** (2013) no. 27, .

[23] R. Lewis, *On the phenomenological description of CP violation for K-mesons and its consequences*, Phys. Rev. Letters **14** (1965) 749.

[24] Y. Amhis *et al.*, HFLAV, *Averages of b-hadron, c-hadron, and τ-lepton properties as of 2021*, Phys. Rev. D **107** (2023) 052008, `arXiv:2206.07501 [hep-ex]`.

[25] J. Charles *et al.*, CKMfitter Group, *Unitarity Triangle Plot*, Eur. Phys. J. C **41** (2005, updated plots available at `http://ckmfitter.in2p3.fr`) no. 1, .

[26] B. Pal *et al.*, Belle, *Measurement of the branching fraction and time-dependent CP asymmetry for $B^0 \to J/\psi\pi^0$ decays*, Phys. Rev. D **98** (2018) no. 11, 112008, `arXiv:1810.01356 [hep-ex]`.

[27] M. Gronau, *A precise sum rule among four $B \to K\pi$ CP asymmetries*, Physics Letters B **627** (2005) no. 1-4, 82–88.

[28] F. Abudinén *et al.*, Belle II Collaboration, *Measurement of the branching fraction and CP asymmetry of $B^0 \to \pi^0\pi^0$ decays using 198×10^6 $B\overline{B}$ pairs in Belle II data*, Phys. Rev. D **107** (2023) 112009.

[29] Y. Ohnishi *et al.*, *Accelerator Design at SuperKEKB*, Prog. Theo. Exp. Phys. (2013) 03A011.

[30] P. Franchini, *Studio delle prestazioni del nuovo rivelatore di muoni con tecnologia LST nell'esperimeto BaBar*, .

[31] P. Oddone, *Detector Considerations*, in D. H. Stork, proceedings of Workshop on Conceptual Design of a Test Linear Collider: Possibilities for a BB Factory (1987) 423.

[32] S. Eidelman, A. Nefediev, P. Pakhlov, and V. Zhukova, *Superfactory of bottomed hadrons Belle II*, 12, 2020.

[33] P. Raimondi *et al.*, *Beam-Beam Issues for Colliding Schemes with Large Piwinski Angle and Crabbed Waist*, `arXiv:physics/0702033`.

[34] A. Gabrielli, *Caratterizzazione approfondita di sensori al diamante per un aggiornamento del monitor di radiazione di Belle II*, 2020.

[35] D. R. Douglas, J. Kewisch, and R. C. York, *Betatron Function Parameterization of Beam Optics Including Acceleration*, in *Proceedings of the 1988 Linear Accelerator Conference.* (1988).

[36] S. Verdu-Andres, *Luminosity Geometric Reduction Factor from Colliding Bunches with Different Lengths*, BNL Report BNL-114409-2017-IR, (2017).

[37] T. Abe *et al.*, Belle II Collaboration, *Belle II Technical Design Report*, `arXiv:1011.0352`.

[38] I. Adachi, T. Browder, P. Križan, S. Tanaka, Y. Ushiroda, B. I. Collaboration, *et al.*, *Detectors for extreme luminosity: Belle II*, Nuclear Instruments and Methods in Physics Research Section A: Accelerators, Spectrometers, Detectors and Associated Equipment **907** (2018) 46–59.

[39] C. Marinas, DEPFET, *The Belle II Pixel Detector: High precision with Low Material*, Nucl. Instrum. Meth. A **731** (2013) 31.

[40] K. Adamczyk *et al.*, Belle-II Collaboration, *The Belle II Silicon Vertex Detector Assembly and Mechanics*, Nucl. Instrum. Meth. A **845** (2017) 38.

[41] H.-G. Moser, *R and D on Interconnection Technology for Belle II and SLHC*, p. 036. 02, 2011.

[42] Lück *et al.*, *Performance studies of the Belle II Silicon Vertex Detector with data taken at the DESY test beam in April 2016*, p. 057. 03, 2017.

[43] H. Hirano *et al.*, *A High-Resolution Cylindrical Drift Chamber for the KEK B-Factory*, Nucl. Instrum. Meth. A **455** (2000) 294.

[44] V. Bertacchi *et al.*, *Track finding at Belle II*, Computer Physics Communications **259** (2021) 107610.

[45] V. Aulchenko *et al.*, *Electromagnetic calorimeter for Belle II*, J. Phys. Conf. Ser. **587** (2015) no. 1, 012045.

[46] M. Milesi, *Lepton identification in Belle II using observables from the electromagnetic calorimeter and precision trackers*, Talk at CHEP 2019 , `https://indico.cern.ch/event/773049/contributions/3476156/attachments/1932835/3217425/mmilesi_mva_CHEP_07_11_19.pdf`.

[47] S. Raiz, *Measurement of the properties of $B^0 \to \pi^0 \pi^0$ decays at Belle II. PhD thesis, University of Trieste*, 2023.

[48] K. Inami *et al.*, *TOP Counter for Particle Identification at the Belle II Experiment*, Nucl. Instrum. Meth. A **766** (2014) 5.

[49] B. Santoro, *Studio del sistema di monitoring della calibrazione del rivelatore iTOP dell'esperimento Belle II*, 2019.

[50] S. Iwata *et al.*, *Particle Identification Performance of the Prototype Aerogel RICH Counter for the Belle II Experiment*, Prog. Theo. Exp. Phys. **2016** (2016) 033H01.

[51] Santelj *et al.*, *The Aerogel RICH detector of the Belle II experiment*, p. 181. 09, 2020.

[52] A. Abashian *et al.*, Belle II Collaboration, The K_L/μ detector subsystem for the BELLE experiment at the KEK B factory, Nucl. Instrum. Meth. A **449** (2000) 112.

[53] T. Alexopoulos, M. Bachtis, E. Gazis, and G. Tsipolitis, *Implementation of the Legendre Transform for track segment reconstruction in drift tube chambers*, Nucl. Instrum. Meth. A **592** (2008) no. 3, 456.

[54] R. Mankel, *Pattern recognition and event reconstruction in particle physics experiments*, Reports on Progress in Physics **67** (2004) no. 4, 553.

[55] Krohn *et al.*, *Global Decay Chain Vertex Fitting at B-Factories*, 01, 2019.

[56] H. Bethe, *Theory of the Passage of Fast Corpuscular Rays Through Matter*, Annalen Phys. **5** (1930) 325.

[57] F. Bethe, *Stopping power of atoms with several electrons*, Z. Phys. **81** (1933) 363.

[58] M. Starič *et al.*, *Likelihood analysis of patterns in a time-of-propagation (TOP) counter*, Nucl. Instrum. Meth. A **595** (2008) 252.

[59] M. Starič, *Pattern recognition for the time-of-propagation counter*, Nucl. Instrum. Meth. A **639** (2011) 252.

[60] J. Neyman and E. S. Pearson, *IX. On the problem of the most efficient tests of statistical hypotheses*, Phil. Trans. R. Soc. Lond. A. **231** (1933) 289.

[61] S. Brandt, C. Peyrou, R. Sosnowski, and A. Wroblewski, *The Principal Axis of Jets. An Attempt to Analyze High-Energy Collisions as Two-Body Processes*, Phys. Lett. **12** (1964) 57.

[62] T. Sjöstrand, S. Mrenna, and P. Skands, *PYTHIA 6.4 Physics and Manual*, Journal of High Energy Physics **2006** (2006) no. 05, 026.

[63] M. Chrzaszcz, T. Przedzinski, Z. Was, and J. Zaremba, *TAUOLA of τ lepton decays—framework for hadronic currents, matrix elements and anomalous decays*, Computer Physics Communications **232** (2018) 220.

[64] P. Golonka and Z. Was, *PHOTOS Monte Carlo: a Precision Tool for QED Corrections in Z and W Decays*, Eur. Phys. J. C **45** (2006) no. 1, 97.

[65] S. Agostinelli *et al.*, GEANT4, *GEANT4 – a Simulation Toolkit*, Nucl. Instrum. Meth. A **506** (2003) 250.

[66] B. Ward, S. Jadach, and Z. Was, *Precision Calculation for $e^+e^- \to 2f$: the KK MC Project*, Nuclear Physics B - Proceedings Supplements **116** (2003) 73.

[67] J. E. Gaiser *et al.*, *Charmonium spectroscopy from inclusive ψ' and J/ψ radiative decays*, Phys. Rev. D **34** (Aug, 1986) 711–721.
https://link.aps.org/doi/10.1103/PhysRevD.34.711.

[68] W. Verkerke and D. Kirkby, *The RooFit toolkit for data modeling*, 2003.
arXiv:physics/0306116 [physics.data-an],
https://arxiv.org/abs/physics/0306116.

[69] I. Adachi *et al.*, Belle II Collaboration, *Measurement of branching fractions and
direct CP asymmetries for $B \to K\pi$ and $B \to \pi\pi$ decays at Belle II*, Phys. Rev. D
109 (2024) 012001.